Hadron properties in QCD with two dynamical quark flavors

Dissertation
zur Erlangung des akademischen Grades
Doktor der Naturwissenschaften (Dr. rer. nat.)

Angefertigt am Institut für Physik
der Karl-Franzens-Universität Graz

Eingereicht von
Markus Limmer

Betreut von
Prof. Dr. Christian B. Lang

April 2011

Präambel

Ich bestätige, dass es sich bei der hier vorgelegten Dissertation um eine Originalarbeit handelt, die von mir selbständig angefertigt und abgefasst wurde.

. . . . . .

(Markus Limmer)

Summary

Here, I present the essential results of my doctoral thesis, which was done in the field of lattice QCD. This work can be seen as one of the cornerstones of a long-ranging project, started already at the beginning of the year 2000. Since then, several groups, associated in the Bern-Graz-Regensburg (BGR) collaboration, continuously worked on that project.

In this report I will discuss results on various sectors of lattice QCD. Seven sets of gauge field configurations with a lattice size of $16^3 \times 32$ and a spatial extent of about 2.2 fm have been created; the pion masses are ranging from 602 MeV down to 257 MeV. The configurations include two mass degenerate dynamical light quarks; the Lüscher-Weisz gauge action and the Chirally Improved Dirac operator have been used. In each set 200 or 300 uncorrelated configurations are available for analyses.

The results are located in three different fields. An analysis of low energy parameters was done, to be more precise, the axial Ward-identity mass and (the pion and kaon) decay constants have been investigated. The experimentally accessible value for the ratio of these decay constants is in reasonable agreement with the value obtained here. The second area of research concerns the angular momentum decomposition of the vector meson ρ. In our approach it could be shown that the first excited state of the ρ meson is not a pure S wave state, which is contrary to the quark model. The main focus of this work was based on hadron spectroscopy. This task was done using the variational method. A broad spectrum of baryons and mesons could be covered here. Also hadrons including strange quarks have been analyzed, however, the strange quark being a partially quenched strange quark. Generally speaking, the studied hadron channels compare favorably to the experimental values.

Finally, I want to mention all publication directly related to this doctoral thesis:

1. **"The chiral and angular momentum content of the ρ-mesons in lattice QCD"**
   L. Y. Glozman, C. B. Lang and M. Limmer
   PoS **LATTICE2010** 149 (2010), [arXiv:1010.5660]

2. **"Some results on excited hadrons in 2-flavor QCD"**
   G. P. Engel, C. B. Lang, M. Limmer, D. Mohler and A. Schäfer
   PoS **LATTICE2010** 103 (2010), [arXiv:1010.2366]

3. **"Effective chiral restoration in the ρ'-meson in lattice QCD"**
   L. Y. Glozman, C. B. Lang and M. Limmer
   Phys. Rev. D **82** 097501 (2010), [arXiv:1007.1346]

4. **"Meson and baryon spectrum for QCD with two light dynamical quarks"**
   G. P. Engel, C. B. Lang, M. Limmer, D. Mohler and A. Schäfer
   Phys. Rev. D **82** 034505 (2010), [arXiv:1005.1748]

5. **"Lattice study of light scalar tetra-quarks with I=0,2,1/2,3/2: are σ and κ tetra-quarks?"**
   S. Prelovsek, T. Draper, C. B. Lang, M. Limmer, K. F. Liu, N. Mathur and D. Mohler
   Phys. Rev. D **82** 094507 (2010), [arXiv:1005.0948]

6. **"Searching for tetra-quarks on the lattice"**
   S. Prelovsek, T. Draper, C. B. Lang, M. Limmer, K. F. Liu, N. Mathur and D. Mohler
   arXiv:1002.0193, to appear in proceedings of Lepton-Photon 2009, Hamburg

7. **"Baryon axial charges from Chirally Improved fermions – first results"**
   G. Engel, C. Gattringer, L. Y. Glozman, C. B. Lang, M. Limmer, D. Mohler and A. Schäfer
   PoS **LAT2009** 135 (2009), [arXiv:0910.4190]

8. **"Excited hadrons in $n_f = 2$ QCD"**
   G. Engel, C. Gattringer, C. B. Lang, M. Limmer, D. Mohler and A. Schäfer
   PoS **LAT2009** 088 (2009), [arXiv:0910.2802]

9. **"Spectroscopy of light tetra-quark states"**
   S. Prelovsek, C. B. Lang, M. Limmer, D. Mohler, T. Draper, K. F. Liu and N. Mathur
   PoS **LAT2009** 103 (2009), [arXiv:0910.2749]

10. **"The chiral and angular momentum content of the ρ-meson"**
    L. Y. Glozman, C. B. Lang and M. Limmer
    Few Body Syst. **47** 91 (2010), [arXiv:0909.2939]

11. **"Angular momentum content of the ρ-meson in lattice QCD"**
    L. Y. Glozman, C. B. Lang and M. Limmer
    Phys. Rev. Lett. **103** 121601 (2009), [arXiv:0905.0811]

12. **"Comparison of filtering methods in SU(3) lattice gauge theory"**
    F. Bruckmann, F. Gruber, C. B. Lang, M. Limmer, T. Maurer, A. Schäfer and S. Solbrig
    PoS **CONFINEMENT8** 045 (2008), [arXiv:0901.2286]

13. **"Hadron Spectroscopy with Dynamical Chirally Improved Fermions"**
    C. Gattringer, C. Hagen, C. B. Lang, M. Limmer, D. Mohler and A. Schäfer
    Phys. Rev. D **79** 054501 (2009), [arXiv:0812.1681]

14. **"Spectroscopy with dynamical Chirally Improved quarks"**
    C. Gattringer, C. B. Lang, M. Limmer, T. Maurer, D. Mohler and A. Schäfer
    PoS **LATTICE2008** 093 (2008), [arXiv:0809.4514]

15. **"Heavy-light hadrons and their excitations"**
    T. Burch, C. Hagen, C. B. Lang, M. Limmer and A. Schäfer
    PoS **LATTICE2008**, 110 (2008), [arXiv:0809.3923]

16. **"Excitations of single-beauty hadrons"**
    T. Burch, C. Hagen, C. B. Lang, M. Limmer and A. Schäfer
    Phys. Rev. D **79** 014504 (2009), [arXiv:0809.1103]

17. **"Dynamical Chirally Improved Quarks: First Results for Hadron Masses"**
    R. Frigori, C. Gattringer, C. B. Lang, M. Limmer, T. Maurer, D. Mohler and A. Schäfer
    PoS **LAT2007** 114 (2007), [arXiv:0709.4582]

18. **"B meson excitations with chirally improved light quarks"**
    T. Burch, D. Chakrabarti, C. Hagen, T. Maurer, A. Schäfer, C. B. Lang and M. Limmer
    PoS **LAT2007** 091 (2007), [arXiv:0709.3708]

Contents

Chapter 1

Introduction

As a part of the standard model, the theory of strong interactions, i.e., the theory of particles carrying color charge, is described by Quantum Chromodynamics (QCD). The basic components of QCD are quarks and gluons, which mediate the underlying force. This force acts on two different scales. On one hand the strong force is responsible for building protons or neutrons out of quarks, and on the other hand it binds protons and neutrons into atomic nuclei. In general, quarks can form mesons (built from a quark and an antiquark) or baryons (built from three quarks), both being color neutral objects. The only well-established, non-perturbative theoretical approach to that field is given by lattice QCD. Within this method, QCD is formulated on a discrete (Euclidean) space-time lattice. Thus, lattice QCD is mathematically well-defined, since the discreteness introduces a momentum cut off, which regularizes the theory. We are therefore able to simulate QCD numerically using (super)computers and obtain observables by application of methods from statistical mechanics.

Already nowadays the ground state mass spectrum of hadrons obtained from lattice QCD impressively agrees with experimental results – a good verification for lattice QCD! However, a large number of excitations are established in experiments, thus a theoretical understanding of these excitations is worthwhile. Also other particle properties, which cannot be accessed with perturbative methods, like low energy parameters, are well-known from experiments. A deeper theoretical insight into these fields can help to increase our knowledge drastically. Hence, the purpose of this doctoral thesis is to study hadronic properties with this non-perturbative *ab initio* approach.

The first formulation of lattice QCD, brought up by K. G. Wilson in 1974 [1], faces two severe problem: it produces 15 additional (unphysical) fermions (called doublers) and it does not respect chiral symmetry. However, Wilson could solve the doubling problem, but the correct implementation of chiral symmetry was a long standing problem. In 1981 it was partly solved by a no-go theorem by Nielson and Ninomyia [2, 3, 4]. They showed that it is not possible to have a theory which is simultaneously local, chirally symmetric and free of doublers. Thus, a lattice version of chiral symmetry was proposed (Ginsparg-Wilson equation), which recovers the

continuum formulation in the right way. But only over two decades after Wilson's formulation H. Neuberger 1997 was able to find a formulation [5] which fulfills all requirements.

In our approach we use the so-called Chirally Improved Dirac operator (D_{CI}) to describe the fermions. It is a compromise, concerning computational resources and the quality of results, between the Wilson action and Neuberger's Overlap operator. The D_{CI} only approximately fulfills the Ginsparg-Wilson equation, but one reasonably can simulate small pion masses on rather coarse lattices. Since quenched simulations using this type of Dirac operator have produced promising results, a project to use the D_{CI} in a dynamical lattice QCD simulation has started already in 2003. The first task was setting up the code, which was done by former members of our group. First results on smaller lattices have been published in [6, 7, 8]. In this doctoral thesis we extend the working basis, i.e., more run sequences on bigger lattices are analyzed in various aspects. The main results of these tasks are presented here.

This thesis can be divided into two parts, the first one is containing all theoretical ideas needed. It starts with Chap. 2, where we give a short introduction into the field of lattice QCD. We present the continuum formulation of QCD and explain the quantization process afterward. Wilson's first formulation and, after a digression concerning chiral symmetry, also actions with better chirality are discussed. This chapter is closed with the issue of setting the scale of a simulation.

All topics related to the production of gauge fields can be found in Chap. 3. The gauge and fermion action we use are discussed, details about the Hybrid Monte Carlo algorithm and the attempts to speed up the code are presented. Furthermore we give details on autocorrelation and various parameters of our simulation.

Chap. 4 contains the preparatory concepts for hadron spectroscopy. We outline several spectroscopy techniques, especially the variational method, and explain the concepts of quark field and link smearing. The idea of a mass independent scheme for the lattice spacing is discussed and finally properties of scattering states are presented.

The second part of the thesis deals with the obtained results. In Chaps. 5 and 6 all analyzed baryon and meson channels, including also hadrons with strange quarks, are discussed. Low energy parameters, like the AWI mass of decay constants, can be found in Chap. 7. In Chap. 8 we analyze the partial wave content of the vector meson, using the techniques discussed before. Finally, we summarize all results and give a short outlook in Chap. 9.

Chapter 2

Quantum Chromodynamics on a lattice

2.1 Quantum Chromodynamics in the continuum

The continuum formulation of the Quantum Chromodynamics (QCD) action in 4-dimensional Euclidean space-time is given by

$$S_{\mathrm{QCD}}[\psi,\overline{\psi},A] = S_{\mathrm{F}}[\psi,\overline{\psi},A] + S_{\mathrm{G}}[A] \ , \tag{2.1}$$

$$S_{\mathrm{F}}[\psi,\overline{\psi},A] = \sum_{f=1}^{N_f} \int d^4x \ \overline{\psi}^{(f)}(x) \left[\gamma_\mu D_\mu + m^{(f)}\right] \psi^{(f)}(x) \ , \tag{2.2}$$

$$S_{\mathrm{G}}[A] = \frac{1}{2g^2} \mathrm{Tr}\left[F_{\mu\nu}\, F_{\mu\nu}\right] \ . \tag{2.3}$$

Here, S_{F} and S_{G} represent the fermionic and the gauge part, respectively. $\psi, \overline{\psi}$ are Dirac spinors representing the quark fields and they are carrying a space-time index x, a Dirac index $\alpha = 1, \ldots, 4$, a color index $c = 1, 2, 3$ and a flavor index $f = 1, \ldots, N_f$. Gluons enter via the gauge field $A \in \mathrm{su}(3)$, which has space-time, Lorentz (μ) and color indices, but no flavor content. Wherever we will not cause confusion, we will omit these indices and use matrix/vector notation. D_μ is called a covariant derivative and is given by

$$D_\mu = \partial_\mu + igA_\mu \ , \tag{2.4}$$

with the coupling constant g. The mass matrix containing the different flavors is represented by $m^{(f)} = \mathrm{diag}(m_1, m_2, \ldots, m_{N_f})$.

The field-strength tensor $F_{\mu\nu}$, which appears in S_{G}, plays a special role. Since

$$F_{\mu\nu} = \partial_\mu A_\nu - \partial_\nu A_\mu + i\left[A_\mu, A_\nu\right] \ , \tag{2.5}$$

and the A_μ are non-abelian fields, Eq. (2.3) leads to cubic and even quartic terms in the gauge fields. These so-called self interactions give rise to the most eminent feature of QCD, namely color confinement.

Flavor	Mass [MeV]
up (u)	$1.5 - 3.3$
down (d)	$3.5 - 6.0$
strange (s)	$70 - 130$

Flavor	Mass [GeV]
charm (c)	$1.16 - 1.34$
bottom (b)	$4.13 - 4.37$
top (t)	$169.0 - 173.6$

Table 2.1: *The six quark flavors appearing in nature and their masses in the $\overline{MS}$ scheme [9]. On the l.h.s. the three flavors of the light sector can be found (in units of MeV), the heavy quark flavors are on the r.h.s. (in units of 10^3 MeV!).*

Let us quickly discuss the flavor index f again. In principle, QCD would work with any number of flavors. But in Nature there are only six quark flavors; they can be split into two groups, the light and the heavy sector (see Tab. 2.1). Especially in lattice QCD one is restricted to less than six dynamical flavors and often 0, 2 or $2 + 1$ flavors are used in the calculations.

2.2 Quantization with the Path Integral

Up to now, we have considered the continuum formulation of the theory. To be able to quantize it, we use the Path Integral formulation, which goes back to Feynman [10].

The generating functional, or in other words the partition function, for QCD is given by

$$Z = \int \mathcal{D}[\psi, \overline{\psi}]\, \mathcal{D}[A]\, e^{-S_{\mathrm{QCD}}[\psi, \overline{\psi}, A]} \ . \tag{2.6}$$

The integration has to be done for all possible field configurations of $\psi, \overline{\psi}$ and A. Since we are using a Euclidean instead of a Minkowski metric, no imaginary unit in front of the action is present.

The expectation value of some function F in the Path Integral formulation is

$$\langle F \rangle = \frac{1}{Z} \int \mathcal{D}[\psi, \overline{\psi}]\, \mathcal{D}[A]\, F[\psi, \overline{\psi}, A]\, e^{-S_{\mathrm{QCD}}[\psi, \overline{\psi}, A]} \ . \tag{2.7}$$

The main object, we will be interested in later on, are correlation functions of two operators. These correlators are defined as

$$\langle O_2(t) O_1(0) \rangle = \frac{1}{Z} \int \mathcal{D}[\psi, \overline{\psi}]\, \mathcal{D}[U]\, O_2[\psi, \overline{\psi}, U]\, O_1[\psi, \overline{\psi}, U]\, e^{-S_{\mathrm{QCD}}[\psi, \overline{\psi}, U]} \ . \tag{2.8}$$

Here, $\mathcal{D}[U]$ is called a Haar measure. Eq. 2.8 is nothing but an expectation value of two operators at a time distance t in Hilbert space. The fields U will be introduced and discussed later.

With this tool at hand we will now be able to regularize QCD by using a finite space-time grid, namely the lattice, which we call Λ. To evaluate the extremely high-dimensional integrals from Eq. (2.7) we will use a Markov chain Monte-Carlo simulation.

2.3 The first formulation by Wilson

Now we are able to write down a first formulation for QCD on a lattice. However, a small piece of preparatory work is still needed.

2.3.1 Introduction of gauge fields

In 1974 K. G. Wilson was the first one who formulated QCD on the lattice [1]. With that formulation he wanted to respect two important principles: the first one is the gauge invariance of the theory and the second one is that the naive continuum limit, i.e., the limit $a \to 0$, should turn into the continuum formulation of the theory.

If one now does a "straight forward" discretization of Eqs. (2.2) and (2.3), terms will arise, which couple fermion fields at adjacent lattice sites, e.g., $\overline{\psi}(n)\psi(n+\hat{\mu})$, where $n+\hat{\mu}$ is the neighbor site of n in the positive μ-direction. Such terms are not gauge invariant. To resolve that problem we need to introduce link variables $U_\mu(n)$ which connect the two lattice sites n and $n+\hat{\mu}$. Due to their properties under a local gauge transformation they ensure the gauge invariance of Wilson's theory. The link variable $U_\mu(n)$ has an orientation μ and points from the site n to $n+\hat{\mu}$. These link variables should play the role of gauge transporters, known from the continuum theory. To do so, we define

$$U_\mu(n) = \exp\left(iaA_\mu(n)\right) \in \mathrm{SU}(3) \ . \tag{2.9}$$

Performing the continuum limit, it is easy to see that the link variables approximate the gauge transporter up to order $\mathcal{O}(a)$ [11].

2.3.2 The Wilson gauge action

Since we have introduced the gauge links as the fundamental quantities on the lattice, we now can construct gauge invariant objects. A prominent example of such a gauge invariant object is the trace over a closed loop of link variables. Using these objects, we can write the Wilson gauge action in the following way,

$$S_\mathrm{G}[U] = \frac{2}{g^2} \sum_n \sum_{\mu<\nu} \mathrm{Re\ tr}[1 - U_{\mu\nu}(n)] \ . \tag{2.10}$$

In this equation we used the smallest possible closed loop, the plaquette $U_{\mu\nu}$. It is a product of four link variables,

$$U_{\mu\nu}(n) = U_\mu(n)\, U_\nu(n+\hat{\mu})\, U_{-\mu}(n+\hat{\mu}+\hat{\nu})\, U_{-\nu}(n+\hat{\nu}) \ , \tag{2.11}$$

where we used the definition $U_{-\mu}(n) = U_\mu^\dagger(n-\hat{\mu})$ for $U \in \mathrm{SU}(3)$. Mostly the inverse gauge coupling β is used instead of g, it is defined as

$$\beta = \frac{6}{g^2} \ . \tag{2.12}$$

This formulation is often called naive, since it is an easy and straightforward discretization.

2.3.3 The doubling problem

If one "takes the easy way out", a naive discretization is done for the action. To be more precise, the derivative from Eq. (2.2) is simply replaced by a symmetric difference, and one ends up with [1]

$$S_\mathrm{F}[\psi,\overline{\psi},U] = a^4 \sum_n \overline{\psi}(n)\Big[\sum_{\mu=1}^{4}\gamma_\mu \frac{U_\mu(n)\psi(n+\hat{\mu}) - U_{-\mu}(n)\psi(n-\hat{\mu})}{2a} + m\psi(n)\Big] \ . \tag{2.13}$$

Let us now have a closer look at that object. Considering the case of just one massless quark-flavor for a free theory, i.e., all $U_\mu(n) = 1$, we can derive an analytic expression for the Dirac matrix and its inverse, the quark propagator. The propagator in momentum space is given by

$$\tilde{D}(p) = \frac{-ia^{-1}\sum_\mu \gamma_\mu \sin(p_\mu a)}{a^{-2}\sum_\mu \sin^2(p_\mu a)} \ . \tag{2.14}$$

As in the continuum, this propagator should have a pole at $\boldsymbol{p}_0 = (0,0,0,0)$, which describes the single fermion considered. However, a different situation is encountered here. Eq. (2.14) has additional poles in the Brillouin zone $-\pi/a < p_\mu \leqslant \pi/a$ at

$$\boldsymbol{p}_1 = \left(\frac{\pi}{a},0,0,0\right),\ \boldsymbol{p}_2 = \left(0,\frac{\pi}{a},0,0\right),\ \ldots,\ \boldsymbol{p}_{15} = \left(\frac{\pi}{a},\frac{\pi}{a},\frac{\pi}{a},\frac{\pi}{a}\right) \ . \tag{2.15}$$

These 15 unphysical poles $\boldsymbol{p}_1,\ldots,\boldsymbol{p}_{15}$ are called doublers.

This problem was solved by Wilson by introducing the so-called Wilson term. This term is simply added to the Dirac operator. In momentum space the Wilson term is

$$\frac{1}{a}\sum_{\mu=1}^{4}[1-\cos(p_\mu a)] \ . \tag{2.16}$$

This expression fulfills all conditions that we want. For components with $p_\mu = 0$ it vanishes, for components with $p_\mu = \pi/a$ it contributes a term $2/a$. This term can be understood as an extra mass term, which diverges in the limit $a \to 0$. Thus, the doublers decouple from the theory.

To summarize the equations above, we write down the full Wilson Dirac operator in position space,

$$D_{\mathrm{W}}(n,m) = \left(m + \frac{4}{a}\right)\delta_{n,m} - \frac{1}{2a}\sum_{\mu=\pm1}^{\pm4}(1-\gamma_\mu)U_\mu(n)\delta_{n+\hat{\mu},m}\ . \tag{2.17}$$

Here, we dropped all color, Dirac and flavor indices and only show the space-time indices n and m. We also defined $\gamma_{-\mu} = -\gamma_\mu$ for all μ. Finally, we want to stress one important property of the Wilson Dirac operator. The first term in Eq. (2.17), which consists of the quark mass and one part of the Wilson term, explicitly breaks chiral symmetry (for a definition see Sec. 2.4), even for $m = 0$. And exactly this is the most disadvantageous feature of the operator D_{W}. How to overcome that problem is explained in more detail in the next section.

2.4 Chiral symmetry on the lattice

Since chiral symmetry and its breaking has enormous consequences for QCD (such as very small pion masses or the absence of a mass degeneracy for parity partners of baryons), a sound definition of QCD on the lattice should take care of this aspect.

The defining equation for a chirally symmetric Dirac operator in the continuum reads

$$D\,\gamma_5 + \gamma_5\,D = 0\ . \tag{2.18}$$

The Wilson Dirac operator proposed in Eq. (2.17) violates this equation due to the extra Wilson term, which was needed to remove the doublers from the theory. Thus, one wants to find a lattice Dirac operator which is free of doublers and also respects chiral symmetry. However, this cannot be simply solved by adding a term other than the Wilson term. A fundamental theorem by Nielson and Ninomyia [2, 4, 3] points out that a Dirac operator D, which is free of doublers, cannot simultaneously fulfill the following conditions:

1. D is local,

2. D is translational invariant,

3. D is chirally symmetric (i.e., in the sense of (2.18)),

4. $\tilde{D}(p) = ia\gamma_\mu p_\mu + \mathcal{O}(a^2 p_\mu^2)$, where $\tilde{D}(p)$ is the Fourier transform of D.

A solution to that problem was suggested by Ginsparg and Wilson [12]. They "weakened" the expression from (2.18) by simply replacing the right-hand side and presented the famous "Ginsparg-Wilson" equation,

$$D\,\gamma_5 + \gamma_5\,D = a\,D\,\gamma_5\,D\ . \tag{2.19}$$

The right-hand side vanishes for $a \to 0$ and thus the continuum version of chiral symmetry is recovered. Using this equation we are now able to implement chiral symmetry on the lattice [13].

2.5 Fermions with better chirality

In the last section we have shown that using Eq. (2.19) enables us to realize Dirac operators, which show better chiral properties than the Wilson Dirac operator. These Dirac operators can be divided into two classes, one of them fulfilling Eq. (2.19) only approximately and the other class, which fulfills Eq. (2.19) exactly. We now discuss some examples of each class.

2.5.1 The fixed-point operator

A Dirac operator, which fulfills Eq. (2.19) only approximately, is the fixed-point operator [14]. This operator uses an ansatz which is inspired from renormalization-group techniques. The simulation should be carried out very close to the renormalized trajectory, from which one expects a good scaling behavior. It can be shown [15], that the fixed-point Dirac operator satisfies the Ginsparg-Wilson equation. This construction can be used to fix the free parameters of a general Dirac operator, and of course there are infinitely many of these terms. However, for practical reasons one has to truncate to some finite number of terms and thus the fixed-point fermions fulfill Eq. (2.19) only approximately.

2.5.2 The Chirally Improved operator

Another candidate of this class of Dirac operators is the Chirally Improved (CI) Dirac operator [16, 17]. To obtain this kind of Dirac operator one uses the most general ansatz for D and plugs it into Eq. (2.19). Then the resulting set of coupled algebraic equations can be solved numerically. Since also here one has to truncate the number of present terms, the CI operator is only an approximate solution of the Ginsparg-Wilson equation. This type of operator is discussed in more detail in Sec. 3.2, since for our simulation we only use this Dirac operator.

2.5.3 Domain-wall fermions

A concept, which is related to Overlap fermions (discussed below), are the so-called domain-wall fermions [18]. In this approach one extends the Wilson fermions into an auxiliary fifth dimension. In the limit on an infinite length for this additional dimension, the Overlap operator is approached. As usual, the extend of this dimension has to be chosen finite.

2.5.4 The Overlap operator

The Overlap operator [5, 19] fulfills the Ginsparg-Wilson equation (2.19) exactly. For massless fermions it reads

$$D_{\mathrm{O}} = 1 + \gamma_5 \,\mathrm{sign}[\gamma_5 K] \;, \tag{2.20}$$

where K is some kernel Dirac operator, free from doublers. The massive version of the Overlap operator is given by

$$D_{\mathrm{O}}(m) = 1 + m + (1-m)\,\gamma_5 \,\mathrm{sign}[\gamma_5 K] \;, \quad m \in [0,1] \;. \tag{2.21}$$

In most simulations the Wilson Dirac operator from Eq. (2.17) is used as the kernel operator.

Although simulations using Overlap fermions are worthwhile, and some groups are already running such simulations (see, e.g., [20, 21, 22, 23, 24, 25, 26, 27, 28, 29, 30, 31]), the numerical costs are tremendous due to the necessary evaluation of the matrix sign function in Eq. (2.20). Actually this function is well defined via the spectral theorem,

$$\mathrm{sign}[K] = \mathrm{sign}\Big[\sum_k \lambda_k \,|k\rangle\langle k|\Big] = \sum_k \mathrm{sign}[\lambda_k]\,|k\rangle\langle k| \;. \tag{2.22}$$

For the typical sizes of the Dirac matrix used in lattice simulations a complete diagonalization is numerically unaffordable, and thus not done. The alternative, applied in most cases, is to utilize the relation

$$\mathrm{sign}[K] = \frac{K}{|K|} = \frac{K}{\sqrt{K^2}} \;. \tag{2.23}$$

The term $1/\sqrt{K^2}$ is then approximated by either a polynomial in K^2 or by a ratio of polynomials. In such a calculation the convergence depends crucially on the eigenvalues of the kernel K. Thus, one may improve the convergence – and simultaneously the computational costs – by choosing another kernel matrix.

2.6 Determination of the scale

As in every lattice simulation, the output of the calculations are only dimensionless numbers. To relate these numbers to physical quantities, like, e.g., masses, one has to extract the value of the lattice constant a to be able to extract, for example, the mass m from the outcoming result am.

To set this scale, several methods exist, however, we only discuss the strategy we follow for our simulation. For other methods see, e.g., [32, 33, 34, 35, 36, 37].

For the determination of the lattice spacing we use the Sommer parameter [38], determined by the lattice potential, which is derived from Wilson loops $W(r,t)$. For improving the signal, the gauge configurations are smeared with hypercubic blocking [39] with the parameters $a_1 = 0.75$, $a_2 = 0.6$ and $a_3 = 0.3$ (see Sec. 4.5).

We extract the static quark potential $V(r)$ from linear fits to $\ln W(r,t)$. The form of the potential $V(r)$ is given by

$$V(r) = A + \frac{B}{r} + \sigma\, r + C\, \Delta V(r) \;, \tag{2.24}$$

$$\Delta V(r) = \left[\frac{1}{\boldsymbol{r}}\right] - \frac{1}{r} \;. \tag{2.25}$$

A discussion of the perturbative lattice Coulomb potential $[1/\boldsymbol{r}]$ and further details can be found in [40] and references therein.

From the resulting potential and the condition

$$r^2\, \frac{dV(r)}{dr}\bigg|_{r=r_0} = 1.65 \;, \tag{2.26}$$

we obtain the Sommer parameter in lattice units as

$$r_0 = \sqrt{\frac{1.65 + B}{\sigma}} = \frac{r_{0,\mathrm{exp}}}{a} \;. \tag{2.27}$$

The lattice spacing is then given by $a = r_{0,\mathrm{exp}}/r_0$. In our simulation we use the value $r_{0,\mathrm{exp}} = 0.48$ fm. However, this value is not determined precisely from experiment, and the values that are used in the literature vary approximately from $\approx 0.45 \ldots 0.50$ fm. The reason for using $r_{0,\mathrm{exp}} = 0.48$ fm is only based on intuitive arguments.

Thus, one always should keep in mind that, depending on the method and the value used, a possible systematic error from determining the lattice spacing can even exceed the statistical error, coming from the limited number of configurations, of final results. The numbers we obtain on our sets of gauge configurations can be found in Tab. 3.1 in Sec. 3.5.

The Sommer scale was originally comprehended as a purely bosonic observable and thought to be independent of any sea quarks. However, any lattice QCD calculation including dynamical quarks has shown that the ratio r_0/a does depend on the quark mass am_q, which is determined by the bare mass parameters $m^{(f)}$. A strategy to avoid that is presented later in Sec. 4.6, since some preparatory work is still to be done.

Chapter 3

Generating the gauge field configurations

3.1 Lüscher-Weisz gauge action

We now want to briefly discuss an alternative formulation of the gauge action, namely the Lüscher-Weisz gauge action [41]. We use this formulation throughout, because it was shown in [17], that the gauge configurations produced with this kind of action are much smoother compared to the Wilson gauge action.

The simplest gauge action one can consider is the Wilson gauge action, given in Eq. (2.10), which only includes the plaquette of gauge links. A Taylor expansion (i.e., the naive continuum limit $a \to 0$) of this kind of action gives $F_{\mu\nu}F_{\mu\nu}$ in leading order, and the corrections are of the order of $\mathcal{O}(a^2)$. To reduce these corrections, one has to include loops longer than the plaquette. If two types of loops of length 6 are included, one ends up with the Lüscher-Weisz gauge action [41], which is given by

$$S_{\mathrm{LW}} = \frac{\beta_1}{3}\sum_{\mathrm{pl}} \mathrm{Re}\,\mathrm{tr}[1 - U_{\mathrm{pl}}] + \frac{\beta_2}{3}\sum_{\mathrm{re}} \mathrm{Re}\,\mathrm{tr}[1 - U_{\mathrm{re}}] + \frac{\beta_3}{3}\sum_{\mathrm{tb}} \mathrm{Re}\,\mathrm{tr}[1 - U_{\mathrm{tb}}] \ , \quad (3.1)$$

where the sums run over all plaquettes (pl), rectangulars (re) and paths along the edges of a 3-cube, called twisted bent (tb) (see also Fig. 3.1). In this equation β_1 is the independent gauge coupling, β_2, β_3 are determined from tadpole-improved perturbation theory [42]. One additional parameter is needed to calculate these two couplings, the assumed plaquette u_0,

$$u_0 = \left(\frac{1}{3}\mathrm{Re}\,\mathrm{tr}\langle U_{\mathrm{pl}}\rangle\right)^{1/4} \ . \quad (3.2)$$

With

$$\alpha = -\frac{\log u_0^4}{3.06839} \quad (3.3)$$

we get for β_2, β_3 the following expressions,

$$\beta_2 = \frac{\beta_1}{u_0^2}\,\frac{1 + 0.4805\alpha}{20} \ , \quad \beta_3 = \frac{\beta_1}{u_0^2}\,0.03325\alpha \ . \quad (3.4)$$

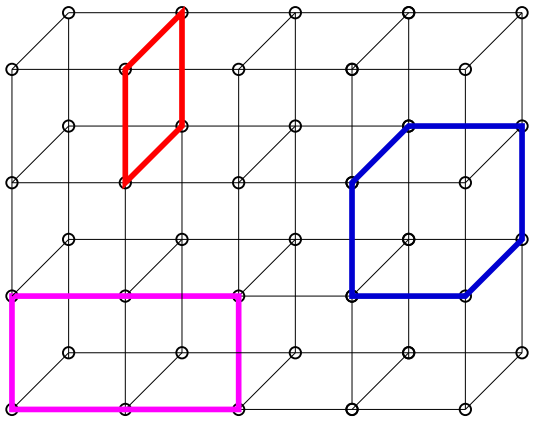

Figure 3.1: *The three loops of gauge links included in the Lüscher-Weisz gauge action. Red: plaquette; magenta: rectangular; blue: twisted bent.*

Finally we want to stress one point about the assumed plaquette. In lattice simulations the value for u_0 should agree with the thermalized plaquette value. Thus, one normally has to calculate u_0 self-consistently by adapting it from time to time to the actual value and then thermalize again. In our simulations, however, we fixed the value permanently to its initial value, since we want to use the same gauge action for all sets of gauge configurations to ensure a better comparability between the sets.

3.2 The Chirally Improved Dirac operator

As already stated in Sec. 2.5, we use the CI Dirac operator [16, 17] for the fermion action in our simulation. Therefor, one makes the most general ansatz for the Dirac operator,

$$D_{\mathrm{CI}} = \sum_{\alpha=1}^{16} \Gamma_\alpha \sum_{p \in \mathcal{P}_\alpha} c_p^{(\alpha)}(U) \ , \tag{3.5}$$

which formulates it as a sum over all 16 elements Γ_α of the Clifford algebra, where each element is multiplied with coefficients $c_p^{(\alpha)}(U)$, consisting of path ordered products of gauge links U. The number of coefficients is governed by respecting all lattice symmetries and the γ_5-hermiticity.

This ansatz is then plugged into the Ginsparg-Wilson relation (2.19), which leads to a set of coupled algebraic equations. In principle, a solution of this set of equations can give rise to an exact solution of (2.19), but only if one allows for infinitely many terms. For practical reasons the lengths of the paths are truncated and thus one

obtains an approximate solution. In our case, we allow for paths up to length 4, which (except for one term) are all lying within the hypercube.

In our simulation the coefficients have been fixed for one set of bare parameters and have then been used further for all our sets of gauge configurations (see [43, 40] for details) to guarantee good comparability. Details about the coefficients are given in App. A. As a consequence, we now have an additive mass renormalization in each set of configurations. CI fermions were used quite extensive within the Bern-Graz-Regensburg (BGR) collaboration in quenched and dynamical simulations. Results of that analyses can be found in [44, 45, 46, 47, 48, 49, 50, 51, 52, 53, 43, 54, 40, 6, 7].

3.3 Hybrid Monte Carlo algorithm

In Sec. 2.2 it became clear that the only way to deal with integrals like Eq. (2.7) is to use a Monte-Carlo simulation. In this section we want to discuss the algorithm we use to perform the fermionic integral, it is a Hybrid Monte-Carlo (HMC) algorithm [55]. The HMC algorithm seems to be most suitable for our goal.

Since one cannot calculate the fermion determinant directly, this problem can be overcome by treating this determinant as an additional weight factor when producing the gauge field configurations. More precisely, the gauge fields are distributed according to (in case of two dynamical quark flavors which we use in our case)

$$P(U) \propto \frac{1}{Z}\, e^{-S_{\mathrm{G}}[U]}\, \det(D_u)\, \det(D_d)\ . \tag{3.6}$$

If the two quarks are mass degenerate ($D_u = D_d = D$) and D is γ_5-hermitian, the product of the two determinants is real and positive and can thus be really interpreted as a weight factor.

Let us now say a few words about fermionic and bosonic Gaussian integrals. The crucial concept, which is needed, is to introduce pseudofermion fields $\phi = (\phi_R, \phi_I) \in \mathbb{C}^N$ [56]. These pseudofermion fields are bosons with the same number of degrees of freedom as the fermions. One can find a relation between the determinant and the pseudofermion fields,

$$\det(D^\dagger D) = \pi^{-N} \int \mathcal{D}[\phi_R]\mathcal{D}[\phi_I]\, e^{-\phi^\dagger (D^\dagger D)^{-1}\phi}\ . \tag{3.7}$$

With this relation we are now able to replace the integral over fermionic Grassmann variables by an integral over bosonic variables. And such an integral can then be calculated on a computer using the mentioned HMC algorithm.

For the HMC we need a generalization of the Hamiltonian evolution for a system of classical mechanics in a fictitious HMC time to our system of gauge fields $U_\mu(n)$.

For that purpose we introduce traceless hermitian matrices $P_\mu(n) \in \mathrm{su}(3)$, which act as conjugate momenta for the gauge fields $U_\mu(n)$. We now can define the time derivative of $U_\mu(n)$ as

$$\dot{U}_\mu(n) = i\, P_\mu(n)\, U_\mu(n) \ . \tag{3.8}$$

Then, a Hamiltonian H can be defined as

$$H = \frac{1}{2} \sum_{n,\mu} \mathrm{tr} \left[P_\mu(n)^2 \right] + S_\mathrm{G} + \phi^\dagger (D^\dagger D)^{-1} \phi \ . \tag{3.9}$$

The equation of motion for the conjugate momenta P is obtained via the relation $\dot{H} = 0$,

$$\dot{H} = \sum_{n,\mu} \mathrm{tr} \left[P_\mu(n) \dot{P}_\mu(n) \right] + \dot{S}_\mathrm{G} + \phi^\dagger \frac{d}{dt} (D^\dagger D)^{-1} \phi = 0 \ . \tag{3.10}$$

This equation results in

$$\dot{P} = f(U, \dot{U}, P) \ , \tag{3.11}$$

which gives the evolution equation in HMC time. The function f is called the fermion force. Evaluating this force function for, e.g., Wilson quarks is not complicated, since this type of quarks involve only one link field $U_\mu(n)$ connecting neighboring sites. In our case, however, paths up to length four, coming from D_CI, have to be considered. Independently from that, calculating the fermion force is the most costly part of the simulation. A more detailed description of the procedure can be found in [57].

Having now all equations at hand, the whole procedure to update the gauge fields looks as follows:

1. **Pseudofermion fields:** Generate the pseudofermion fields $\phi = D\xi$, where ξ is distributed according to $e^{-\xi^\dagger \xi}$.

2. **Conjugate momenta:** For the initial set of gauge fields $\{U_\mathrm{ini}\}$ generate a set $\{P_\mathrm{ini}\}$ according to $e^{-\mathrm{tr}(P_\mathrm{ini}^2)}$.

3. **Evolution of fields:** Evolve the gauge fields and conjugate momenta consistent with their equations of motion to the final sets $\{U_\mathrm{fin}\}$ and $\{P_\mathrm{fin}\}$.

4. **Accept/Reject step:** To correct for numerical errors close with an accept/reject step, i.e., accept the new configuration with $\exp(-S_\mathrm{fin} + S_\mathrm{ini})$.

The only thing still to be clarified is step 3. We need to find an integration scheme for the equations of motion. Such an integration scheme should be area preserving and reversible. At the same time it should keep the change in the action small, since a big ΔS leads to a poor acceptance rate. One possibility for such an integration

scheme is the leapfrog integration (also known as Störmer-Verlet method), which we use and briefly discuss now.

The fictitious time in which we evolve our system of fields, is called HMC time. The HMC time separation (trajectory length) between two consecutive gauge configurations is denoted by T. This interval is divided into N small time steps of length τ via $\tau = T/N$. In all our simulations we used $T = 1$. One starts with initial gauge fields U_0 and the conjugate momenta P_0. The next step is to evolve the conjugate momenta with a half step,

$$P_{\frac{1}{2}} = P_0 - \frac{\tau}{2} f \ . \tag{3.12}$$

Here, f is the fermion force defined in (3.11). Then the gauge fields and the conjugate momenta are evolved alternately $N-1$ times, i.e., $k = 1, \ldots, N-1$, with a full step in τ,

$$U_k = \exp\left(i\,\tau\, P_{k-\frac{1}{2}}\right) U_{k-1} \ , \tag{3.13}$$

$$P_{k+\frac{1}{2}} = P_{k-\frac{1}{2}} - \tau\, f \ . \tag{3.14}$$

The final steps for both fields are given by

$$U_N = \exp\left(i\,\tau\, P_{N-\frac{1}{2}}\right) U_{N-1} \ , \tag{3.15}$$

$$P_N = P_{N-\frac{1}{2}} - \frac{\tau}{2} f \ . \tag{3.16}$$

Then, of course, the final set of gauge fields $\{U_f\}$ is identical to the set $\{U_N\}$.

At that stage, it is clear why the third point of the procedure, the evolution of the fields, is the most costly one. The fermion force f, and thus the inverse of $D^\dagger D$, has to be calculated N times. Logically, one should care for using a highly optimized code – at least concerning that part. This task is discussed a bit more general now.

3.4 Speeding up the code

In this section we want to cover all concepts which are implemented to increase the run-time of our code.

3.4.1 Alternative integration schemes

An alternative to the leapfrog scheme would be an Omelyan integrator [58, 59], which was tested but not used for production runs, however. Let us denote the evolution of the gauge field U or the conjugate momentum P by some time τ with

$U(\tau)$ or $P(\tau)$, respectively. The leapfrog integrator from above evolves the system of fields according to

$$\Big[\, P(\tau/2)\, U(\tau)\, P(\tau/2) \,\Big]^N \,, \tag{3.17}$$

such that $N\tau$ is the length of the trajectory. The deviation from an exact solution is of the order of $\mathcal{O}(\tau^2)$. This deviation, i.e., the coefficient in front of the $\mathcal{O}(\tau^2)$ term, is reduced by the Omelyan integrator. There, the order in evolving the fields is

$$\Big[\, P(\lambda\tau)\, U(\tau/2)\, P((1-2\lambda)\tau)\, U(\tau/2)\, P(\lambda\tau) \,\Big]^N \,. \tag{3.18}$$

The tunable parameter λ for this order has the optimal value at $\lambda = 0.193183$ [59].

Finally we want to mention that also integrators using multiple time scales [60, 61] have been tested, but not used further. The reason is, that for our lattice size we could not find any significant speeding up of the code. Thus we decided not to change the code during the production runs.

3.4.2 Mass preconditioning

To be able to go to smaller quark masses, we utilize mass preconditioning (often called "Hasenbusch trick") [62]. The basic idea is to split the pseudofermion action into two (or more) parts, separating the small and the large eigenvalues (forces) of the Dirac matrix. I. e., the UV part of the spectrum is approximated by a fermion matrix with a large quark mass, since this part of the spectrum depends only very little on the quark mass. The splitting is achieved through the identity

$$\det(D^\dagger D) = \det(M^\dagger M) \det\left(\frac{1}{M^\dagger}\, D^\dagger D\, \frac{1}{M}\right) \,, \tag{3.19}$$

where M is a fermion matrix with heavier quark mass. For details on the calculations we refer to [57]. Only the key point will be presented here. The parameter m_{HB}, which amounts to an additional mass, is deduced from an educated guess [57]. Using N_{PF} pseudofermions, the mass shift is given by

$$m_{\mathrm{HB}}^{(i)} = \begin{cases} \left(2^{N_{\mathrm{PF}}-i}\, \lambda_{\mathrm{min}}^{i}\right)^{1/N_{\mathrm{PF}}} & ,\ 1 \leqslant i < N_{\mathrm{PF}} \\ \\ 0 & ,\ i = N_{\mathrm{PF}} \end{cases} \,. \tag{3.20}$$

Here, λ_{min} is the assumed smallest eigenvalue of the Dirac matrix.

In our case we always use two pseudofermions. Details on the assumed smallest eigenvalues can be found in Tab. 3.1 on page 23.

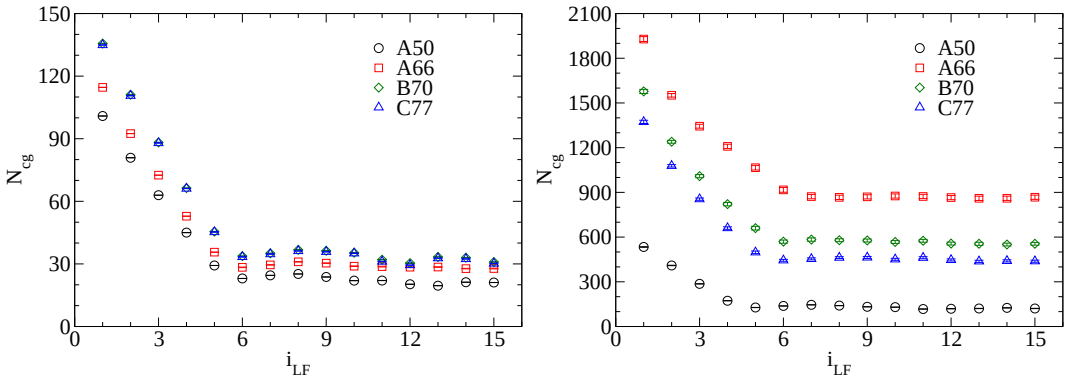

Figure 3.2: *The average number of conjugate gradient iterations needed is plotted against the first leapfrog steps for several sets of gauge configurations. On the l.h.s. we plot this number for the heavier Hasenbusch fermion, the lighter (the one without the additional mass shift) is found on the r.h.s*

3.4.3 Developments on the conjugate gradient solver

As pointed out before, the most costly part in the HMC is the calculation of the force. The main part of this task is to invert $D^\dagger D$, i.e., solving a linear system, which is done with the conjugate gradient method in our case. This has to be done N times, i.e., for each time step τ. Since the right hand side is fixed during the leapfrog integration, the fermion matrix is evolving smoothly in time. Hence, the previous solutions can help us making a reasonable guess for the solution at any given time. This method is called a chronological inverter [63]. In our case we use 12 previous solutions. In Fig. 3.2 we show the numbers of needed conjugate gradient steps, N_{cg}, for the two Hasenbusch fermions for several gauge configuration sets. One can clearly see, that these numbers are significantly higher for the first leapfrog steps, where no or only a few previous solutions are available. It is also obvious, that in both cases a plateau is formed, beginning with $i_{\mathrm{Lf}} = 6$. Thus, we could also take into account only 6 previous solutions, but the overhead caused by the 6 additional matrix vector multiplications is negligible for the run-time of the code. We want to stress that one has to take special care for the reversibility of the integration algorithm when using this method.

In order to ensure reversibility in the molecular dynamics evolution one should work with double precision accuracy. However, this has not as a consequence that each inversion has to be done in double precision. In [64] a method was suggested, which uses an elaborate combination of single and double precision arithmetics. The system we want to solve is $D^\dagger D x = \mathbf{A}x = b$. The final accuracy is chosen as $\varepsilon = 10^{-7}$

and then the procedure reads:

1. Compute $r_k = b - \mathbf{A}x_k$ in double precision.

2. If $|r_k| < \varepsilon|b|$, exit.

3. Solve $r_k = \mathbf{A}t_k$ in single precision with accuracy $\varepsilon_{\rm s}$, with t_k^* being the solution.

4. Set $x_{k+1} = x_k + t_k^*$.

5. Go to **1.**

To give a rough estimate, the reduction in run-time per gauge configuration was, e.g., about 33% for set C77.[1]

3.5 Run parameters

We generated seven different sets of gauge configurations. The size of the lattice in spatial direction is $L_s = 16$ and the temporal extend is twice the spatial one, $L_t = 32$. All input parameters, i.e., the gauge coupling β_1, the assumed plaquette u_0, the bare mass parameter m_0 and the assumed minimal eigenvalue $\lambda_{\rm min}$ can be found in Tab. 3.1. We also show there the values of the lattice spacing a, the pion mass m_π, the AWI-mass $m_{\rm AWI}$ and the total number of analyzed configurations $N_{\rm conf}$.

3.6 Autocorrelation

Having produced the gauge configurations, one has to analyze their autocorrelation, since they are normally still highly correlated. Thus, we have to find a way to decide (a) where we start our measurements, and (b) how many configurations we skip between two measurements. Let us start with the former point.

We have two quantities at hand to decide how many gauge configurations we skip until the first measurement, these are the plaquette value and the number

[1] Let me add here a personal comment. Some time ago I found an interesting paper [65]. The key point of this work is the following. Due to Moore's law the computer power doubles every 18 months. Thus, in some cases it can be more profitable to "slack" for some time before beginning the calculations. And the "magic number" is 26 months. Each project lasting longer than these 26 months can be started with a delay, which increases with the project duration. So, what are my conclusions out of that? Since this work took far more that 26 months (i.e., about 44 moths), it would have been better to be the "lazy bum at the beach" for about 14 months and only then start to work on all that ... But who would have paid me?

Set	β_1	u_0	m_0	$\lambda_{\min}$	a [fm]	m_π [MeV]	m_{AWI} [MeV]	N_{conf}
A50	4.70	0.45	-0.050	0.015	0.150(1)	525(5)	40(1)	200
A66	4.70	0.45	-0.066	0.015	0.135(1)	250(8)	9(1)	200
B60	4.65	0.45	-0.060	0.010	0.150(1)	470(4)	31(1)	300
B70	4.65	0.45	-0.070	0.010	0.141(1)	296(6)	12(1)	200
C64	4.58	0.45	-0.064	0.010	0.158(1)	519(5)	37(1)	200
C72	4.58	0.45	-0.072	0.010	0.151(1)	419(4)	23(1)	200
C77	4.58	0.45	-0.077	0.010	0.145(1)	319(5)	14(1)	300

Table 3.1: *Run parameters for the different sets of gauge configurations. λ_{min} is the assumed smallest eigenvalue of the Dirac matrix, which is needed in the calculation of m_{HB} in Eq.* (3.20)*. a is the lattice spacing in Fermi, obtained with the method described in Sec. 2.6. For details on the pion mass m_π (given here in the mass dependent scheme, discussed in Sec. 4.6) see Sec. 6.2. The AWI-mass m_{AWI} is outlined in Sec. 7.2. In the last column the total number of independent configurations can be found.*

of needed conjugate gradient iterations in the accept/reject step of the molecular dynamics evolution, N_{cg}. On the left hand side of Fig. 3.3 we show the first 300 plaquette values for the sets A50, B60 and C64. Sets A50 and B60 are the only ones which were generated with a "cool" starting configuration, i.e., all $U_\mu(n) = 1$. All other sets were generated by taking an existing gauge configuration and changing the values of β_1 and m_0 smoothly to the new values, which then served as starting configuration. One can clearly see, that sets A50 and B60 are equilibrated after roughly $\mathcal{O}(100)$ configurations. Set C64 does not show such a behavior due to the "partly equilibrated" starting configuration. On the right-hand side of Fig. 3.3 we plot N_{cg}, which is the number of needed conjugate gradient steps for the lighter Hasenbusch fermion in the accept/reject step, for the first 300 configurations and the same behavior as for the plaquette can be seen. Therefrom we mostly decided to skip the first 99 gauge configurations and start the measurement with the 100-th configuration. The detailed numbers are given in Table 3.2.

Now we know where to start the measurements. The next task will be to clarify the second point: How many configurations will be skipped within two measurements? A useful tool to answer this question is the integrated autocorrelation time $\tau_{\mathrm{int}}^{[O]}$, which is defined through

$$\tau_{\mathrm{int}}^{[O]} = \frac{1}{2} + \sum_{t=1}^{\infty} \frac{\Gamma^{[O]}(t)}{\Gamma^{[O]}(0)} \ , \tag{3.21}$$

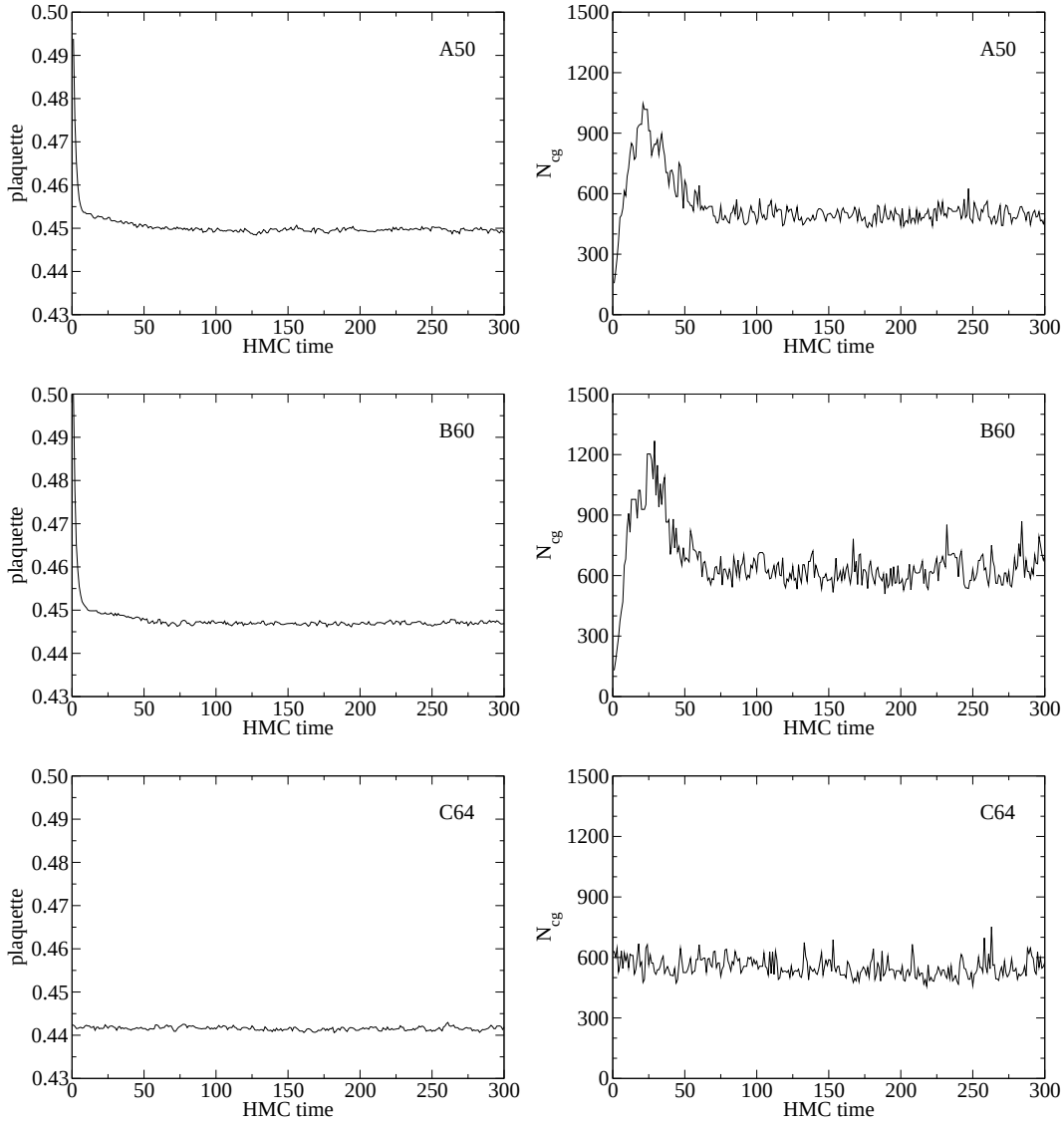

Figure 3.3: *For the sets A50, B60 and C64 we show on the l.h.s. the value for the plaquette and on the r.h.s. the number of needed conjugate gradient steps in the accept/reject step, N_{cg}.*

Set	N_{skip}	$\tau_{\mathrm{int}}^{[\mathrm{plaq}]}$	$\tau_{\mathrm{int}}^{[N_{\mathrm{cg}}]}$
A50	99	2.93	3.91
A66	99	3.59	2.32
B60	114	2.85	3.94
B70	99	3.64	1.91
C64	99	2.81	2.08
C72	99	3.45	2.24
C77	49	3.77	3.37

Table 3.2: *For each set of gauge configurations we show the numbers of skipped configurations and the integrated autocorrelation times for the plaquette values and the number of needed conjugate gradient inversions, N_{cg}.*

serves as a quantity of the statistical efficiency of the observable O. $\Gamma^{[O]}(t)$ is called the autocorrelation function,

$$\Gamma^{[O]}(t) = \Big\langle \big(O(t_0) - \langle O\rangle\big)\big(O(t_0+t) - \langle O\rangle\big) \Big\rangle \ . \tag{3.22}$$

For practical reasons, the sum in (3.21) is truncated at some upper value t_{max}, which is in our case the point, where the autocorrelation data becomes to noisy. This number gives a lower bound for the autocorrelation length. Therefrom, one has a rough estimate how many configurations should at least be skipped between two measurements. Of course, these numbers could be orders of magnitude higher if other observables are analyzed. In Tab. 3.2 we show the numbers, obtained with Eq. (3.21), for our sets of gauge configurations. According to these numbers we decided to analyze every fifth configuration in each set.

In Fig. 3.4 we plot, for all sets of gauge configurations, the pseudoscalar masses, calculated for each configuration separately (see Chap. 6 for details). If our choice of analyzing every fifth configuration is good enough, we should not see any significant correlation effect in this plot – and this is indeed the case. The measured values are nicely fluctuating around some central value (red lines), the peaks are a pure statistical effect (and are not included to get the average value). These peaks are due to the fact, that we still calculate the pion mass for one single configuration, which is, of course, a strongly fluctuating quantity, especially for lower masses like in the sets A66, B70 and C77.

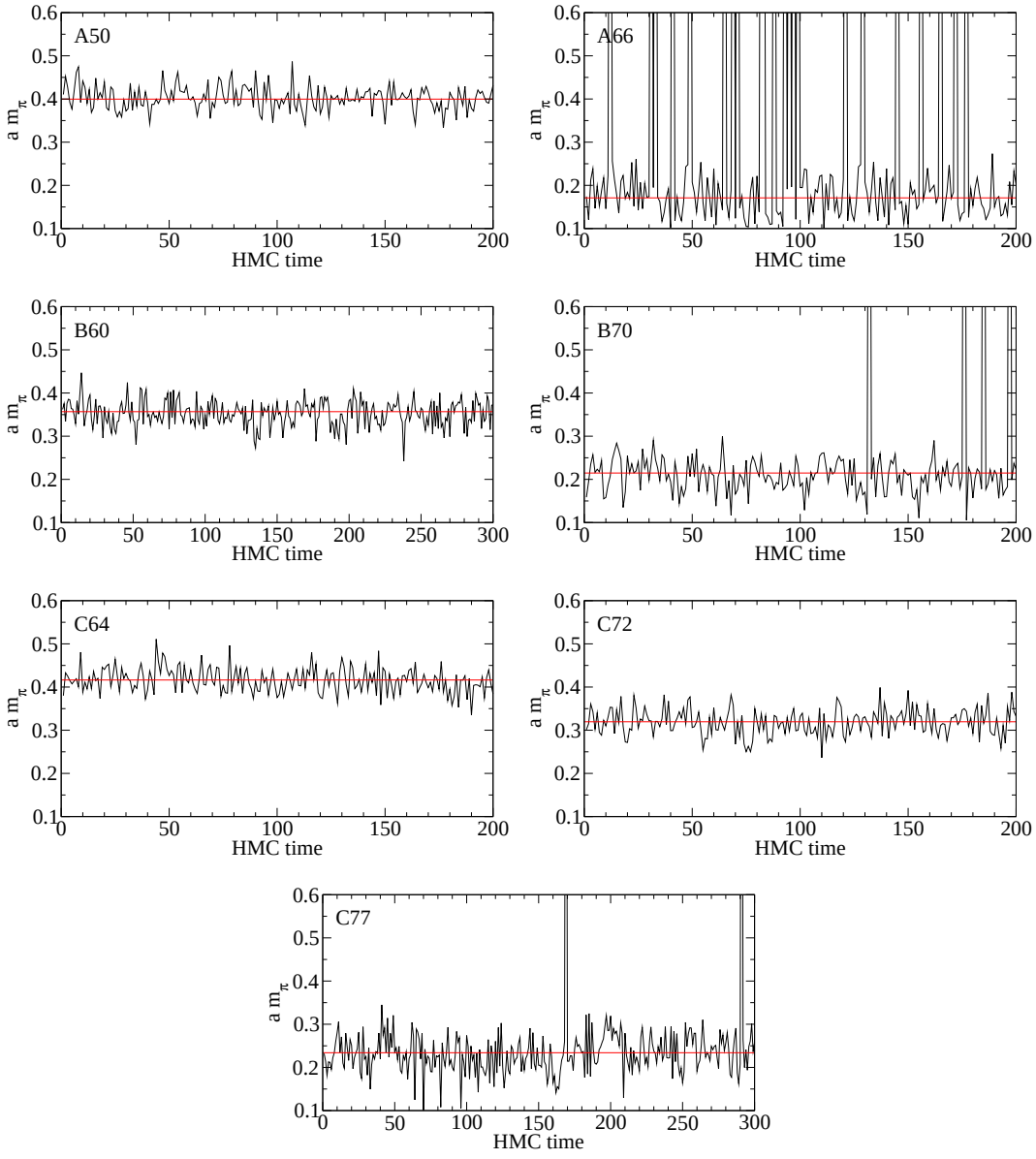

Figure 3.4: *For each set of gauge configurations the pseudoscalar mass (in dimensionless units) is plotted for each single configuration. The red lines denote the averaged values (calculated without the peaks).*

Set	CPUh	$\overline{N_{\mathrm{cg}}} \cdot \max\left(\tau_{\mathrm{int}}^{[\mathrm{plaq}]}, \tau_{\mathrm{int}}^{[N_{\mathrm{cg}}]}\right)$
A50	66.5	2129
A66	293.2	6818
B60	76.1	2743
B70	166.1	6000
C64	67.3	1566
C72	101.2	3082
C77	152.1	5518

Table 3.3: *For each set of gauge configurations we give details about the number of CPU hours we need to generate one gauge configuration (second column) and the product of the averaged number of conjugate gradient steps with the maximum of the integrated autocorrelation times (third column).*

3.7 Numerical costs

From the previous section we learned that not each generated configuration should be used in the final analysis. This fact, of course, also increases the computational costs for producing independent configurations. Thus, we now outline some details concerning this topic.

In [66] an empirical formula for the costs of dynamical HMC simulations can be found, it reads

$$€ \propto L^5 \, a^{-7} \left(\frac{m_\pi}{m_\rho}\right)^{-6} \quad . \tag{3.23}$$

Since we only use lattices of size $16^3 \times 32$, the factor coming from the volume, L^5, can be ignored in our case. In this formula also the autocorrelation time τ_{int} enters via the quark mass and the costs are given in units of Tflop years, a quantity which we do not have at hand in our case. Hence, we take as the "costs" of our simulation the product of the averaged numbers of conjugate gradient steps needed in the accept/reject step, $\overline{N_{\mathrm{cg}}}$, with the maximum of the two available autocorrelation times from Sec. 3.6. In Table 3.3 we give the details on the CPU hours (CPUh) we need to generate one individual gauge field configuration and the mentioned product for the costs.

We now want to check if (at least the qualitative behavior of) Eq. (3.23) is fulfilled here. Therefore, we plot in Fig. 3.5 the costs against the lattice spacing (left plot) and against the ratio m_π/m_ρ (right plot). One can recognize, that the dependence on the lattice spacing can be reproduced qualitatively, although we are not able to

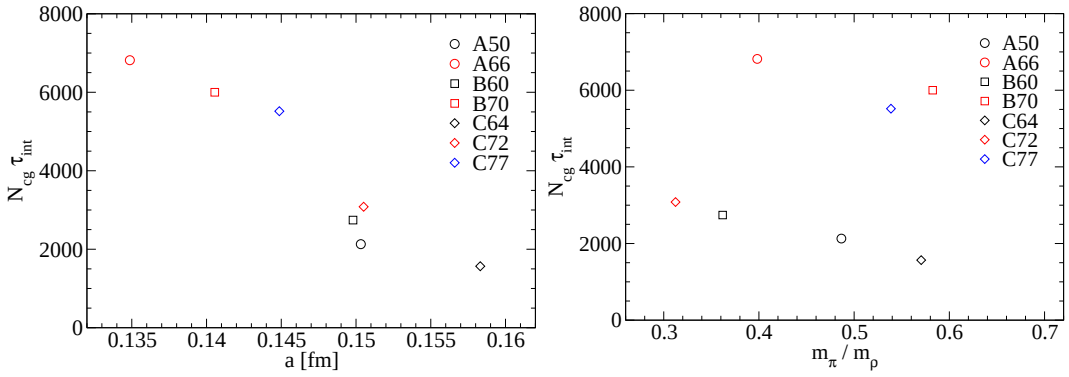

Figure 3.5: *L.h.s.: For each set of gauge configurations we plot the numerical costs as a function of the lattice spacing a. R.h.s.: For each set of gauge configurations we plot the numerical costs as a function of the mass ratio m_π/m_ρ.*

get the right exponent for a. For the dependence on the mass ratio, however, the situation is rather different from the expected behavior. This may be due to the (too) simple quantity which we take as the numerical costs and the fact that we ignore the effect coming from the lattice spacing.

3.8 The change in the Hamiltonian

Since we introduced the conjugate momenta P, we describe a microcanonical ensemble of a classical system with a Hamiltonian H. For exact solutions of the equations of motion (MD equations), the Hamiltonian would be a constant of motion and the configurations all would lie on a surface of constant energy. Thus, each created configuration would be accepted. However, due to the discretization with a MD time step τ, numerical errors are introduced and the Hamiltonian energy is not invariant. We denote this change by ΔH. Each calculated gauge configuration is then accepted with a probability $e^{-\Delta H}$. The area preserving property of MD leads to an inequality [67],

$$e^{-\langle \Delta H \rangle} \leqslant \left\langle e^{-\Delta H} \right\rangle = 1 \ . \tag{3.24}$$

Due to this inequality $\langle \Delta H \rangle$ has to be a positive, small number. This is indeed the case in our simulations. The evolution of ΔH in units HMC time can be seen in Fig. 3.6 and the detailed numbers are given in Tab. 3.4.

However, for some of the runs (i.e., runs A66, B60, B70, C77) the value for $\langle \Delta H \rangle$ is getting large. This increase is coming from spikes in the individual values for ΔH during the creation of the gauge field configurations, see Fig. 3.6. Since the

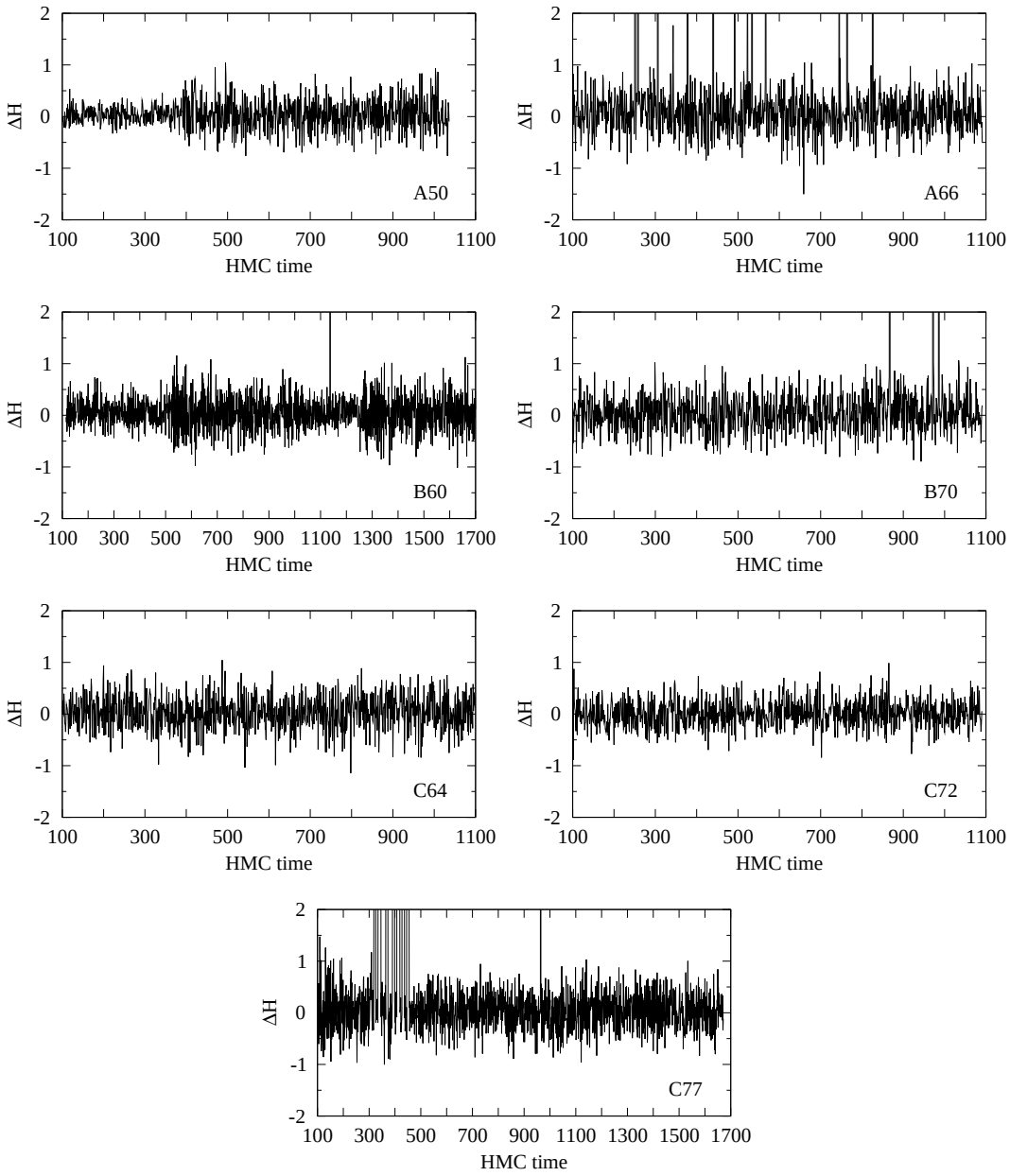

Figure 3.6: *We plot ΔH against the HMC time starting from the point of equilibration.*

Set	$\langle \Delta H \rangle$	$e^{-\langle \Delta H \rangle}$	$\langle e^{-\Delta H} \rangle$
A50	0.036(9)	$0.964(^{+0.009}_{-0.009})$	1.001(9)
A66	1.734(917)	$0.177(^{+0.265}_{-0.106})$	1.002(13)
B60	1.097(1050)	$0.334(^{+0.618}_{-0.217})$	0.998(8)
B70	0.823(645)	$0.439(^{+0.397}_{-0.209})$	1.019(11)
C64	0.038(11)	$0.963(^{+0.010}_{-0.010})$	1.017(11)
C72	0.014(8)	$0.986(^{+0.008}_{-0.008})$	1.020(9)
C77	0.377(53)	$0.686(^{+0.038}_{-0.036})$	0.983(10)

Table 3.4: *Averages of ΔH and their exponentials for each run. We only included the equilibrated configurations in our calculations.*

acceptance of a configuration is given by $e^{-\Delta H}$, none of the proposed configurations was accepted.

Such spikes have already been observed in other simulations with dynamical fermions [20, 68]. Two possible reasons can cause such a spike. One is the instability of the HMC for large step sizes in the MD evolution, cf. Ref. [69]. The other one, and this is most likely the case here, is that the Dirac operator can develop very small eigenvalues which lead to these spikes in the derivative of the action.

3.9 Stability of the algorithm

In this section we shortly discuss the stability of the algorithm used. In general, the eigenvalues of $D^\dagger D$ are positive semi-definite (not positive definite), if D is some lattice Dirac operator. Assuming that one could integrate the HMC trajectories exactly, no problems would be encountered, since small eigenvalues lead to large revertive forces in the HMC. Thus, exact zero modes are avoided in the algorithm. However, due to a finite step size τ in the integration, this back driving force may be smaller than it would be in an exact integration scheme, and so, a very small eigenvalue can cause an instability.

If a notably small eigenvalue appears during the MD evolution, the conjugate gradient solver for calculating the fermion force will need many more iterations to arrive at the given precision. Or, in other words, the inverse of the number of needed CG steps is strongly related to the smallest eigenvalue of $D^\dagger D$. The distribution of $1/N_{\mathrm{cg}}$ for a given ensemble is approximately a Gaussian [64]. As long as the mean is considerably larger than the standard deviation (e.g., the authors of Ref. [70] quote $\mu \geqslant 3\sigma$), the algorithm setup is safe. This condition is most crucial for small pion

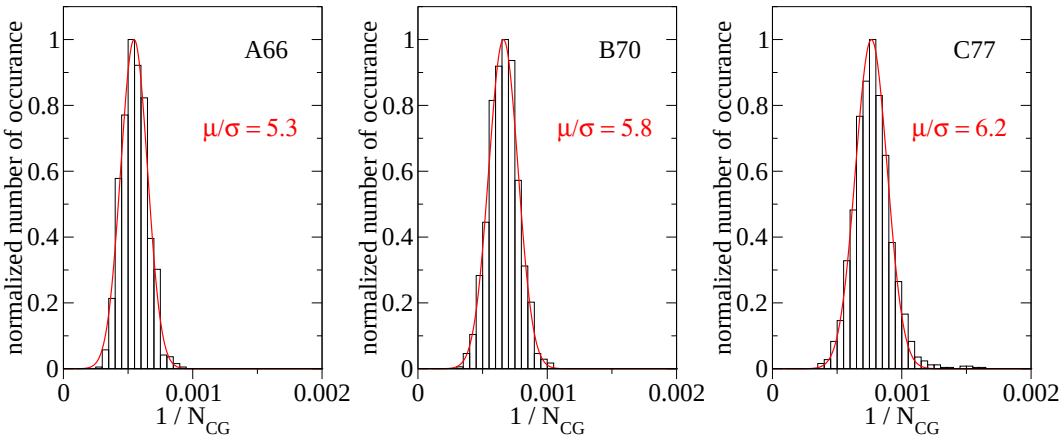

Figure 3.7: *A plot of the normalized histogram of* $1/N_{cg}$ *for runs A66, B70 and C77. The red line is a fit to the function* $\exp(-(x-\mu)^2/2\sigma^2)$ *and the ratio of* μ/σ *is given in each plot.*

masses.

In Fig. 3.7 we plot the histograms of $1/N_{\rm cg}$ for the smallest pion mass at each value of the gauge coupling. Also a fit of the histogram to a Gaussian is included. One can see, that there is a clear separation of the Gaussian shaped curve to the origin. Even for the worst case scenario, i.e., run A66, we find $\mu/\sigma \approx 5.3$. We thus conclude that our implementation is safe in the sense, that no negative eigenvalues of the Dirac operator are developed.

Chapter 4

Hadron spectroscopy

4.1 Euclidean correlation functions

In the beginning of Chap. 2 we already introduced the so-called correlation function or correlator in Eq. (2.8). This object is the main tool in hadron spectroscopy. From Eq. (2.8) we see that the correlator $C(t)$ can be expressed as a path integral. One can then start integrating out the fermionic part and generate gauge field configurations with the methods explained in Chap. 3.

To extract masses of hadrons using correlators, one has to insert suitable hadron interpolators for the operators O_1 and O_2 in Eq. (2.8). How these interpolators will look in detail is explained in Sec. 4.3 and App. B. Evaluating the expression for the correlator then gives [11]

$$C(t) = \sum_k a_k \, e^{-tE_k} \ , \tag{4.1}$$

which is a sum over all k states with energy levels E_k. The coefficients a_k give us the overlap of the lattice operator O with the physical state k,

$$a_k = \left|\langle 0|O|k\rangle\right|^2 \ . \tag{4.2}$$

Since in lattice QCD one uses natural units, energy and mass are equal to each other. However, the energy levels we speak of have to be compared to the energy levels in the continuum. For the following discussions we want to stress, that the expressions 'energy (level)' and 'mass' should have the same meaning. If we speak of a 'state', this cannot only be meant as a one-particle state, but also can be a scattering state, made out of two or more particles.

From Eq. (4.1) we see that the correlator is built of several states, all having different energies (in a finite volume). Since the ground state has the smallest mass of all states, it asymptotically contributes most to $C(t)$ due to the exponential decay. As a consequence, one is able to extract the ground state mass if t is large enough and thus the higher excited states are exponentially suppressed. This can be done by, e.g., a single exponential fit. The time range in which this fit is performed can

be fixed using the so-called effective mass, defined by

$$m_{\text{eff}}(t) = \ln \frac{C(t)}{C(t+1)} \ . \tag{4.3}$$

A plot of this quantity against t will show a plateau behavior in some time range $[t_1; t_2]$. The reason for such a behavior is the following. At the time t_1 the exponential suppression of the higher excited states is so strong, that one can assume $C(t) \propto e^{-tE_0}$, where E_0 is the energy level of the ground state. Applying then Eq. (4.3) leads to a constant for m_{eff}. Actually, the plateau in m_{eff} should not break down, since the exponential suppression is getting stronger with greater t. One reason for an upper boundary t_2 of the fit range is simply that the signal is getting worse if t is approaching the symmetry point $t = L_t/2$. This is due to the fact, that the correlators in Eq. (4.1) actually have the form

$$C(t) = \sum_k a_k \left[e^{-tE_k} + e^{-(L_t - t)E_k} \right] \ . \tag{4.4}$$

The second term in the square brackets comes from an antiparticle, which runs backwards in time. Since the expression in square brackets is $\propto \cosh[(t - L_t/2)E_k]$, we speak of a cosh-behavior of the correlator and leave out the second term in the square brackets for simplicity again. Another reason is, of course, that the signal gets exponentially weak with grater t and thus simply turns into pure noise.

The method just described works fine for the ground state for a lot of hadron channels. However, one usually does not only want to extract the ground state energy level but also one or more excitations. For this task the method will fail because the excitations appear only as sub-leading terms in the correlation function. Carrying out a multi-exponential fit is unstable, particularly in view of the noisy data on a finite number of gauge configurations. Furthermore, quantities related to the ground state are spoiled with admixtures of the excited states, which often reduce the fit range severely.

To overcome this problem, we now will present and discuss some methods which can deal with this unpleasantness.

4.2 Spectroscopy techniques for excited states

As seen before, the reliable separation of the ground and excited states, or even of different excited states, is a rather challenging enterprise. The brute-force least-squares fit to a finite sum of exponentials will only have promise if rather high statistics are available. Since this is not the normal case, other approaches towards that goal are used in hadron spectroscopy.

4.2.1 Bayesian methods

Here, one does not minimize the "ordinary" χ^2 functional, but uses instead

$$\widetilde{\chi}^2 = \chi^2 + \lambda\phi \ , \tag{4.5}$$

where ϕ is a stabilizing function of the fit parameters and λ a positive and real multiplier. This method has been used, e.g., in [71, 72]

4.2.2 Maximum entropy method

In the maximum entropy method the correlation function is written as the Laplace transform of a spectral density,

$$C(t) = \int_0^\infty dE\, \rho(E)\, e^{-tE} \ . \tag{4.6}$$

In the continuum the density function $\rho(E)$ should have peaks near the energy values which dominate the correlation function. On the lattice, it is a hard task to recover $\rho(E)$ with only a few values for $C(t)$.

This method is frequently used in statistical physics, but also applied by the lattice community [73, 74].

4.2.3 The variational method

The most promising method at the moment is the variational method [75, 76]. It is used by various collaborations, see for example [77, 78, 53], and provides reliable results for ground and excited states of several hadrons.

Since we exclusively use the variational method in our studies, we discuss this approach in more detail in the next section.

4.3 The variational method

As already stated above, the method of choice for our studies is the variational method [75, 76]. This method has a fundamental difference to the other methods discussed – it uses not only one correlator but a matrix of cross-correlators. Therefore one employs N different interpolators O_i, $i = 1, \ldots, N$, which all have the quantum numbers of the state of interest. Then this cross-correlation matrix is given by

$$C_{ij}(t) = \langle O_i(t)\, O_j^\dagger(0) \rangle \ . \tag{4.7}$$

In the Hilbert space this matrix can be expressed as

$$C_{ij}(t) = \sum_k \langle 0|O_i|k\rangle \langle k|O_j^\dagger|0\rangle \, e^{-tE_k} = \sum_k a_k^{(i)} \, a_k^{(j)*} \, e^{-tE_k} \ . \tag{4.8}$$

One immediately sees that the only time-dependent term is the exponential. This fact will be discussed in more detail below.

Considering a generalized eigenvalue problem (GEVP) normalized at some time slice $t_0 < t$,

$$C(t)v_k = \lambda_k(t, t_0)C(t_0)v_k \ , \tag{4.9}$$

we obtain the following behavior for the eigenvalues [75, 76]

$$\lambda_k(t, t_0) \propto e^{-(t-t_0)E_k}\left[1 + \mathcal{O}(e^{-(t-t_0)\Delta E_k})\right] \ . \tag{4.10}$$

In general, ΔE_k is the mass difference to the closest lying state. For the special case $t < 2t_0$ and a basis of N interpolators, ΔE_k is the difference to the first neglected state [79, 80],

$$\Delta E_k = E_{N+1} - E_k \ . \tag{4.11}$$

Thus, each eigenvalue represents one single state for large time distances, and this gives us the possibility to perform a (stable) two-parameter fit to the eigenvalue. This means the largest eigenvalue decays with the ground state mass, the second largest decays with the mass of the first excited state, etc. The technical procedure is the following:

1. Compute the cross-correlation matrix, including the interpolators of interest.

2. Solve the GEVP for each time-slice.

3a. Sort the eigenvalues according to their magnitude.

3b. Sort the eigenvectors according to order of the eigenvalues.

4. Perform a two-parameter fit to the eigenvalues in some time range $t_0 < t_{\min} \leqslant t \leqslant t_{\max}$.

To be able to identify the region where the eigenvalues should be fitted, we again use the concept of effective masses from Sec. 4.1.

We now want to shortly discuss the eigenvectors again. Since they should not depend on the time-slice t, see Eq. (4.8), we have an additional tool at hand, which can help us to identify a state in general and the time range for the fit, i.e., the region where also the vectors show a plateau behavior. To get some impression of a typical result of this analysis, we show in Figure 4.1 the eigenvectors of the ground

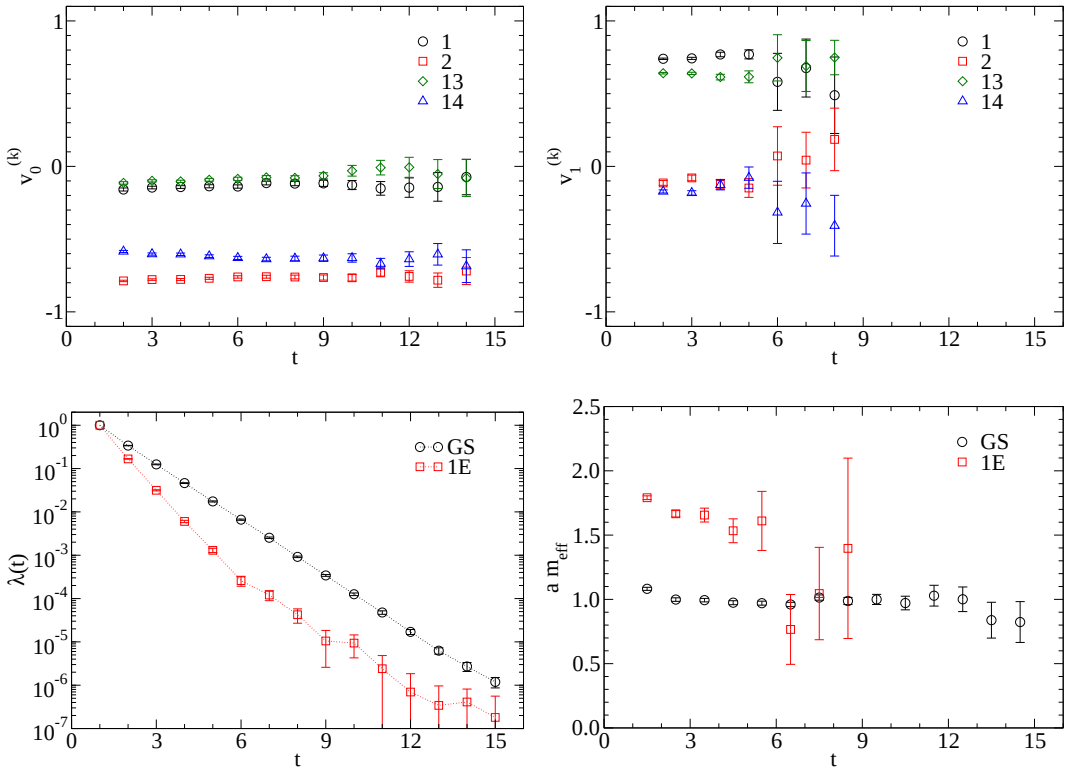

Figure 4.1: *In the first row we plot the eigenvector of the ground state, $v_0^{(k)}$, and the eigenvector of the first excited state, $v_1^{(k)}$. Below the eigenvalues for these states and the corresponding effective masses can be found. All results are for set A50.*

and first excited state and the eigenvalues with the corresponding effective masses for the positive parity nucleon of set A50. If only the effective mass is the basis for the decision where to fit the eigenvalue then one would naively fit the first excitation from $t = 2-6$. But when we also include the eigenvectors into this process, the time range shrinks by one time-slice to $t = 2-5$! However, this effect may be tiny here, but in other hadron channels the eigenvectors are often crucial to decide on the fit range.

Another point to be discussed here is the basis used in this analysis. Since one does not use a single correlator but a cross-correlation matrix, several interpolators O_i, which couple to the same hadron state, are necessary. In our simulation this request is achieved with two approaches. On the one hand we can describe a particle with interpolators which all have a different Dirac structure. For, e.g., the case of the nucleon we can use three different types of interpolators (with respect to the

Dirac structure),

$$O_N^{(1)} = \epsilon_{abc}[u_a^T\, C\, \gamma_5\, d_b]\, u_c\ , \tag{4.12}$$

$$O_N^{(2)} = \epsilon_{abc}[u_a^T\, C\, d_b]\, \gamma_5\, u_c\ , \tag{4.13}$$

$$O_N^{(3)} = i\,\epsilon_{abc}[u_a^T\, C\, \gamma_\mu\, \gamma_5\, d_b]\, u_c\ . \tag{4.14}$$

This leads as a first step to a 3×3 correlation matrix.

The other onset we make use of, is to include different quark sources on which we compute the quark propagators. These sources differ only by their widths. The detailed procedure is explained in the next Section 4.4, here we only mention, that for the nucleon, we can use two different widths of quark sources. Thus, the 3×3 correlation matrix grows by a factor of 8 and finally we can work with a 24×24 correlation matrix. Due to some numerical equalities it reduces to a 18×18 matrix for the case of the nucleon.

The most crucial ingredient in the variational analysis is the basis of interpolators. One can only *a posteriori* decide if one has chosen a reasonable basis or not. Thus, the "design" of the interpolators is some kind of an art with a big portion of physics.

The usage of the full $N \times N$ correlation matrix in a straight forward way, i.e., perform the diagonalization of the full $N \times N$ matrix, is normally not possible – although, according to the theory, the results should get better. The reason is, that increasing the number of interpolators in the matrix also increases the statistical noise. Therefore, one takes only a subset of $n \leqslant N$ interpolators and works with this smaller $n \times n$ matrix. Then, of course, the question arises: Which interpolators should be included? This question is highly non-trivial to answer! For the nucleon we have, as seen above, an 18×18 matrix. To try out every combination of interpolators means analyzing $2^{18} - 1 = 262,144$ different combinations – which is obviously impossible! Thus, one has to learn from previous combinations and has to rely on experience to try out only some promising subsets. In other words, it is some kind of a "trial and error" process. So we here arrive at the point from above: It is some kind of art. A typical number, independent of the hadron type, is $3 \lesssim n \lesssim 8$. In our case, we started analyzing each set of configurations separately and then tried to find a promising intersection of the several subsets, i.e., we tried to find one interpolator combination for all seven sets. This strategy worked out in the case of baryons, the situation for mesons is, however, more involved and we cannot always follow such a scheme.

Set	κ	N_κ	Width [fm]
A50	0.212	17	0.357
A66	0.210	20	0.356
B60	0.222	15	0.347
B70	0.305	8	0.256
C64	0.280	7	0.254
C72	0.280	7	0.241
C77	0.223	15	0.333

Set	κ	N_κ	Width [fm]
A50	0.1840	63	0.661
A66	0.1830	74	0.647
B60	0.1840	68	0.679
B70	0.1840	55	0.573
C64	0.1918	37	0.547
C72	0.1925	37	0.525
C77	0.1840	70	0.677

Table 4.1: *For each set of gauge field configurations we show the numbers for κ and N_κ, which are used in Eq.* (4.16) *and the resulting source width . On the l.h.s. the parameters for the narrow sources and on the r.h.s. the parameters for the wide sources are given.*

4.4 Smearing of quark fields

In the previous section we already discussed ways how to increase the number of possible interpolators which all describe the same hadronic channel. One method, which we use in our simulation, is smearing of the quark sources or sinks, respectively. More precisely, we here apply two different smearing techniques: Jacobi smearing [81, 82] and the creation of derivative sources (see, e.g., [83]). With this procedures we can on the one hand extend the basis of interpolators and on the other hand also improve the quality of the signal.

Let us discuss the Jacobi smearing. One acts on a point like quark field source S_0, which can in the following either be a source or a sink, with a smearing operator M,

$$S_s = M\, S_0 \ , \tag{4.15}$$

where this smearing operator M is defined as

$$M = \sum_{n=0}^{N_\kappa} (\kappa\, H)^n \ . \tag{4.16}$$

Actually, this is the application of a polynomial of a hopping term H, which is given by

$$H(n,m) = \sum_{k=1}^{3} \left[U_k(n,t)\delta_{n+\hat{k},m} + U_k^\dagger(n-\hat{k},t)\delta_{n-\hat{k},m} \right] \ . \tag{4.17}$$

It is obvious from Eq. (4.17) that each time-slice t is smeared individually. The resulting quark fields have approximately a Gaussian shape. The width of the cre-

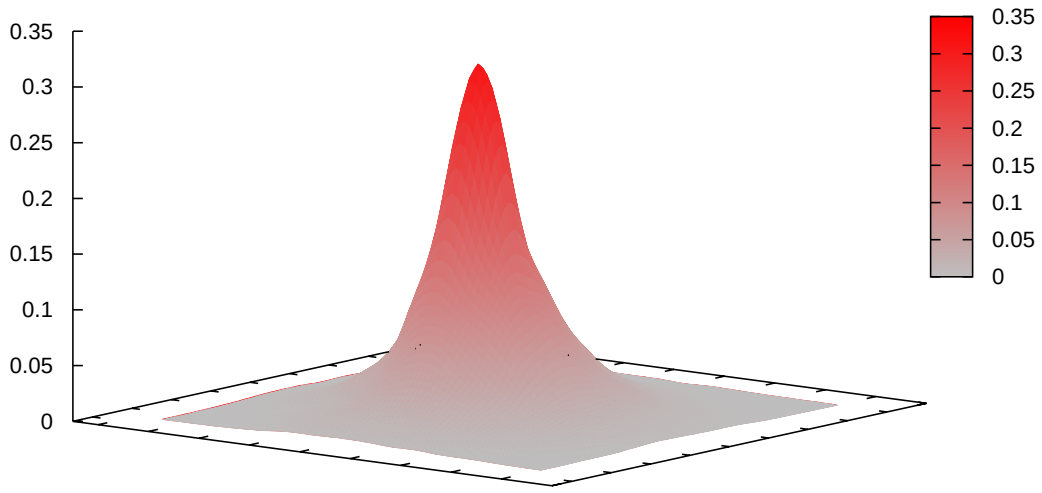

Figure 4.2: *A 3d plot of a Jacobi smeared quark field in some arbitrary units.*

ated sources can be controlled by the parameters κ and N_κ. In Tab. 4.1 we give the detailed numbers for each set of gauge configurations. In our simulation we use two different widths of sources and call them "narrow" (index n) and "wide" (index w). Originally this smearing procedure was used to suppress contributions from excited states. In our approach, however, we can improve the overlap of interpolators with both the ground state and low excitations to extract these signals at the same time. For applications of these method see, for example, [46, 47].

Another method, we also work with, is to smear the quark fields such that the resulting field may exhibit nodes, i.e., it is a P-wave like field [83]. This is achieved by applying a covariant lattice derivative operator (which is nothing but a difference operator) on a smeared source, and in our case we take the wide source. We denote these derivative sources by $S_{\partial_k} = P_k S_w$ and the derivative operator P_k is

$$P_k(n,m) = \frac{1}{2}\left[U_k(n,t)\delta_{n+\hat{k},m} - U_k^\dagger(n-\hat{k},t)\delta_{n-\hat{k},m}\right] \ . \tag{4.18}$$

To get an impression of this two constructs we show in Figs. 4.2 and 4.3 both a Jacobi smeared quark field and a P-wave like field. In these plots the sources are calculated only for one single gauge configuration, since this is not a gauge-invariant object and would vanish in the ensemble average.

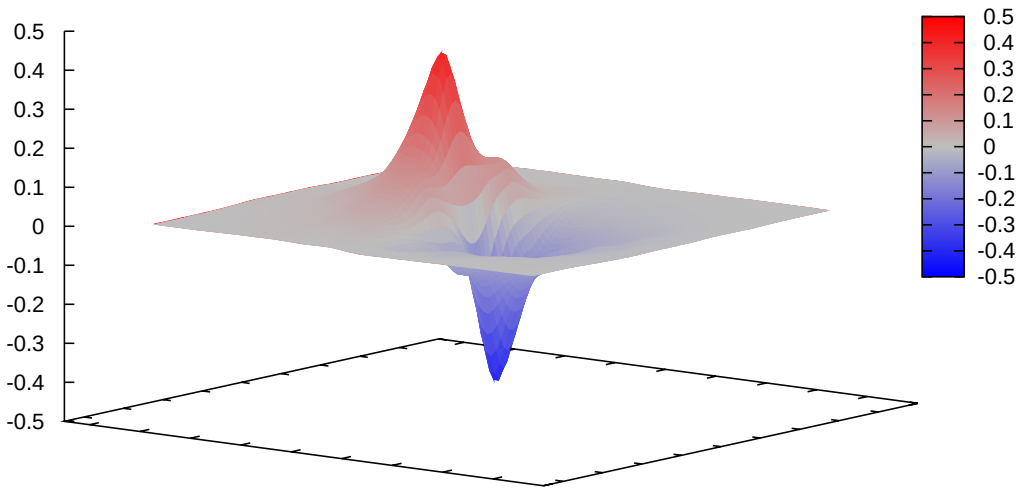

Figure 4.3: *Same as Fig. 4.2, now for a derivative smeared field.*

4.5 Gauge link smearing

In the previous section we discussed the smearing of quarks fields, from which the quark propagators are computed subsequently. However, another type of smearing is widely used in lattice simulations, it is the gauge link smearing. There, a local gauge link is replaced by an "average" over paths of gauge links in its vicinity. Mostly this vicinity is a $4d$ hypercube around the unsmeared gauge link. The underlying reason is to reduce short range fluctuations, since one mostly is interested in the long distance behavior of, e.g., correlation functions. By the replacement of links with their averages these short range fluctuations are smoothed out. As long as the smearing is local, i.e., the average contains only a fixed number of links, the long range behavior does not change in the continuum limit. To obtain a gauge covariant process, and thus no gauge fixing is needed, the link is replaced by averages of paths of links which have the same endpoints as the original link. Since in SU(3) this average is not in general again an element of the gauge group, some kind of a projection back into the group of SU(3) has to be performed.

Meanwhile a lot of link smearing procedures are available. We shortly want to discuss only three out of these.

APE smearing. Here, a weighted average of the original link and the six perpendicular staples, having the same endpoints as the link, is built [84]. The

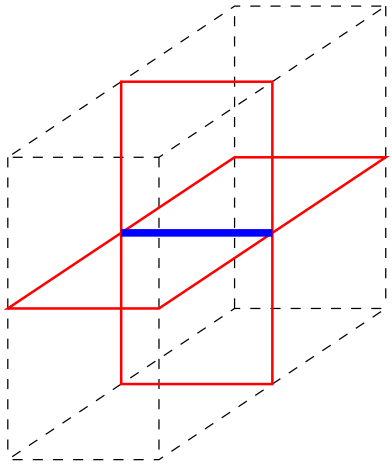

Figure 4.4: *A 3d plot of four staples (red) around some central link (blue).*

situation is depicted in three dimensions in Fig. 4.4: four out of the six staples (red), which have the same endpoints as the original link (blue), are plotted. The average is then computed as

$$V_\mu(n) = (1-\alpha)\, U_\mu(n) + \frac{\alpha}{6} \sum_{\nu \neq \mu} C_{\mu\nu}(n) \ , \tag{4.19}$$

where $C_{\mu\nu}(n)$ are the staples, i.e., an oriented product of three links, connecting the two endpoints of the link $U_\mu(n)$. The parameter $\alpha \in \mathbb{R}$ has to be adjusted depending on the gauge coupling β. The final projection back to SU(3) is normally done by maximization of $\mathrm{Re}\,\mathrm{tr}[X\, V_\mu^\dagger(n)]$ for $X \in \mathrm{SU}(3)$ and using X as the new link variable.

HYP smearing. This smearing procedure is some kind of an iterative APE smearing. Originally [39] three steps of projected APE smearing were used, containing only links which lie in the hypercube containing the original link. In general, one can take any smearing procedure as core of the HYP smearing; e.g., n-HYP [85] uses n-APE as core.

In our analyses the HYP smearing is used in the creation of quark field sources. Therefore, we use a $3d$ variant of this procedure, which only smears the links in spatial directions. It is applied three times on stout link smeared (see next item) gauge fields.

Stout link smearing. Since in HMC simulations one has to calculate derivatives of objects w.r.t. the gauge links, smearing procedures which use a projection

Sets	β	$m_0^\star$	$a^\star$ [fm]
A	4.70	-0.06987(32)	0.1311(15)
B	4.65	-0.07576(39)	0.1352(21)
C	4.58	-0.08377(19)	0.1380(17)

Table 4.2: *The values of $m_0^\star$ and $a^\star$ in fm (for $r_0 = 0.48$ fm) for each gauge coupling β.*

operator are not suitable for this purpose, since after the projection one cannot recover the original link. Thus, in 2003 the first differentiable (w.r.t. gauge links) smearing procedure was presented, the stout link smearing [86]. Also in our simulation stout link smearing is used and can be seen as one part of the definition of the Chirally Improved Dirac operator D_{CI}. This smearing does not use the projection described above, but uses instead

$$V_\mu(n) = e^{i\,Q_\mu(n)} U_\mu(n) \ , \tag{4.20}$$

where $Q_\mu(n)$ is a hermitian, traceless matrix which is built from staples. This procedure contains tunable, real weight factor $\rho_{\mu\nu}$, which often are kept constant, $\rho_{\mu\nu} = \rho$. In our case we set $\rho_{\mu\nu} = \rho = 0.165$.

4.6 A mass-independent scheme for the scale

The way we define the scale a in our lattice QCD simulation was already presented in Sec. 2.6. However, any dynamical simulation shows a dependence of r_0/a on the quark mass m. In [87] it is explained to what extent this is a physical effect. To milden this quark mass dependence, we use a so-called mass-independent scheme. In that approach one assigns the same lattice spacing to a fixed value of the gauge coupling β. This procedure is discussed now.

To work with this method, at least two simulations with different bare mass parameters m_0 at the same β are needed. One starts to determine the AWI-masses (see Sect. 7.2), which can be seen as the quark mass for this purpose, and plot them against the bare parameter m_0 (see Fig. 4.5 for our data). Then, a linear fit to the data of one particular β is made. From the fitted function one can read of the value for $m_0^\star = m_0(m_{\mathrm{AWI}} = 0)$. This value is often called the critical mass value. The next step is to plot the lattice spacing a against m_0 and also (linearly) fit the data groups of one β (cf. Fig. 4.6). At that point one is able to extract the value of a at $m_0 = m_0^\star$, which we denote as $a^\star$. The detailed numbers for $m_0^\star$ and $a^\star$ are given in

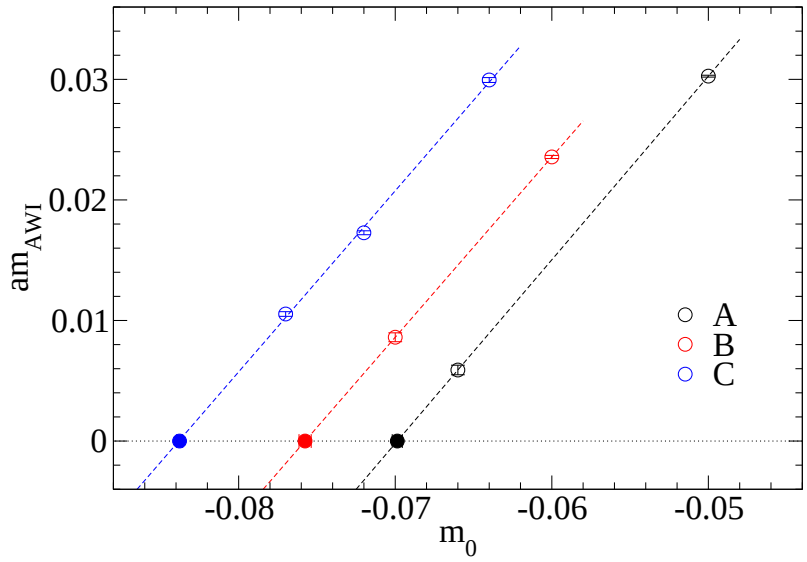

Figure 4.5: *We plot the AWI-mass m_{AWI} (in dimensionless units) against the bare mass parameter m_0 for each set of gauge configurations. The dashed lines are linear fits to the data points corresponding to one definite β, the dotted line indicates $am_{AWI} = 0$. The full symbols denote the critical values, $m_0^\star$, for each value of β.*

Tab. 4.2. The value of $a^\star$ is then attached to all sets of gauge configurations for the particular β. From now on we suppress the superscript "$\star$" and use the values given in Tab. 4.2 for our calculations.

4.7 Momentum projection and scattering states

Euclidean correlation functions were already discussed in Sec. 4.1 and from Eq. (4.1) we learned that a correlator is a (infinite) sum over states with energy levels E_k. The statement from above, that these energies equal the masses, has to be clarified: it is only valid for vanishing momentum, $\boldsymbol{p} = 0$. We now want to discuss this fact in more detail.

The energy E of a particle X and its mass m_X are related through the dispersion relation

$$E(X(\boldsymbol{p})) = \sqrt{m_X^2 + \boldsymbol{p}^2}\left(1 + \mathcal{O}(ap)\right) , \tag{4.21}$$

leading to $m_X = E(X(\boldsymbol{p} = 0))$. Thus, all states in our simulation are projected to momentum zero to obtain their rest mass.

In dynamical simulations a single hadron state can also couple to a state involving

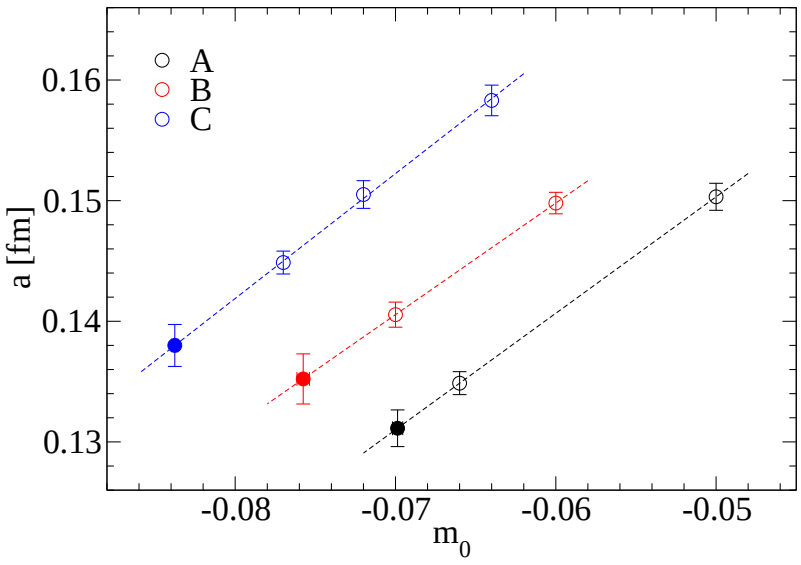

Figure 4.6: *We plot the lattice spacing a (in physical units) against the bare mass parameter m_0 for each set of gauge configurations. The dashed lines are linear fits to the data points corresponding to one definite β and the full symbols denote the values of a at $m_0 = m_0^\star$.*

two (or more) hadrons, a so-called scattering state. Even if the hadron is projected to $\boldsymbol{p} = 0$, the individual particles can have non vanishing momenta although the scattering state obeys $\boldsymbol{p} = 0$. The simplest example is a two particle state, in which one particle has a certain momentum $\boldsymbol{p}$ and the other exhibits a momentum $-\boldsymbol{p}$, which is in sum again zero. Since we use a finite box, the allowed values for $\boldsymbol{p}$ are discrete, in contrast to the continuum (which is nothing but a box with infinite volume). Each component p_i can have the values $ap_i = 2\pi k_i / L_s$, with $k_i = -L_s/2, \ldots, L_s/2 - 1$. The energy of such a two particle scattering state, neglecting interactions, is then given by

$$E(X(\boldsymbol{p}), Y(-\boldsymbol{p})) = \left(\sqrt{m_X^2 + \boldsymbol{p}^2} + \sqrt{m_Y^2 + \boldsymbol{p}^2} \right) \left(1 + \mathcal{O}(ap) \right) . \tag{4.22}$$

In some hadron channels the lowest scattering state energy lies above the signal we measure and this signal depends on the quark mass, which is a clear indication that the observed state is indeed the ground state. However, a clear and unique assignment of states with energies in the vicinity of scattering state energies is often not possible. Mostly, the two particle state energy is located between the measured ground state and the measured first excitation. Thus, we cannot identify the first excitation as a single hadron state, since it is also possible, that we see the two

particle state a bit above its experimental value. To distinguish bound states from scattering states one would have to run simulations with other (preferably bigger) volumes, since scattering states are suppressed by a factor of $\mathcal{O}(1/L_s^3)$ [88, 89]. Gauge field configurations for lattice size of $L_s = 24$, $L_t = 48$ are at the moment being produced for the parameters of the runs A66 and C77. We do not discuss results for these runs here, because the analysis is not finished yet.

Another possibility to give a statement about the nature of a measured state is to additionally analyze the eigenvector behavior. A hint for a one particle state is given by observing the same eigenvector composition for different points in the parameter space, i.e., for different dynamical sets of gauge configurations (cf. the discussion in [53]).

Chapter 5

Baryon spectroscopy and its results

5.1 Technical details

Let us start with some technicality to set the ground. For baryon spectroscopy we only use Gaussian sources, coming from Jacobi smearing of point-like quark fields – no derivative sources are included in the correlation matrices in the variational method, in contrast to meson spectroscopy from Chap. 6. The exact definitions of the baryon interpolators can be found in App. B.

For all channels we have data for positive and negative parity states. To be able to analyze both parities, we project the interpolators to a definite parity using the projection operator

$$P_{\pm} = \frac{\mathbb{1} \pm \gamma_t}{2} \ . \tag{5.1}$$

The interpolators for the Δ and Ω baryons have overlap with both spin $1/2$ and spin $3/2$ states [47], thus we have to project to spin $3/2$, using the projection operator for a Rarita-Schwinger field,

$$P^{(3/2)}_{\mu\nu}(\boldsymbol{p}) = \delta_{\mu\nu} - \frac{1}{3}\gamma_\mu\gamma_\nu - \frac{1}{3\boldsymbol{p}^2}\left(\boldsymbol{\gamma}\cdot\boldsymbol{p}\,\gamma_\mu\,p_\nu + p_\mu\,\gamma_\nu\,\boldsymbol{\gamma}\cdot\boldsymbol{p}\right) \ . \tag{5.2}$$

Since the correlation matrices C_{ij} are real and symmetric within numerical error bars, we symmetrize the matrices according to

$$\frac{C + C^\dagger}{2} \ \longrightarrow \ C \tag{5.3}$$

before diagonalization. This is also valid for the correlation matrices for mesons.

In the subsequent plots in this chapter and in Chap. 6 we always use the following legend for plots of masses to distinguish between the seven sets of gauge configurations:

Set	Symbol
A50	○
A66	○

Set	Symbol
B60	□
B70	□

Set	Symbol
C64	◇
C72	◇
C77	◇

Hence, a legend is only shown where otherwise the plot would be ambiguous. In general, we only include the dynamical (i.e., $m_{\text{valence}} = m_{\text{sea}}$) data points in our plots. In the case of the Ω, however, we also show data points where $m_{\text{valence}} > m_{\text{sea}}$ (partially quenched data points). Such data points are available for all sets, and they are used only to set the strange quark mass, see Sec. 5.4. Possible existing two particle scattering states are indicated by green crosses (✕) at the corresponding values of m_π^2. Experimental values are, if available in [9], displayed as magenta stars (✳), corresponding error bars are only displayed if they are bigger than 40 MeV. In each plot we print the name of the baryon and its quantum numbers J^P in the lower left corner. Fits of the dynamical points are shown as black lines, the corresponding errors are the surrounding dashed black lines. The range for the fitted value at $m_\pi = m_\pi^{(\text{phys})}$ is also displayed as vertical black line. The detailed form of these fits is discussed in more detail now.

All the simulations we perform are at values of the pion mass, which are bigger than the physical value. Thus, we have to perform some kind of extrapolation of our data to the physical (experimental) point. In our case we find chiral perturbation theory [90, 91, 92] to be the appropriate tool. There, the only varying parameter is the quark mass. However, this method is based on constant values for other parameters, like the lattice spacing or the volume. Of course, the explicit analytic form of the extrapolation depends also on the path one takes in parameter space. Strictly speaking, we then would only be allowed to fit the data of sets A, B and C separately. Since all our values for the lattice spacing and the gauge coupling are very similar, we assume our extrapolation path to be very close to the one with constant parameters. Thus, for the mass m_X of a particle X we use a form, which is linear in the quark mass in leading order, i.e., linear in the pion mass squared (cf. Sec. 7.2). In dimensionless units (am_X) we find

$$am_X = c_0 + c_1 \, (am_\pi)^2 + \mathcal{O}\Big((am_\pi)^2 \ln am_\pi\Big) \; . \tag{5.4}$$

Therefrom, we can read of the value for m_X either for the physical pion mass or in the chiral limit (i.e., $m_\pi = 0$). In Chap. 9 we will summarize our spectroscopy results and use these extracted values there.

5.2 The Nucleon

Positive parity

We want to start our discussion of the baryon spectroscopy results with that channel, where one normally gets the best signal: the positive parity nucleon N. To

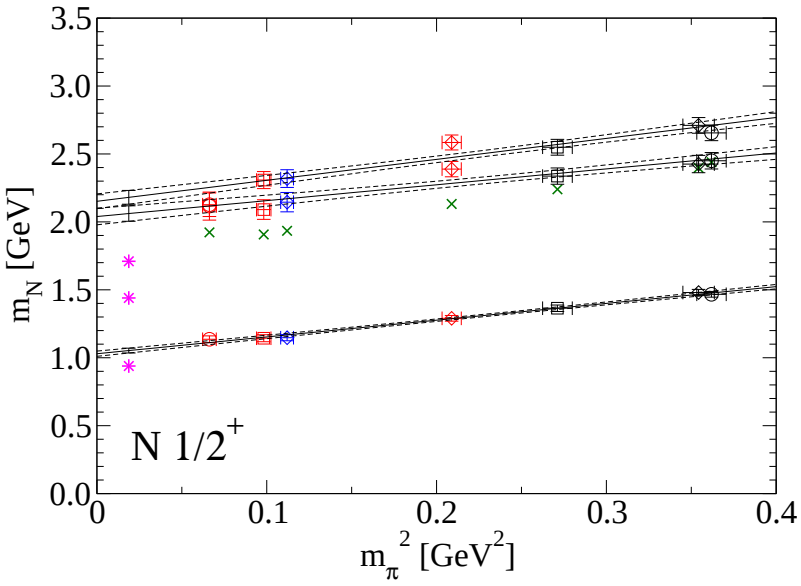

Figure 5.1: *The mass of the positive parity nucleon is plotted against m_π^2 in physical units. The energy levels of the (theoretical) P wave scattering state $N\pi$ are shown as crosses.*

extract the ground state (GS) and two excitations (1E, 2E), we used the interpolator combination $1, 2, 4, 6, 14, 17, 18$ (see App. B for details). In Fig. 5.1 we show the extracted masses in physical units. Our result for the ground state lies about 10% above the experimental value. In [93, 94] it was found that also a fit linear in the pion mass agrees well with the experimental data. We here, however, want to stick to the form given in Eq. (5.4), since this form is suggested by chiral perturbation theory.

Since its discovery in 1964 [95] the first excitation of the positive parity nucleon, the so-called Roper resonance, is a quite special candidate in baryon spectroscopy. Its mass lies below the mass of the first excitation of the negative parity nucleon channel. This is often called reverse level ordering. In most of the dynamical simulations (see, e.g., [96, 77, 53, 97, 98]) such a reverse level ordering is not seen and the energy level for that resonance comes out to high; we obtain a value of about 600 MeV above the experimental value. There may be a few reasons for that observation. First of all, this excitation is not an orbital (as in the negative parity) but a radial excitation in the language of the quark model. Thus, its size could be considerably larger than that of the ground state and may be squeezed due to the limited spatial lattice volume. To eliminate this effect, bigger and finer lattice would

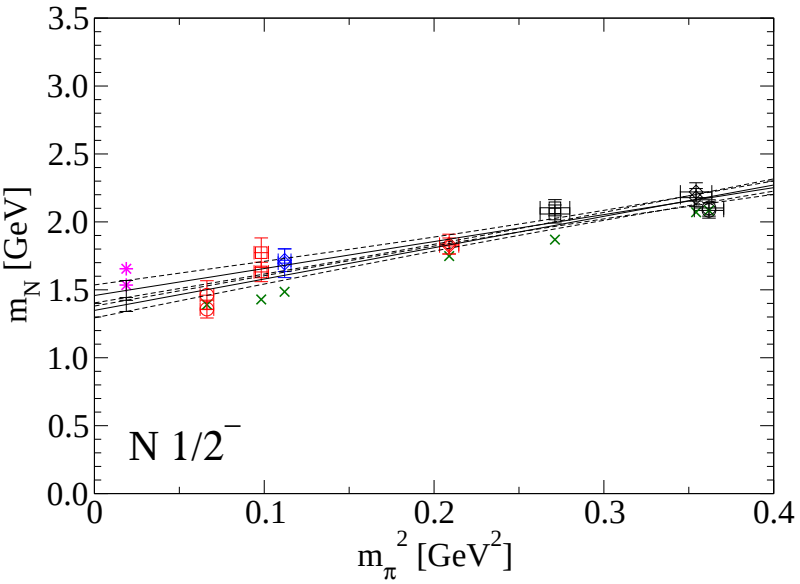

Figure 5.2: *The mass of the negative parity nucleon is plotted against m_π^2 in physical units. The energy levels of the (theoretical) S wave scattering state $N\pi$ are shown as crosses.*

be helpful. We further have rather noisy data in that channel and it could just be a statistical effect and more configurations would be needed to clarify this aspect. A third reason could emerge from a possible existing P wave $N\pi$ channel, which is not represented by our set of interpolators. Thus, the inclusion of nucleon-meson interpolators could improve our insight here and, of course, also for all other baryon channels. Although there is no clear separation of the energy levels of the scattering states and our signals, we favor the one particle picture since the eigenvector composition is the same for all seven sets (see the discussion in Sec. 4.7).

However, some groups [99, 100, 101] were able to extract a state, which approaches the right physical value. In that analyses several fermion actions and fitting techniques are used, but all groups work with quenched gauge field configurations. To confirm these results with our approach (dynamical configurations!) would be worthwhile, but for sure, all points mentioned above are needed for a systematic analysis.

Negative parity

We now want to discuss the negative parity nucleon channel. Although the time range for a fit of the eigenvalues is limited due to the backward (in Euclidean time)

running positive parity nucleon and due to possible present scattering states [102], we can extract the two lowest lying states, but from a quite noisy signal. We use the interpolator combination $1, 2, 3, 7, 8, 9$. The masses can be found in Fig. 5.2. One can see, that we underestimate the experimental values slightly, as for all negative parity baryon channels.

In this case we cannot clearly distinguish if a one or a two particle state is seen. It is possible that an S wave $N\pi$ state, which is not represented by our set of interpolators, is present here. Taking into account the extracted masses only, we even would conclude that the state obtained is a scattering state. In Nature the S wave state lies below the ground state of the negative parity nucleon. This still may be true for the small pion masses as we obtain in set A66, and thus we may see a two particle state there (this data point increases the slope of the fit drastically!). However, for the sets with larger pion masses, this should not be the case.

Additionally we then can analyze the composition of the states via the eigenvectors from the variational method and see if we always obtain the same eigenvector composition over the whole range of pion (i.e., quark) masses; this is done in Fig. 5.3. There we plot the eigenvector components of the ground state and the first excitation for all sets. We always observe the same composition of states from the heaviest (A50) down to the lowest (A66) pion mass, but this can now be interpreted in two contrary ways. Since the composition does not change, this behavior can favor either the bound state or the scattering state: In both cases the corresponding state would simply be observed in all sets.

Thus, we cannot give a definite statement about the particle content in this channel. As in the positive parity channel, further investigation by, e.g., larger lattices or a momentum analysis can help to clarify this issue.

5.3 The Delta

Positive parity

In the case of the Δ we have to project to spin $3/2$ and end up with a total of 8 interpolators. Since 2 of these 8 are numerically very similar to others, we omit them in our correlation matrices and are finally able to analyze 6 different interpolators. They differ only in their smearing type for the individual quarks.

It turns out, that the differences in the results of all possible subsets of the full 6×6 correlation matrix are only small. We use the combination $1, 3, 4$ and can extract the first two energy levels (see Fig. 5.4). In both cases we favor the picture of a one particle state, since our values are clearly off from the P wave $N\pi$ state; this

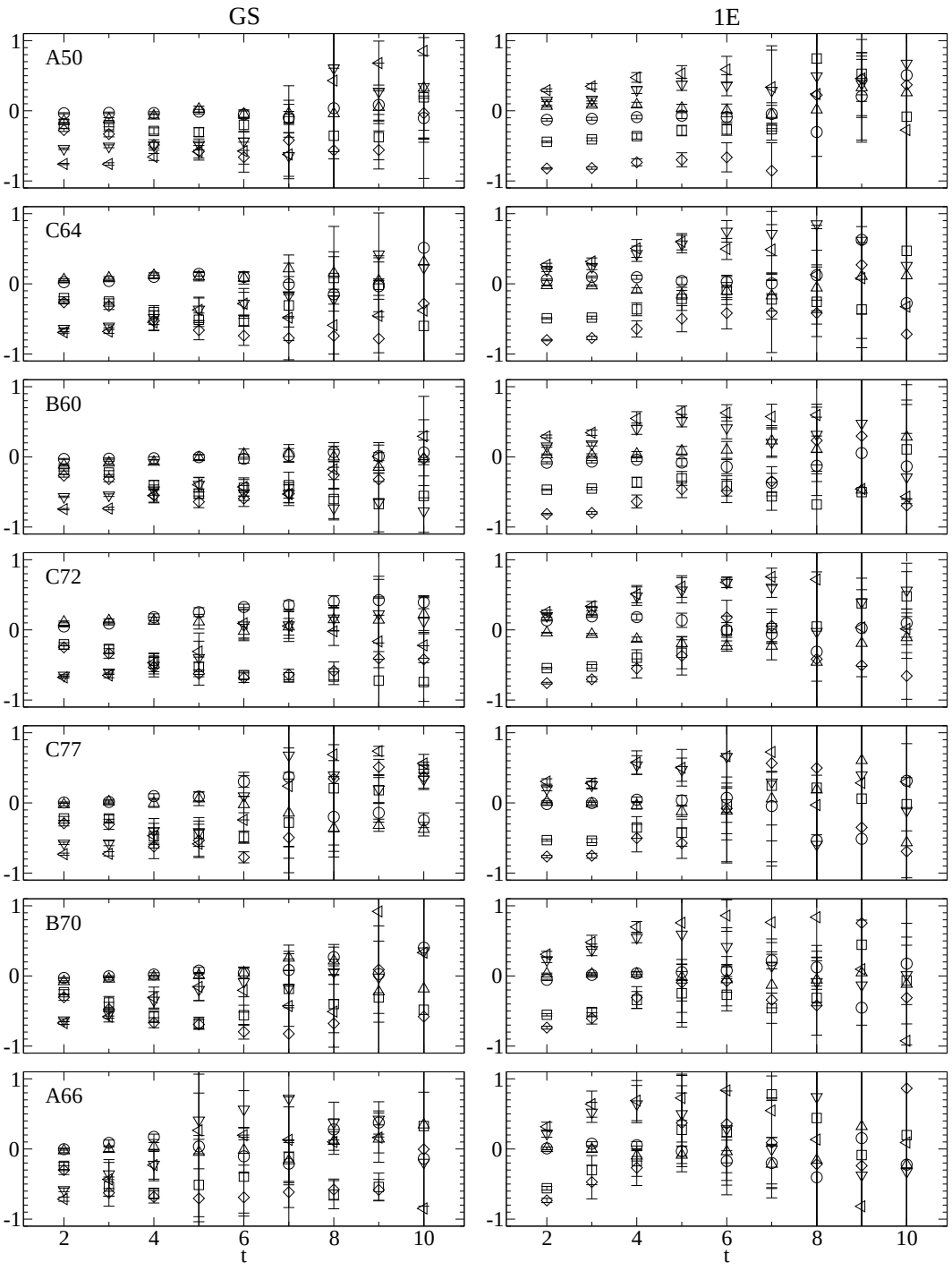

Figure 5.3: *Time dependency of the eigenvector components of the ground state (left panel) and the first excited state (right panel) of the negative parity nucleon. From top to bottom the pion mass is getting continuously smaller.*

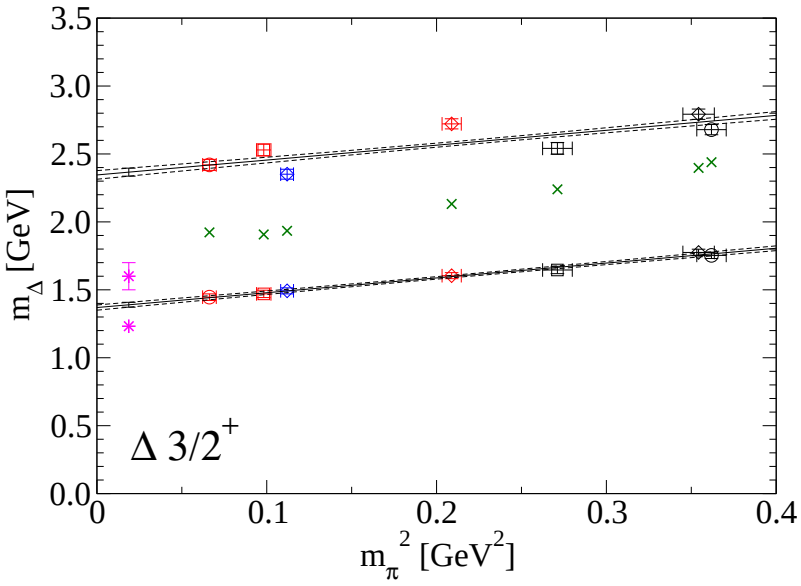

Figure 5.4: *The mass of the positive parity Δ is plotted against m_π^2 in physical units. The energy levels of the (theoretical) P wave scattering state $N\pi$ are shown as crosses.*

state seems to be missing here. Our final result for the ground state (at the physical point) overestimates the experimental value by roughly the same amount as for the nucleon, namely 10%. For the Roper-like state $\Delta(1600)$ our signal is, again as for the nucleon, rather beyond the experimental value. Due to the small statistical errors in both cases, we presume either finite volume effects or other systematic errors to be the reason(s) for this discrepancy.

This hadron channel is also used to set the mass of the strange quark, m_s. Therefore, we have to use partially quenched mass values, i.e., $m_{\text{valence}} > m_{\text{sea}}$. Details of that procedure follow in the next section.

Negative parity

For the negative parity Δ we can extract a signal using interpolators $2, 3, 5$ (see Fig. 5.5). The statistical error bars are fairly small, however, the experimental value is slightly underestimated.

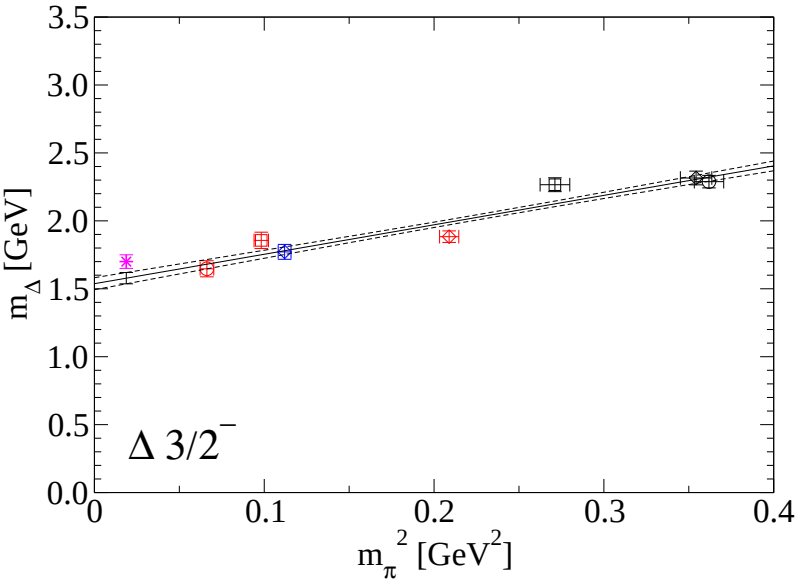

Figure 5.5: *The mass of the negative parity Δ is plotted against m_π^2 in physical units.*

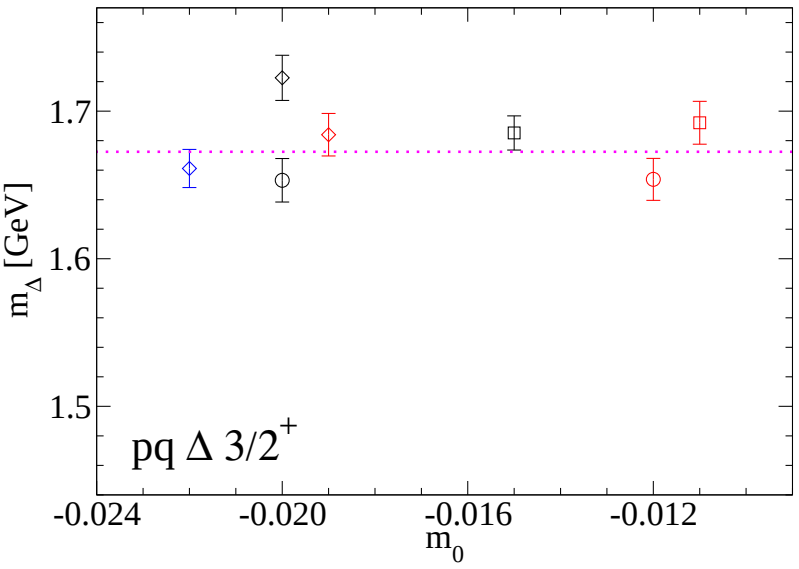

Figure 5.6: *We plot the masses (in the mass dependent scheme) of the positive parity Δ resp. Ω, extracted from partially quenched data (i.e., $m_{\text{valence}} > m_{\text{sea}}$) against m_0. The dotted magenta line indicates the value of the physical $\Omega(1672)$.*

5.4 Setting the strange quark mass with the Omega

The sets of gauge configurations were created including two dynamical light quark flavors. To be able to study also hadrons with strange quark content, we have to introduce somehow a strange quark into our simulation. How this can be done is explained in more detail now.

Since the positive parity Δ and the $\Omega(1672)$ share the same J^P quantum numbers and consist of only one quark type, we can identify a Δ state where $m_{\text{valence}} > m_{\text{sea}}$ with the $\Omega(1672)$. Thus, we get the bare mass parameter at which the quark mass equals approximately m_s. We then can use the quark propagators for this valence quark mass to compute hadron correlators including strange quarks. However, we do not include the effects coming from a dynamical strange quark. All our hadrons built from light and strange quarks always include dynamical ($m_{\text{valence}} = m_{\text{sea}}$) light quarks and quenched strange quarks, motivated by partially quenched ($m_{\text{valence}} > m_{\text{sea}}$) data.

To fix the value where $m_{\text{valence}} = m_s$, we followed a strategy, where we can determine the value for m_Ω exactly only a posteriori. We started analyzing the Δ of the first 50 independent configurations and determined from that the value of m_{bare}, at which we get a signal closest to $m_\Omega^{(\text{phys})}$. Initially, the available values for m_{bare} had a discrete difference of 0.05, thus for some sets we had to recompute quark propagators at different m_{bare}, if the signal was too far off from $m_\Omega^{(\text{phys})}$. In Fig. 5.6 we plot the masses of the partially quenched Δ, at which we fixed m_s, against m_0. This plot, of course, is for full statistics; we used interpolators $1, 3, 4$. One can see that we get values for m_Ω which mostly are not more than two standard deviations away from the physical value. Only the results from set C64 deviate more. A reason may be the choice of interpolators here. When fixing the value of m_{bare} we did not use the same combination of interpolators for each set – but we do here! Hence, the combination $1, 3, 4$ may not be the best, but to have comparable results, we stick to this choice. Let us stress one important point here. This analysis was done in the mass dependent scheme (cf. Sec. 4.6), since we did not create the sets of gauge configurations in parallel. Thus, we were not able to fix the value of the lattice spacing for the corresponding coupling β in advance, and therefore we also can extract the Ω mass in the mass independent scheme – and do not only get the values from Fig. 5.6 again.

To some extent we can cross check our designated results for m_s by analyzing other hadrons, which include strange quarks. In the baryon sector we get results (see next sections) for Σ (built from two light and one strange quark) and Ξ (built from one light and two strange quarks), which extrapolate very nicely to the physical

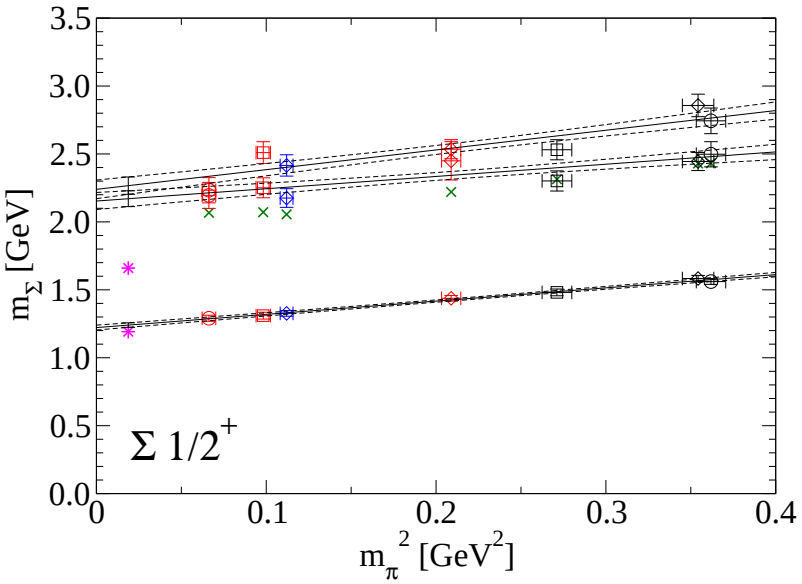

Figure 5.7: *The mass of the positive parity Σ is plotted against m_π^2 in physical units. The energy levels of the (theoretical) P wave scattering state NK are shown as crosses.*

value. This confirms our choice of values. In the meson sector we can analyze the K mesons (see Sects. 6.4 and 6.5) or the ϕ meson (see Sec. 6.6) to get another validation to that topic.

5.5 The Sigma

Positive parity

The Σ baryon consists of two light and one strange quark. Its Dirac structure is the same as for the nucleon, only the flavor content differs. Thus we can use the same interpolator basis for the variational method as before, extended by some interpolators due to the different quark masses. Using interpolators $1, 2, 6, 17, 20$ we can extract the ground state and two excitations (see Fig. 5.7). The ground state is in good agreement with the experimental data and confirms again our choice for m_s. The first excitation comes out about one third to high compared to the experimental level, which can be due to finite volume effects. For the second excited state we do not have an experimental value, confirmed by the Particle Data Group (PDG), to which we can compare to. The next state with the same quantum numbers,

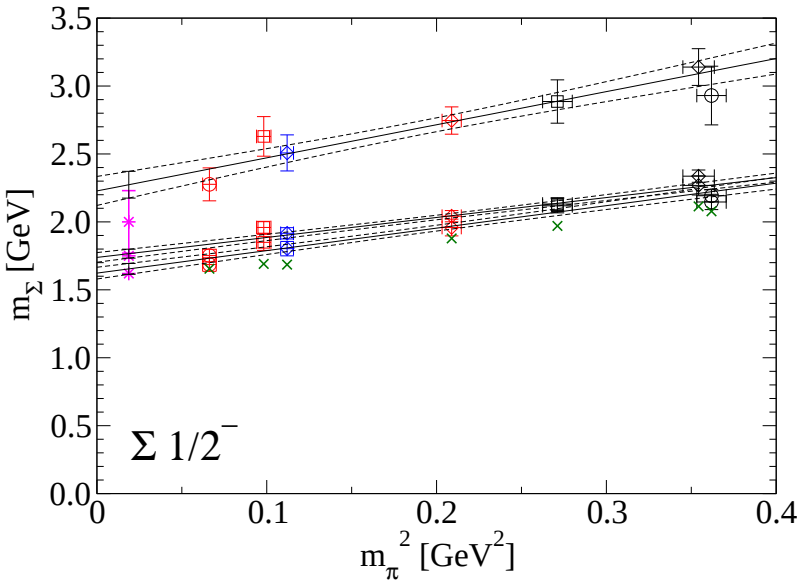

Figure 5.8: *The mass of the negative parity Σ is plotted against m_π^2 in physical units. The energy levels of the (theoretical) S wave scattering state NK are shown as crosses.*

$\Sigma(1770)$, is classified with only one star by the PDG, which is expressed as 'evidence of existence is poor'. For the reasons already mentioned above and due to the same eigenvector composition for each set of gauge configurations, we are not able to decide whether we see a one particle state or a scattering state here.

Negative parity

In the negative parity Σ channel we can extract the ground state and two excitations, see Fig. 5.8. We used interpolators $1, 9, 10, 12$. As for the nucleon, the ground state and the first excitation lie very close to each other. In our case, the extrapolation to the physical point for both states agrees surprisingly well with the experimentally measured states $\Sigma(1620)$ and $\Sigma(1750)$ (rated with 2 and 3 stars by the PDG, respectively). The second excitation here reaches a value of about 2270 MeV, which may be compatible with the $\Sigma(2000)$, however, this state is not yet confirmed by the PDG and has a rating of one star.

The lowest scattering state, the S wave NK, lies below the one particle state at the physical point. To find out if we see a one particle state, instead of a scattering state, we traced the eigenvalues from high to low pion masses and did not find any change in their relative weights to that state (cf. the discussion for the negative

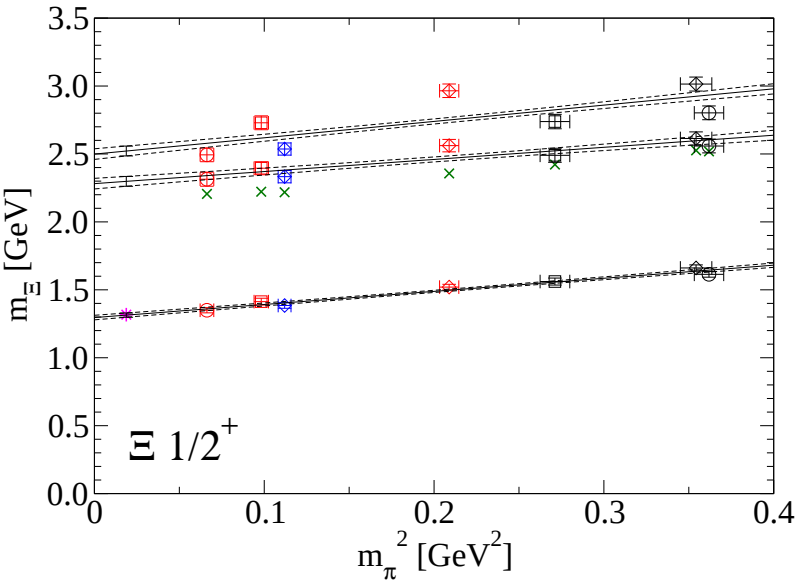

Figure 5.9: *The mass of the positive parity Ξ is plotted against m_π^2 in physical units. The energy levels of the (theoretical) P wave scattering state ΣK are shown as crosses.*

parity nucleon). Here, the masses would favor the two particle picture. As for the positive parity Σ, we cannot reliably determine the particle content.

5.6 The Xi

Positive parity

For this channel we only have one state, confirmed by the PDG, we can compare to. From our data we can, however, extract three states with rather small statistical errors. We used interpolators $1, 2, 3, 4, 9, 10, 13, 17$, the masses are shown in Fig. 5.9. The ground state fits perfectly with the experimental data point, which again backs up the choice for the strange quark mass parameter. The excitations we get are in the range of about 2300 and 2500 MeV. States in such energy regions, listed by the PDG, are assigned neither spin J nor parity P.

Negative parity

As for the positive parity we here can measure the ground state and two excitations, using interpolators $1, 2, 9, 10, 14, 17, 21$. The extracted masses are plotted in Fig.

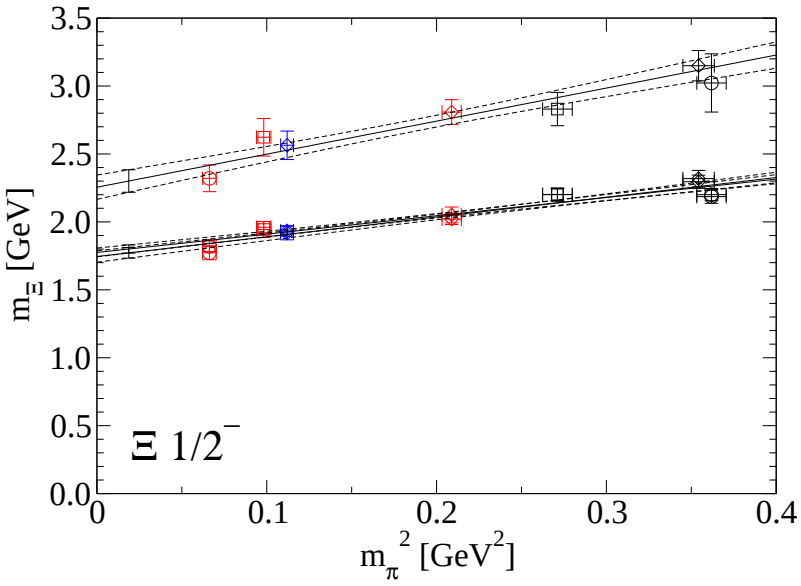

Figure 5.10: *The mass of the negative parity* Ξ *is plotted against* m_π^2 *in physical units.*

5.10. The experimental situation here is even worse than for the positive parity channel, there is no state listed by the PDG. The ground state and the first excitation are very close to each other and are located in a region of 1730 to 1830 MeV, both having small statistical errors. The second excitation lies around 2300 MeV and the signal is fluctuating a bit more. As before, unconfirmed states with undefined spin and parity are seen in such energy regions.

5.7 The Omega

Positive parity

In Sec. 5.4 we used the positive parity Ω to fix the mass parameter of the strange quark. If we turn over to the mass independent scheme, as for all other channels, and start the analysis, we get "biased" results here, since we measure a quantity which was used already before as input, although in a different way. However, the extrapolation of the ground state mass to the physical point gives perfect agreement with the experimental data, see Fig. 5.11. We used interpolators $1, 3, 4$ as in the Δ channel. The situation is definitely different for the first excitation. We get a signal at about 2500 MeV, which is compatible to the $\Omega(2470)$, a state, which is listed by

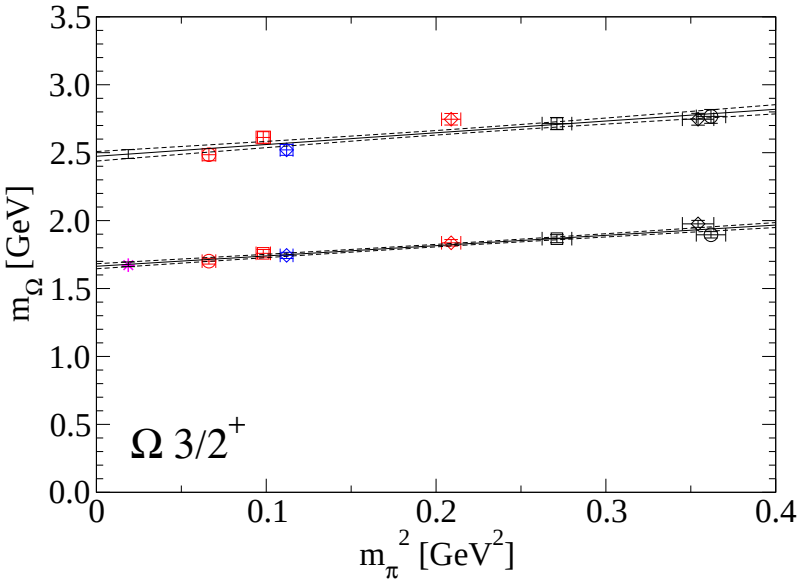

Figure 5.11: *The mass of the positive parity Ω is plotted against m_π^2 in physical units.*

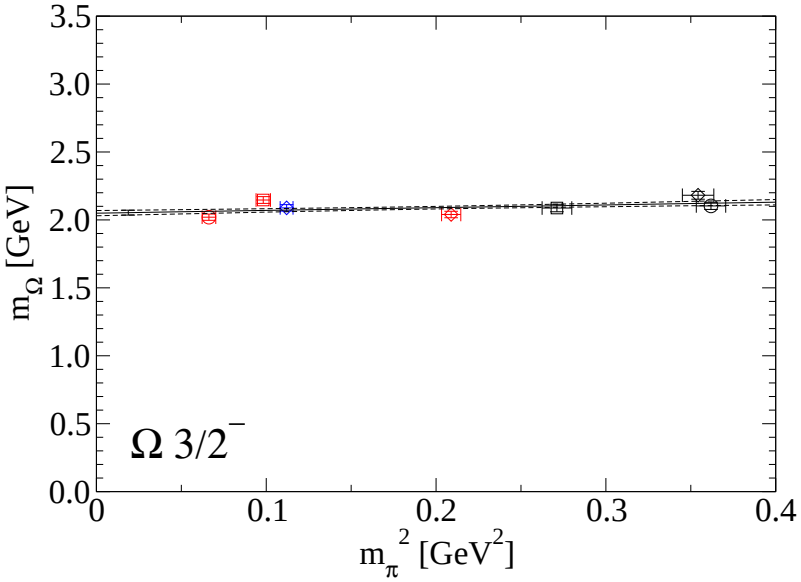

Figure 5.12: *The mass of the negative parity Ω is plotted against m_π^2 in physical units.*

the PDG without spin and parity and not yet confirmed.

Negative parity

In the negative parity Ω channel we get a signal around 2050 MeV. In Fig. 5.12 we show the extracted masses, utilizing interpolators $2, 3, 5$ from the Δ channel. Here, we cannot compare to any state listed by the PDG.

Chapter 6

The mass spectrum for mesons

6.1 Preparatory background

In the analysis of the meson sector we use three types of quark sources, a narrow, a wide and a derivative source, to include in the basis for the variational method. For both types of mesons, those built from only light quarks and those including also strange quarks, the interpolators are given in App. B. Since the C parity is only an exact symmetry for mesons built from mass degenerate quarks, the right columns of the tables with interpolators in App. B apply only to light mesons. However, this quantum number may be still an approximate quantum number for mesons with light and strange quarks (i.e., non mass degenerate quarks) and is possibly still valid to some significant amount. Hence, we can try to include in the variational basis only interpolators sharing the same C (in the limit of mass degenerate quarks), and find out if some state is dominated by a definite C parity. This point will be discussed again later in Sec. 6.5.

To improve statistics on the one hand, and to respect the correct symmetries on the other, we folded the data in time around the symmetry point $t = L_T/2$ and performed the same symmetrization as for the baryons,

$$\frac{C + C^\dagger}{2} \longrightarrow C \ . \tag{6.1}$$

All the details about the legends in the subsequent plots and the chiral fit procedure are the same as for baryons and were already fixed in Sec. 5.1. In each plot we print the name of the meson and its quantum numbers as J^{PC} (or J^P for strange mesons) in the upper left corner. The data points for plots of strange mesons are extracted from the points where the light quark has its dynamical value and the strange quark its given value (details can be found in Sec. 5.4).

Unfortunately we are not able to follow the same strategy for the choice of interpolators as we do for the baryons – there it was possible to use the same interpolators combination and the same time range to extract the mass from. Here, however, we sometimes have to use different combinations for different states, or even different combinations for each of the sets. The time ranges mostly were adapted

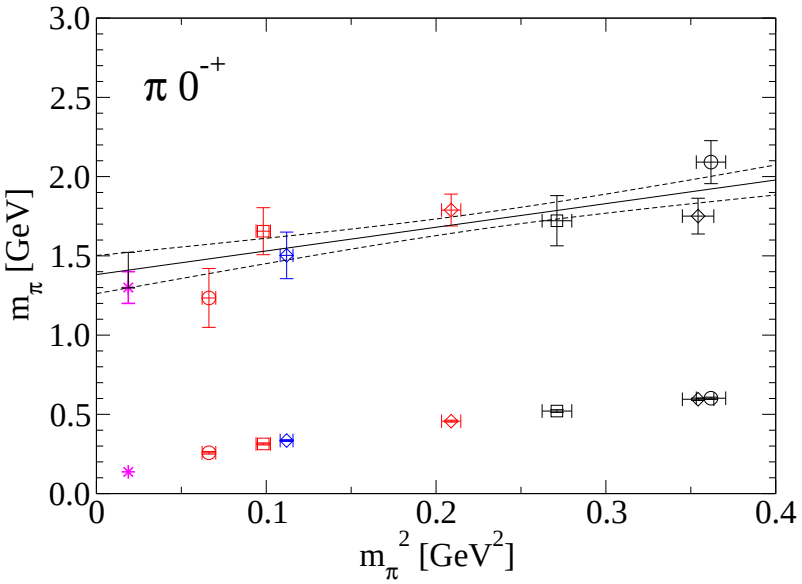

Figure 6.1: *The mass of the pseudoscalar meson π ($J^{PC} = 0^{-+}$) is plotted against m_π^2 in physical units.*

individually for each set. This proceeding is necessary to obtain reasonable results, or, in some cases, to obtain a result at all. A summary of the results from the chiral fit can be found in Chap. 9.

6.2 Light quark mesons with spin 0

6.2.1 The pseudoscalar meson π, $J^{PC}=0^{-+}$

We start our discussion of light meson spectroscopy results with the pion; its quantum numbers are $J^{PC} = 0^{-+}$. Since the ground state mass of this particle is used to set the scale in all our plots of hadron masses, we here decide to fix it by inclusion of only one interpolator, as such a choice gives the longest plateau in the effective mass. The first excitation could also be extracted. The interpolators used are

State	A50	A66	B60	B70	C64	C72	C77
GS 0^{-+}	1	1	1	2	1	2	1
1E 0^{-+}	1,2,17 throughout						

The detailed values are shown in Fig. 6.1. Although it is nothing but a square root function, we also show the ground state masses there to give the magnitude of the statistical errors.

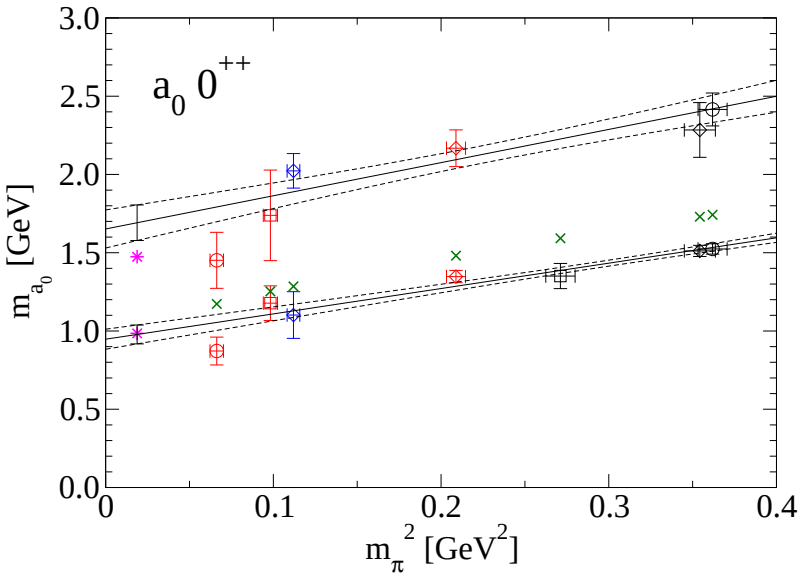

Figure 6.2: *The mass of the scalar isovector meson a_0 ($J^{PC} = 0^{++}$) is plotted against m_π^2 in physical units. The energy levels of the (theoretical) S wave scattering state $\eta_2\pi$ are shown as crosses [104].*

We already discussed the quality of the signal of the first excitation in [40]. This signal is contaminated by a backward running pion and thus the plateau in the effective mass is shortened, especially for small pion masses. Nevertheless, we could get a signal with fair statistical error bars. The chiral extrapolation of this signal is compatible with the experimental value.

6.2.2 The scalar isovector meson a_0, $J^{PC}=0^{++}$

In lattice simulations the scalar meson a_0 ($J^{PC} = 0^{++}$) is a rather delicate business (see, e.g., [103] for a nice overview). There are still ongoing discussions about the quark content of this meson, i.e., whether it is a quark-antiquark or a tetra-quark state. The other great difficulty is, that in the bunch of states (obeying $J^{PC} = 0^{++}$) to which the interpolators couple, scattering states with a mass lower than the ground state mass of the a_0 are present (at the physical point!). Thus, the part of the correlator one is interested in appears only as sub-leading term.

In our case we can extract the ground state and the first excitation (see Fig. 6.2) using the interpolators

State	A50	A66	B60	B70	C64	C72	C77
GS 0^{++}	13 throughout						
1E 0^{++}	10,12,13	4,10,12,13	—	1,4,10,12	1,4,10,12	10,12,13	10,12,13

The signals for the ground state of the different sets seem to be consistent, except for set A66. Maybe there we are already in a region of the pion mass, where we do not see a bound state as the lowest lying state, but we cannot surely identify the state; further investigation is crucial here. However, our signals all lie below the S wave $\eta_2\pi$ scattering state. We used the value given in [104] for the mass of the η_2 meson and assumed that this particle has the same dependence on m_π^2 as the vector meson ρ. For the first excitation we get quite noisy signals, in set B60 we could not even get any signal. However, the chiral extrapolations for the two states are either in astonishing agreement with the PDG data (ground state) or match with the experimental point within two standard deviations. However, in this channel it is impossible to identify the state as a bound state.

6.3 Light quark mesons with spin 1

6.3.1 The vector meson ρ, $J^{PC}=1^{--}$

For the vector meson channel ρ, $J^{PC} = 1^{--}$, we get a ground state signal, which in the chiral limit perfectly agrees with experimental data. The signal of the first excitation is also in good agreement with data from the PDG (see Fig. 6.3). We used interpolators $1, 5, 8$ for the ground state and $1, 8, 12, 17, 22$ for the first excitation.

Since the vector meson is not a stable particle, i.e., it decays into a P wave $\pi\pi$ state, we also show the scattering state in Fig. 6.3. Since this state lies above our ground state signal, we conclude, that here the ground state is indeed dominated by the ρ meson and is not a scattering state (such a state is usually called "stabilized"). The signal for the first excitation in our case always lies above the scattering state. The reason that we do not observe a scattering state may be the same as for the baryons: our set of interpolators lacks two meson states.

6.3.2 The axial vector meson b_1, $J^{PC}=1^{+-}$

In the axial vector meson channel b_1 ($J^{PC} = 1^{+-}$) we only could fit the ground state and did not get any signal for an excitation. Using interpolator 6 throughout all sets, we get the masses plotted in Fig. 6.4. In this figure also the dominant decay channel for the b_1, the S wave state $\omega\pi$, is shown. The mass of the ω is estimated by $m_\omega \approx m_\rho$. Since except for set C72 (which may be an incidentally statistical

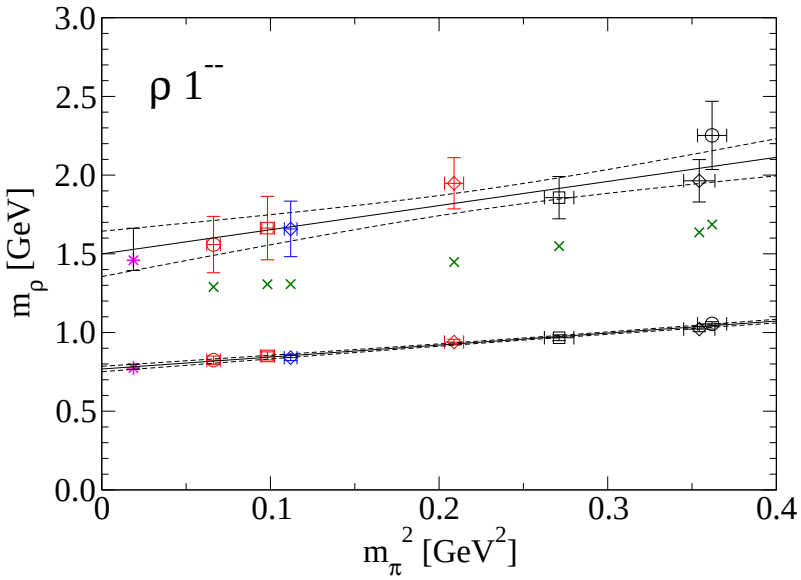

Figure 6.3: *The mass of the vector meson ρ ($J^{PC} = 1^{--}$) is plotted against m_π^2 in physical units. The energy levels of the (theoretical) P wave scattering state $\pi\pi$ are shown as crosses.*

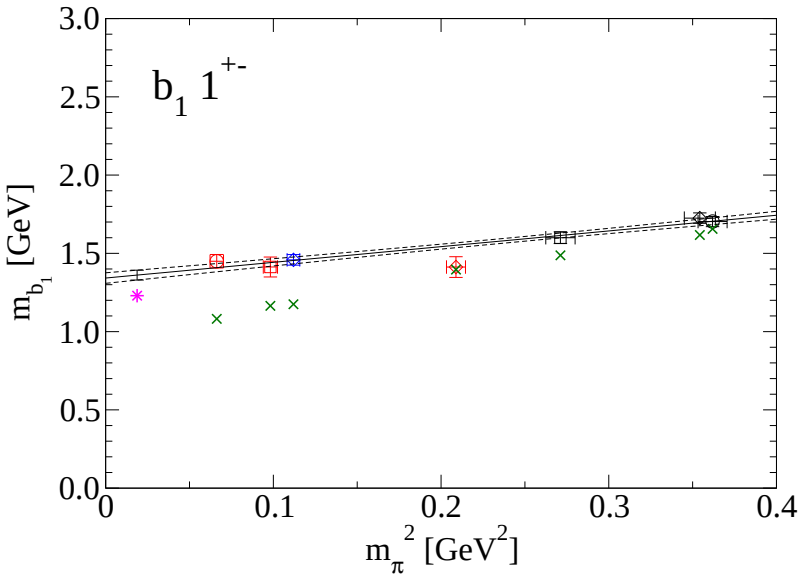

Figure 6.4: *The mass of the axial vector meson b_1 ($J^{PC} = 1^{+-}$) is plotted against m_π^2 in physical units. The energy levels of the (theoretical) S wave scattering state $\omega\pi$ are shown as crosses.*

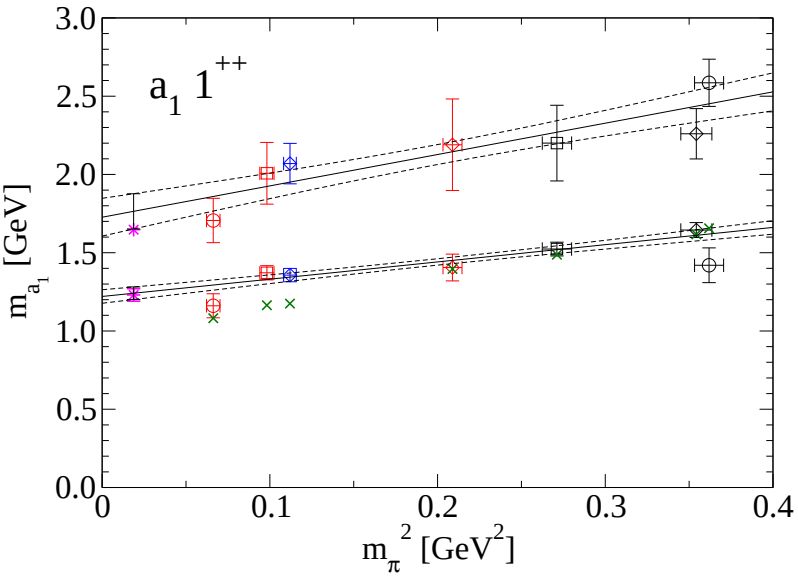

Figure 6.5: *The mass of the axial vector meson a_1 ($J^{PC} = 1^{++}$) is plotted against m_π^2 in physical units. The energy levels of the (theoretical) S wave scattering state $\rho\pi$ are shown as crosses.*

effect) the mass of the scattering state lies below our measured results, we conclude that the observed state is the b_1 ground state. Another reason is, of course, that we do not use two particle interpolators and thus the coupling to such a state is quite weak. The final result for the chiral extrapolation slightly overestimates the experimental data point.

6.3.3 The axial vector meson a_1, $J^{PC}=1^{++}$

In the axial vector meson a_1 channel with the quantum numbers $J^{PC} = 1^{++}$ we could extract the ground state and the first excitation using the interpolators

State	A50	A66	B60	B70	C64	C72	C77
GS 1^{++}	1 throughout						
1E 1^{++}	1,4,13	4,13,15	1,2,13	1,2,13	1,2,13	1,2,4,	1,2,4

The ground state comes out with small statistical error bars (see Fig. 6.5). Comparing these results with the S wave scattering state $\rho\pi$, we cannot draw a reliable conclusion of the particle content in this channel. Some of our measured results lie straight on top of the corresponding $\rho\pi$ energy level, while others are clearly separated. Here, increasing statistics would be a great benefit to determine the

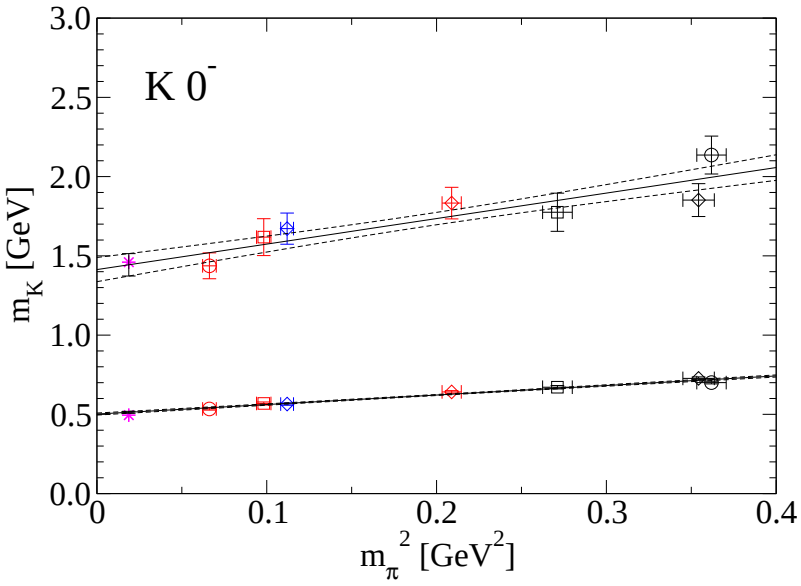

Figure 6.6: *The mass of the K meson ($J^P = 0^-$) is plotted against m_π^2 in physical units.*

state more precisely. Nevertheless, our chiral extrapolation of this state is in perfect agreement with the PDG data.

The first excited state here only gives results with rather big statistical error bars, but we finally get a result which still overlaps with experiment. However, in both states the results are strongly depending on the chosen time range for the fit of the eigenvalues. Hence, we are not able to draw definite conclusions about the qualitative and quantitative results here.

6.4 Strange quark mesons with spin 0

6.4.1 The K, $J^P=0^-$

In the strange meson channel with $J^P = 0^-$, the K meson, we find for both, the ground state (using interpolator 1) and the first excitation (using interpolators $1, 2, 8, 17$), a very sharp signal with small statistical error bars, which extrapolates very nicely to the experimental point (see Fig. 6.6). This result confirms once more our choice for the strange quark mass parameter m_s.

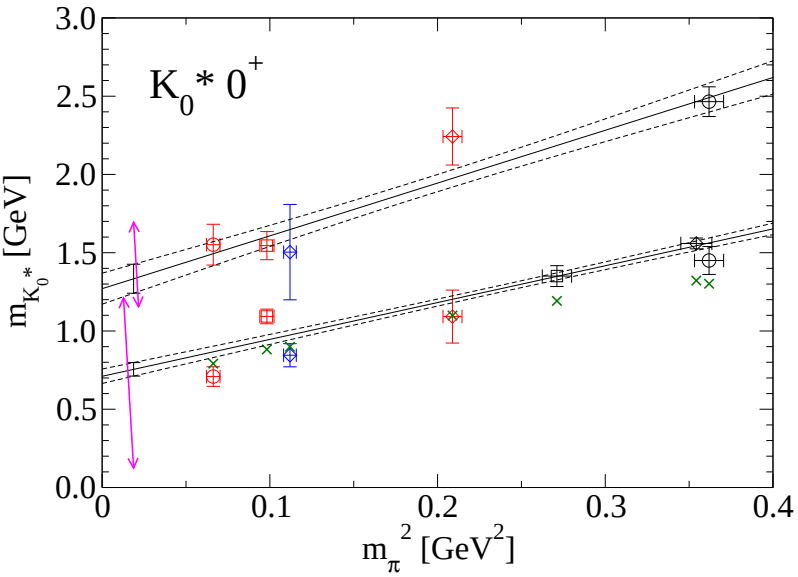

Figure 6.7: *The mass of the K_0^* meson ($J^P = 0^+$) is plotted against m_π^2 in physical units. The energy levels of the (theoretical) S wave scattering state $K\pi$ are shown as crosses. The resonance widths are depicted as magenta lines with end-arrows, which are slightly shifted to clearly show their overlap.*

6.4.2 The K_0^*, J^P=0^+

Here, the situation is similar to the light $J^{PC} = 0^{++}$ a_0 channel. The lowest state listed by the PDG, obeying the quantum numbers of the K_0^* meson, $J^P = 0^+$, is a very broad resonance with a width of about 550 MeV at a mass of about 672 MeV: the $K_0^*(800)$ or κ. This state is not yet confirmed by the PDG. The least controversial (and confirmed) state is the $K_0^*(1430)$, having a width of about 270 MeV. These two resonances overlap in their widths as one can see in Fig. 6.7. In this figure we also show our results for the ground state energy level and the first excitation, for which the following interpolators are used

State	A50	A66	B60	B70	C64	C72	C77
GS 0^+	13 throughout						
1E 0^+	10,12,13	4,10,12,13	—	4,10,12,13	—	10,12,13	4,10,12,13

For the sets B60 and C64 we are not able to extract a reliable signal for the first excited state.

Although our ground state result in the chiral extrapolation has small errors and hits the experimental point, we cannot exclude that we see the scattering S wave state $K\pi$ (crosses in Fig. 6.7).

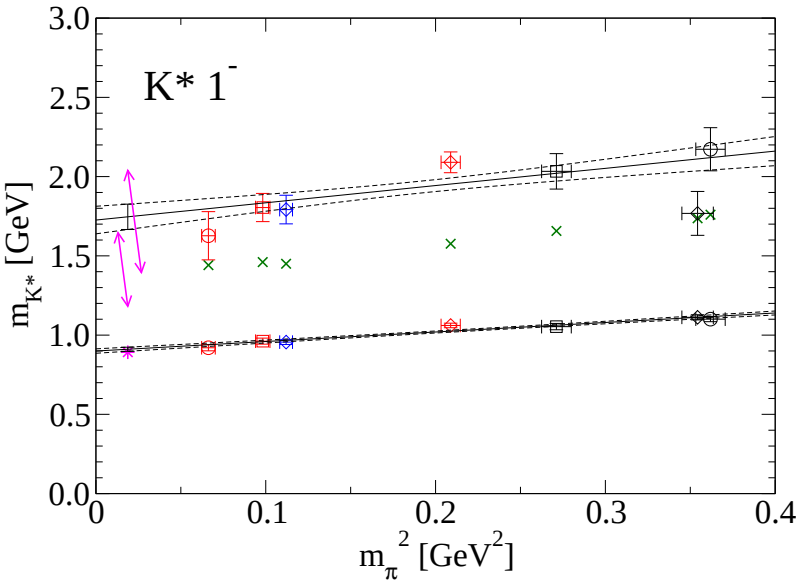

Figure 6.8: *The mass of the K^* meson ($J^P = 1^-$) is plotted against m_π^2 in physical units. The energy levels of the (theoretical) P wave scattering state $K\pi$ are shown as crosses. The two resonance widths are depicted as magenta lines with end-arrows, which are slightly shifted to clearly show their overlap.*

The final chiral extrapolated result for the first excited state coincides with the PDG data nicely. However, since we only include statistical errors we may underestimate the final error of our result and it could also be compatible with the $K_0^*(800)$ resonance. Thus, without further investigation by, e.g., larger lattice volumes or correlators with non-zero momentum, we cannot draw a unique conclusion concerning the quality of the state, i.e., do we see a one or a two particle state, here.

6.5 Strange quark mesons with spin 1

6.5.1 The K^*, $J^P=1^-$

In the K^* channel with $J^P = 1^-$ we can observe a very clear ground state signal and a quite reliable signal for the first excitation (see Fig. 6.8). The interpolators used are

State	A50	A66	B60	B70	C64	C72	C77
GS 1^-	1,5,8 throughout						
1E 1^-	1,8,9	1,11,12	8,9,22	8,21,22	1,8,9	9,12,22	1,8,16

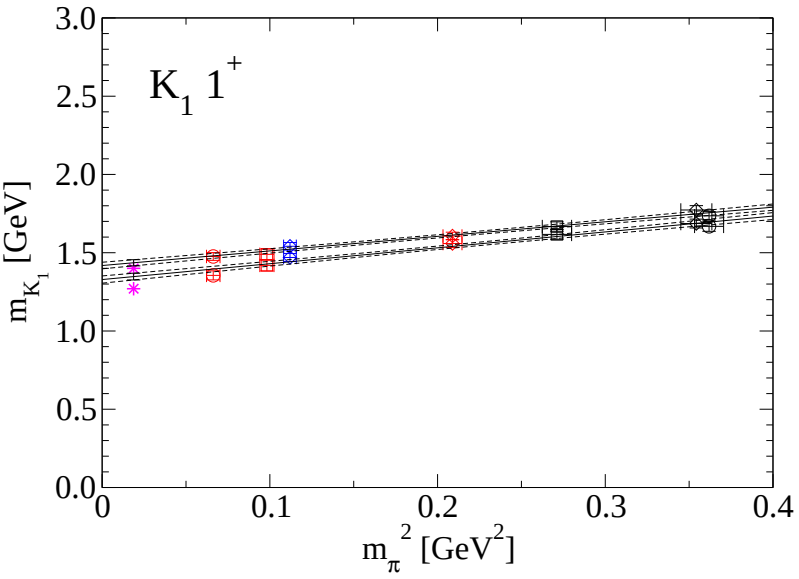

Figure 6.9: *The mass of the K_1 meson ($J^P = 1^+$) is plotted against m_π^2 in physical units.*

The ground state extrapolates – in the chiral limit – straight to the experimental data point (which again supports the chosen value for m_s). However, the situation is different for the first excitation. There, we still observe the same behavior as we did in [53]: the final result matches the $K^*(1680)$ resonance much better than the $K^*(1410)$ resonance (both shown in Fig. 6.8). Due to the same reasons as in the K_0^* meson we cannot strictly assign our result to one of the two states: the resonances are broad and overlap, and we may underestimate the error of our final result.

Finally, we want to mention one interesting point here. For extracting the ground state we only take interpolators which have $C \approx -$, since with this combination we get the best result. In the first excited state we always use a combination of interpolators with both C parities. The interesting observation now is, that in the first excited state interpolators with $C \approx +$ only contribute very little. Thus, we think that this channel is dominated from interpolators, which have $C = -$ (in the light meson sector). A reason may be, that interpolators with $J^{PC} = 1^{-+}$ correspond to exotic states, which do not exist within the quark model [105].

6.5.2 The K_1, J^P=1^+

Here, in the strange $J^P = 1^+$ channel, i.e., the K_1 meson, we can extract the two lowest lying states with very small statistical error bars (see Fig. 6.9). For both

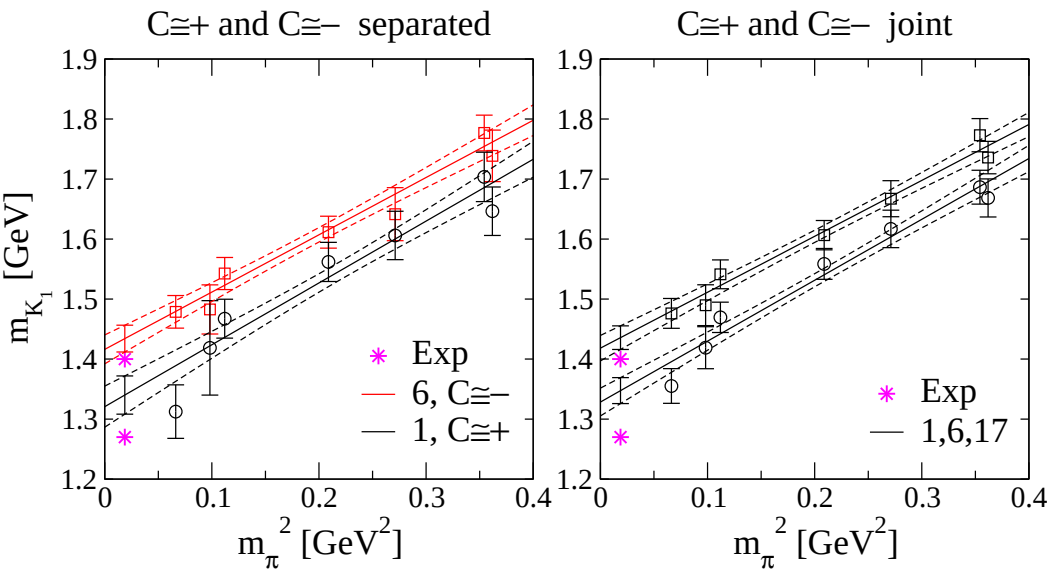

Figure 6.10: *L.h.s.: The mass of the K_1 meson is plotted against m_π^2 in physical units for using only interpolator* 1 *($C \approx +$, black) or interpolator* 6 *($C \approx -$, red). R.h.s.: The mass of the K_1 meson is plotted against m_π^2 in physical units using interpolators* $1, 6, 17$.

states we use the same interpolator combination, namely $1, 6, 17$. The results in the chiral limit seem to be compatible with the $K_1(1270)$ and the $K_1(1400)$ states, both confirmed by the PDG.

Compared to the results from the K^* channel, the situation concerning the contribution from different interpolators is much clearer here. The two possible "subgroups" of interpolators ($C \approx -$ and $C \approx +$) do exist within the quark model (in the case of mass degenerate quarks). Thus, we can try to include only interpolators of one of these two branches. The result for this approach can be seen in Fig. 6.10. On the left-hand side we show the results for the case, where only interpolator 1 (lower state) or only interpolator 6 (upper state) is used in the variational basis. The results in the chiral limit coincide (within error bars) with the results from using interpolators $1, 6, 17$ simultaneously, which is for direct comparison again plotted on the right-hand side of Fig. 6.10. Since interpolators 1 and 6 obey $C = +$ and $C = -$ (for mass degenerate quarks), respectively, we conclude that the ground state of the K_1 meson is dominated by the $J^{PC} = 1^{++}$ interpolators, whereas the first excitation is dominated by $J^{PC} = 1^{+-}$ interpolators (within our range of m_π). The behavior of the eigenvectors also confirms this picture.

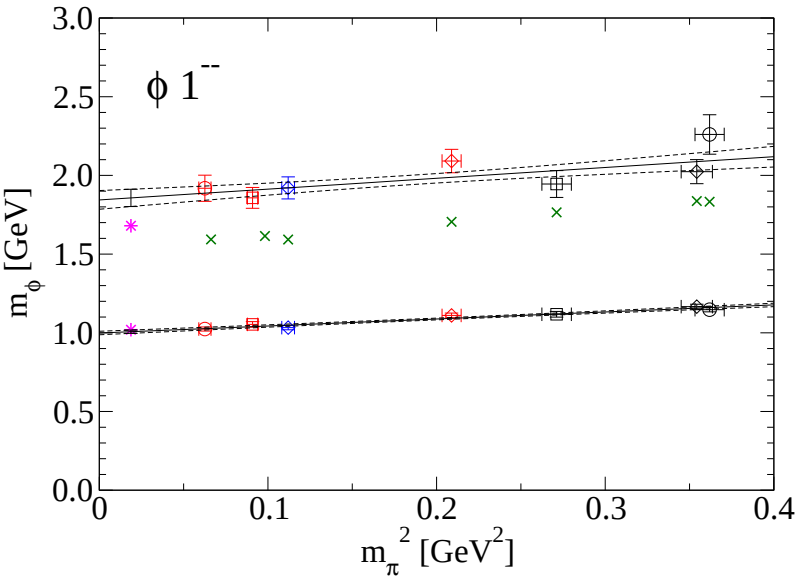

Figure 6.11: *The mass of the ϕ meson ($J^{PC} = 1^{--}$) is plotted against m_π^2 in physical units. The energy levels of the (theoretical) P wave scattering state KK are shown as crosses.*

6.6 The ϕ meson

In this section we want to confirm the chosen values for the strange quark mass parameter m_s, which is discussed in Sec. 5.4. Therefore we analyze the ϕ meson. The decay modes on this channel indicate, that it is built from a strange and an anti-strange quark, $s\bar{s}$. It shares the same J^{PC} quantum numbers as the vector meson ρ, thus we can use the interpolator basis from the ρ channel in the variational method. However, we here neglect disconnected diagrams and the justification to use this meson channel only originates from the decay channels of the ϕ meson. Of course, we have to analyze the ρ meson for partially quenched quark mass values, i.e., for the corresponding value to obtain the partially quenched strange parameters. The result of this procedure can be found in Fig. 6.11.

The ground state can be extracted with very small statistical errors and matches the experimental data point. This consistency validates again the process and outcome of setting the strange quark mass parameter m_s. Here, we seem to see a bound state, since the P wave scattering state KK does not match our data points.

For the first excitation the result for the chiral fit deviates slightly from the PDG data point. A reasons may be too small statistics and thus weak signals in the effective mass plateaus and noisy data in general.

Chapter 7

Low energy parameters

7.1 Preparing the ground

7.1.1 Renormalization

In Chap. 2 we introduced the lattice as a regulator to be able to quantize the theory. However, to complete the process of relating measured quantities to experimental values, we (mostly) have to renormalize these quantities. Masses, for example, do not have to be renormalized. This renormalization process depends, of course, on the type of regulator and the action used. One can distinguish between multiplicative and additive renormalization. The most prominent continuum renormalization scheme is the modified minimal subtraction ($\overline{\mathrm{MS}}$) scheme. From now we denote renormalized quantities with a superscript (r).

A multiplicative renormalization applies to, e.g., the pseudoscalar interpolator, the axial vector current or the vector current,

$$Z_P P = P^{(r)} \ , \quad Z_A A = A^{(r)} \ , \quad Z_V V = V^{(r)} \ . \tag{7.1}$$

Also the quark condensate or the quark mass renormalizes multiplicatively,

$$Z_S \langle \overline{u}u + \overline{d}d \rangle = \langle \overline{u}u + \overline{d}d \rangle^{(r)} \ , \quad Z_m m = m^{(r)} \ . \tag{7.2}$$

An additive renormalization constant is needed for the quark mass if the Dirac operator used is not chirally symmetric. The extra term is called residual mass, $m = m_{\mathrm{bare}} + m_{\mathrm{res}}$.

7.1.2 Normalization of smeared interpolators

All relations and identities we apply here in our lattice simulation originate from a continuum formulation of the theory. There, all objects, like interpolating fields, are point-like quantities. Thus, we have to establish a relation between the different renormalization/regularization schemes. After normalization of the fields in our theory we also have to guarantee to compare to the required point-like continuum

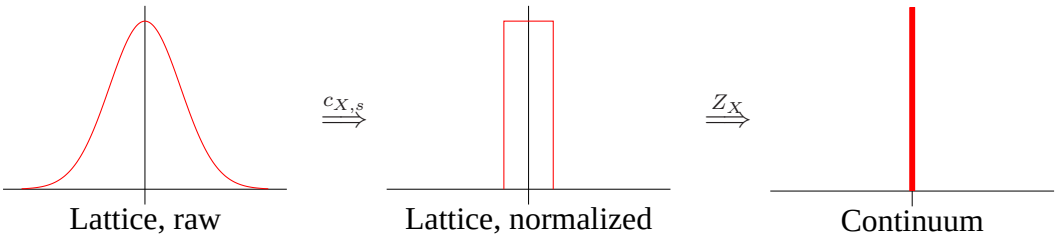

Figure 7.1: *The evolution of some field after canceling smearing effects ($c_{X,s}$) and renormalization (Z_X).*

objects. Since we often use smeared quark fields, we introduce a factor $c_{X,s}$, which accommodates for the relation of an interpolator with smearing type s, X_s, to its point-like counterpart X_p. We define this factor by

$$c_{X,s} = \frac{\langle 0 \,|X_p(t)\, Y_s(0)|\, 0\rangle}{\langle 0 \,|X_s(t)\, Y_s(0)|\, 0\rangle} \ , \tag{7.3}$$

Of course, the source interpolator Y can be any interpolator coupling to the same channel as X. The effect of the smearing of Y cancels in that fraction. To finally get rid of the influence of the smearing each smeared interpolator X_s must come with a factor $c_{X,s}$.

In Fig. 7.1 we give a more qualitative picture of these two processes. One starts with some interpolating field describing, say, some quark, defined on our lattice (left picture). After normalization (middle picture) we can compare to physical (point-like) fields like in, e.g., the $\overline{\text{MS}}$ scheme. The last step is to get rid of "lattice effects" by renormalization (right picture).

7.1.3 Ward identities

From the fact that the partition function Z is in general invariant under a transformation of variables,

$$Z = \int \mathcal{D}[\psi, \overline{\psi}]\, \mathcal{D}[U]\, e^{-S[\psi,\overline{\psi},U]} = \int \mathcal{D}[\psi', \overline{\psi}']\, \mathcal{D}[U']\, e^{-S[\psi',\overline{\psi}',U']} \ , \tag{7.4}$$

one can derive several Ward identities. For more details and examples see, e.g., [11].

One important identity is the axial Ward identity (AWI) which is given by

$$\partial_\mu\, A^a_\mu = \frac{1}{2}\, \overline{\psi}\, [m, \tau^a]_+\, \psi \ , \tag{7.5}$$

where m is the mass matrix in flavor space and τ^a is a Pauli matrix. In case of $N_f = 2$ and degenerate quark masses ($m = \text{diag}(m, m)$) Eq. (7.5) turns into

$$\partial_\mu\, A^{a(r)}_\mu = 2\, m^{(r)}\, P^{a(r)} \ . \tag{7.6}$$

This relation will be used in the following sections.

7.2 The axial Ward identity mass

Evaluating Eq. (7.6) between the vacuum and a pion field, we obtain a relation for determining the renormalized quark mass,

$$\langle 0|\partial_\mu A_\mu^{a(r)}|\pi\rangle \sim 2\, m^{(r)}\, \langle 0|P^{a(r)}|\pi\rangle \ . \tag{7.7}$$

In our case (Euclidean formulation) this relation only holds asymptotically, i.e., for large times t, where a plateau can be identified (symbol $\sim$). For the pion field π one takes some operator X which creates a pion from the vacuum, $X|0\rangle = |\pi\rangle$. We finally end up with the following equation to determine the renormalized quark mass,

$$2\, m^{(r)} \sim \frac{c_A}{c_P} \frac{\langle 0|\partial_t A_4^{(r)}(\boldsymbol{p}=0,t)\ X^{(r)}(0)|0\rangle}{\langle 0|P^{(r)}(\boldsymbol{p}=0,t)\ X^{(r)}(0)|0\rangle} \ , \tag{7.8}$$

where all interpolators are projected to zero spatial momentum $\boldsymbol{p} = 0$. For X an interpolator coupling to the quantum numbers of the pion must be used; we take P, because with this choice the plateaus are most stable. If one neglects the renormalization constants Z_A, Z_P the ratio (7.8) is called the AWI-mass $m_{\rm AWI}$. It holds

$$m^{(r)} = \frac{Z_A}{Z_P}\, m_{\rm AWI} \ . \tag{7.9}$$

The detailed pion interpolators are

$$P = \overline{d}\,\gamma_5\, u \ , \tag{7.10}$$

$$A_4 = \overline{d}\,\gamma_t\,\gamma_5\, u \ , \tag{7.11}$$

where γ_t is the Dirac matrix in time-direction. Comparing to Tab. B.3, we can choose interpolator $1, 2, 4$ for P and $5, 6, 8$ for A_4 (of course, both interpolators should obey the same smearing for the two quark fields). The time-derivative in Eq. (7.8) is done with a local 3-point fit, involving values at $(t-1, t, t+1)$. Therefrom half-integer values are avoided. For the functional behavior we assume a cosh-form instead of one single exponential for the correlators.

From Eq. (7.6) another important relation can be derived,

$$F_\pi^2\, m_\pi^2 = -N_f\, m^{(r)}\, \Sigma^{(r)} \ , \tag{7.12}$$

where F_π is the pion decay constant (see Sec. 7.3) and Σ is the quark condensate. This relation was established in a pioneering paper [106] and is known as the

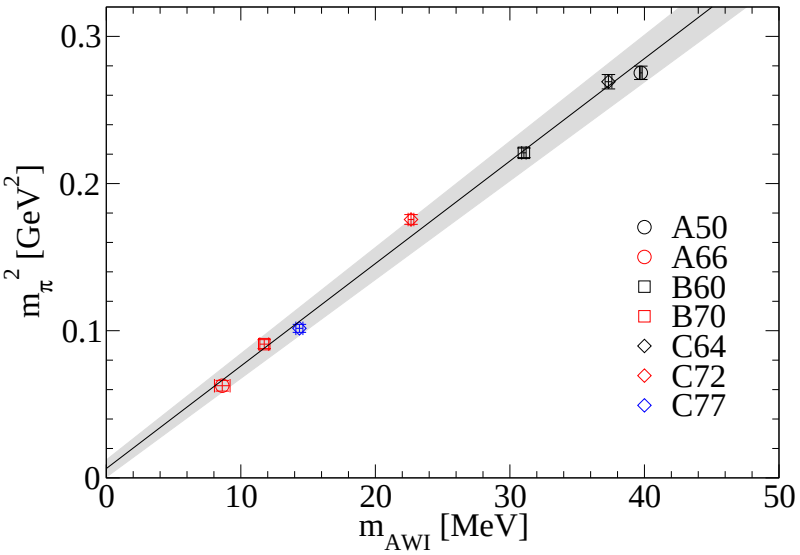

Figure 7.2: *We plot m_π^2 against the unrenormalized quark mass m_{AWI} for each set of gauge configurations. The black line is a linear fit to the data and the error of the fit is shown as gray band around this line.*

Gell-Mann–Oakes–Renner (GMOR) relation. This paper paved the way to a new approach in quantum field theory, namely chiral perturbation theory [90, 91, 92]. For a nice overview see also [107] and references therein.

In Fig. 7.2 we show the dependence of m_π^2 on the AWI-mass. We perform a linear fit of the data, therefrom it can be seen that the expected behavior (cf. Eq. (7.12)) is nicely fulfilled and the data points are lying within the estimated (gray) error band.

7.3 The pion decay constant

The pion decay constant describes the weak decay of the pseudoscalar meson π. One uses again Ward identities to obtain a defining equation for F_π, for details we want to refer the reader to standard text books. In our simulation we use two different relations from which we can extract the value of F_π. We then can compare the different results and thus have a cross-check for the setup.

The first identity is given by

$$c_A^2 \, Z_A^2 \, \langle A_4(\boldsymbol{p}=0,t) \, A_4(0) \rangle \sim m_\pi \, F_\pi^2 \, e^{-m_\pi t} \ . \tag{7.13}$$

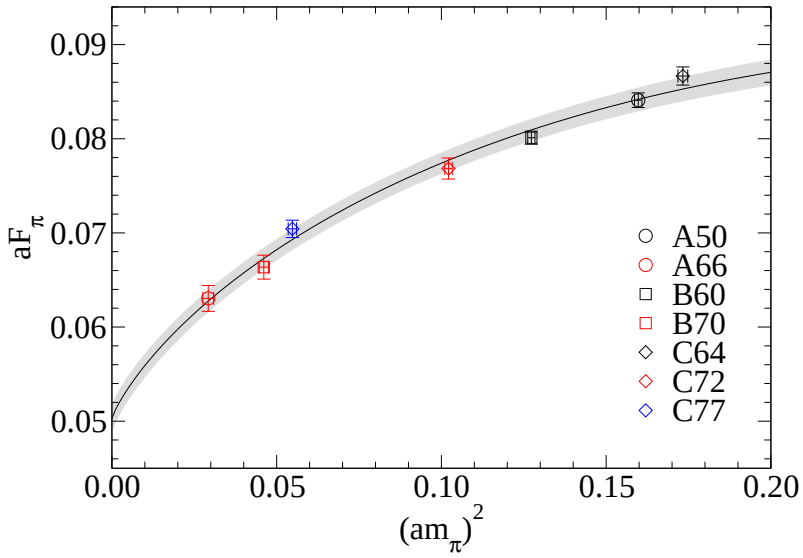

Figure 7.3: *The pion decay constant F_π is plotted against m_π^2 (all in dimensionless units) for each set of gauge configurations. The black line is a fit of the data and the estimated errors are shown as gray envelope around that line.*

The other possibility is to employ

$$c_P^2\, Z_P^2\, \langle P(\boldsymbol{p}=0,t)\, P(0)\rangle \sim \frac{m_\pi^3\, F_\pi^2}{4\, m^{(r)2}}\, e^{-m_\pi t}\ . \tag{7.14}$$

In both cases one performs a fit to the given exponential behavior and can then calculate F_π from the fitted coefficient in front of the exponential. From Eq. (7.13) we get

$$F_\pi = c_A\, Z_A \sqrt{\frac{\text{coeff.}}{m_\pi}}\ , \tag{7.15}$$

and (7.14) gives

$$F_\pi = 2\, m^{(r)}\, c_P\, Z_P \sqrt{\frac{\text{coeff.}}{m_\pi^3}} = 2\, m_{\text{AWI}}\, c_P\, Z_A \sqrt{\frac{\text{coeff.}}{m_\pi^3}}\ . \tag{7.16}$$

The values of both methods agree, which validates our setup to be correct.

The dependence of the pion decay constant on the quark mass can be described by chiral perturbation theory. Up to 1-loop order we find [90]

$$F_\pi = F_{\pi,0} - m\, \frac{2\,\Sigma_0}{16\,\pi^2 F_{\pi,0}^3}\, \ln\left(m \frac{2\,\Sigma_0}{\Lambda_4^2 F_{\pi,0}^2}\right)\ . \tag{7.17}$$

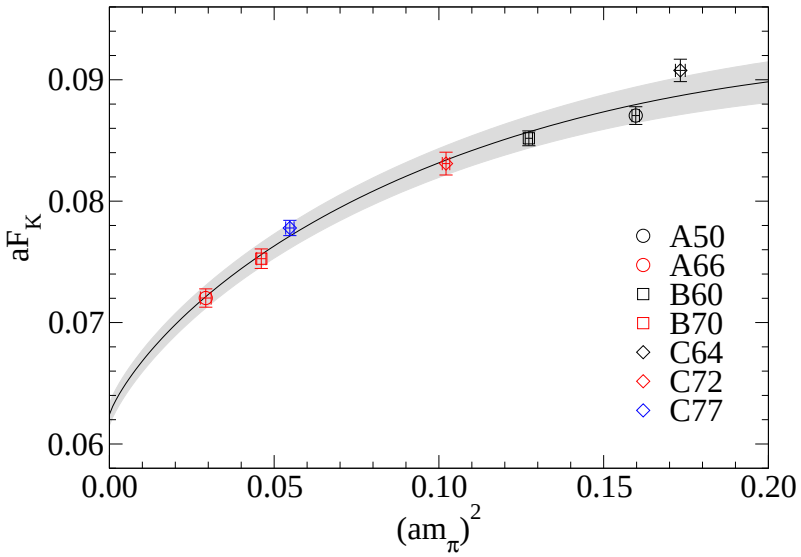

Figure 7.4: *Same as Fig. 7.3, now for the kaon decay constant F_K.*

Here, $F_{\pi,0}$ and Σ_0 refer to the pion decay constant and the quark condensate in the chiral limit $m \to 0$ and Λ_4 is some low energy constant. The corresponding expressions including the 2-loop order can be found in [108].

Since the quark mass is proportional to the pion mass squared (see Eq. (7.12)), we also know the relation between F_π and m_π^2. Thus, we can transform Eq. (7.17) into an equation in which F_π only depends on m_π^2. Such an expression can be fitted with a two-parameter fit, figuring out the values for $F_{\pi,0}$ and Λ_4.

In Fig. 7.3 we plot the value of F_π against m_π^2 (all in dimensionless units) for each set of gauge configurations. The black line is a function of the form (7.17) and the fit errors are shown as gray envelope around. One can see, that our results are described very well by the assumed behavior and are all lying within the estimated error.

7.4 The kaon decay constant

As there also exist pseudoscalar mesons which do not consist of light quarks only, but are built from a light and a strange quark, we can use the apparatus developed in Sec. 7.3 to determine the decay constant of the lightest of these mesons, the kaon, too. We can apply the equations from above and thus extract the values for each set of gauge configurations. In Fig. 7.4 F_K plotted against m_π^2. Also like for the pion, the data can be nicely fitted to the form expected from chiral perturbation theory

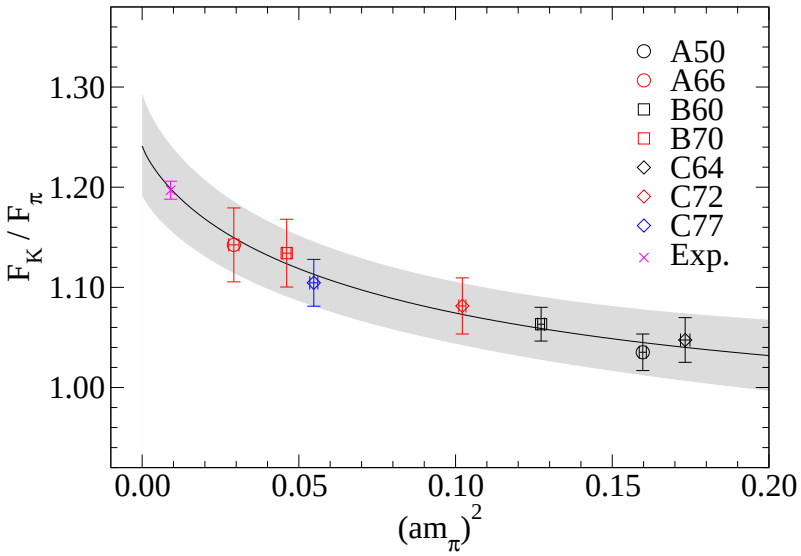

Figure 7.5: *The ratio of F_K/F_π is plotted against m_π^2 (in dimensionless units) for each set of gauge configurations. The black line is a fit of the data using the relevant expressions for numerator and denominator. The magenta cross indicates the experimental value [9].*

and all data points are located within the error band.

To draw a connection to the experiment we compute the ratio of the two decay constants, since such a quantity does no longer depend on the scale a. The values are seen in Fig. 7.5. For the ratio F_K/F_π the experimental value is determined as [9]

$$F_K/F_\pi = 1.197 \pm 0.009 \tag{7.18}$$

In Fig. 7.5 we show that at a value for the abscissa, where we assumed a lattice spacing of 0.135 fm (average of our values for the mass independent scheme) and a physical pion mass of 139.57 MeV [9]. The extrapolation of our data to that point gives

$$F_K/F_\pi = 1.199 \pm 0.043 \ , \tag{7.19}$$

which fully covers the experimental range.

Chapter 8

The angular momentum content of the vector meson

8.1 Hadron decomposition

In a quantum field theory the description of the composition of a hadronic state is a quite artful issue. Since the concept of a wave function and a complete basis of states has a sound definition in non-relativistic approaches only, one suffers from the absence of a proper definition for a hadron beyond the ground state in a quantum field theory. There the situation is such that a given hadron interpolator (with definite quantum numbers) in principle couples to all states and thus the state always has contributions from scattering states, i.e., a superposition of many particle components. As a consequence, lattice QCD studies concerning hadrons mainly deal with quantities like, e.g., spectroscopy, axial couplings, forms factors, etc. However, to get some insight into the hadron composition, i.e., understanding the hadronic structure from an *ab initio* calculation, is a tough project.

Of course, a huge amount of different Fock components are present in a hadron. Thus, it is very demanding, if not impossible, to reconstruct a hadron on the lattice. Fortunately, as we can learn from phenomenological data and modeling of hadrons, only a few of the Fock components are the dominant ones. To get a more intelligible picture of these leading components would be a great benefit for improving our knowledge about the hadron structure.

Using the variational method (see Sec. 4.3) we can study the hadron wave function in lattice QCD. What we are interested in is the reconstruction of the leading quark-antiquark component of low lying mesons. Therefore we need interpolators that allow us to determine such a component in an unique way. Additionally, such a set of interpolators must be complete with respect to the chiral basis.

In [109, 110] a classification according to the transformation properties with respect to the $SU(2)_L \times SU(2)_R$ and $U(1)_A$ was done for all non-exotic interpolators in the light meson sector. If no explicit excitation of the gluonic field with non-vacuum quantum numbers is present, this basis is a complete one for a quark-antiquark sys-

tem and we can investigate chiral symmetry breaking. We then can reconstruct the decomposition for a given meson in terms of different representations of the chiral group by diagonalizing the cross-correlation matrix C_{ij}. The eigenvectors describe the quark-antiquark content in terms of different chiral representations. This means that chiral symmetry is broken if we observe components with different transformation properties in terms of $SU(2)_L \times SU(2)_R$ and $U(1)_A$.

To establish a connection to the quark model [105], we can reconstruct the meson composition in terms of the $^{2S+1}L_J$ basis, where $\mathbf{J} = \mathbf{L} + \mathbf{S}$ are the standard angular momenta. Although there is some kind of understanding that results of the quark model are related to chiral symmetry breaking, an independent and gauge invariant approach to answer this question is still missing. Thus, the composition of the leading quark-antiquark component in terms of the $^{2S+1}L_J$ basis in the infrared, i. e., where the hadron mass is generated, would tell us to which degree the quark model language is adequate for a given state.

We can roll out the decomposition of the leading quark-antiquark component in the angular momentum basis. The $^{2S+1}L_J$ angular momentum basis and the chiral basis are both complete for a two particle system. They are connected by a unitary transformation. It was shown in [111, 112] that each state of the chiral basis can be uniquely represented in terms of the $^{2S+1}L_J$ states. Then, diagonalizing the cross-correlation matrix, built from interpolators with definite chiral transformation properties, one can obtain the partial wave decomposition of the leading Fock component, using the unitary transformation from [111, 112].

This method can in principle be applied to any meson, here we use as an example the vector meson ρ. First results of the application of this method, which involve only the ground state ρ, can be found in [113, 114]. In [115, 116] results which mainly focus on the first excitation of the vector meson, ρ', were published.

8.2 Chiral classification and angular momentum basis

The classification of the quark-antiquark states and interpolators with respect to the representations of $SU(2)_L \times SU(2)_R$ was done in [109, 110]. We are interested in the quark-antiquark component of the ground state ρ meson and its first excitation. There are two possible chiral representations (which we denote as $\mathcal{R}$) that are compatible with the quantum numbers of the ρ meson: $\mathcal{R} = (0,1) \oplus (1,0)$ and $\mathcal{R} = (1/2,1/2)_b$. These representations have drastically different chiral transformation properties (see [109, 110] for details). Assuming that chiral symmetry is not broken, then one has two independent states. The first state is $|\mathcal{R};\, I\, J^{PC}\rangle = |(0,1) \oplus (1,0);\, 1\, 1^{--}\rangle$ and can be created from the vacuum by the standard vector

current

$$O_V = \overline{q}\,\gamma_i\,\vec{\tau}\,q\ . \tag{8.1}$$

The other state is $|\mathcal{R};\, I\,J^{PC}\rangle = |(1/2,1/2)_b;\, 1\,1^{--}\rangle$, which can be created by the pseudotensor operator,

$$O_T = \overline{q}\,\sigma_{0i}\,\vec{\tau}\,q\ . \tag{8.2}$$

Here, I denotes the isospin and $\vec{\tau}$ the vector of isospin Pauli matrices.

Chiral symmetry breaking in the state implies that the state should be a mixture of both representations. If it is a superposition of both representations with approximately equal weights, then chiral symmetry is maximally violated in this state. If, otherwise, one of the representations strongly dominates over the other representation, one could speak about effective chiral restoration in this state.

These chiral representations can be transferred into the $^{2S+1}L_J$ basis, using the unitary transformation [111, 112]

$$\begin{pmatrix} |(0,1)\oplus(1,0);\, 1\,1^{--}\rangle \\ |(1/2,1/2)_b;\, 1\,1^{--}\rangle \end{pmatrix} = U\cdot\begin{pmatrix} |1;\,^3S_1\rangle \\ |1;\,^3D_1\rangle \end{pmatrix}\ , \tag{8.3}$$

where U is given by

$$U = \begin{pmatrix} \sqrt{\frac{2}{3}} & \sqrt{\frac{1}{3}} \\ \sqrt{\frac{1}{3}} & -\sqrt{\frac{2}{3}} \end{pmatrix}\ . \tag{8.4}$$

Thus, using the interpolators O_V and O_T from Eqs. (8.1) and (8.2) for the diagonalization of the cross-correlation matrix, we are able to reconstruct the partial wave content of the leading Fock component of the ρ meson, if this unitary transformation is applied.

8.3 Reconstruction of the wave function

We briefly want to discuss how to analyze the decomposition of the ρ meson using the variational method. The time propagation properties of the normalized physical states $|n\rangle$ are given by

$$\langle n(t)|m(0)\rangle = \delta_{n,m}e^{-E_n t}\ . \tag{8.5}$$

However, the lattice interpolators O_i are typically not normalized and are projected to zero spatial momentum.

The cross-correlation matrix C_{ij} can be written as

$$C_{ij}(t) = \langle O_i(t)\; O_j^\dagger(0)\rangle\ = \sum_n a_i^{(n)} a_j^{(n)*} e^{-E_n t}\ , \tag{8.6}$$

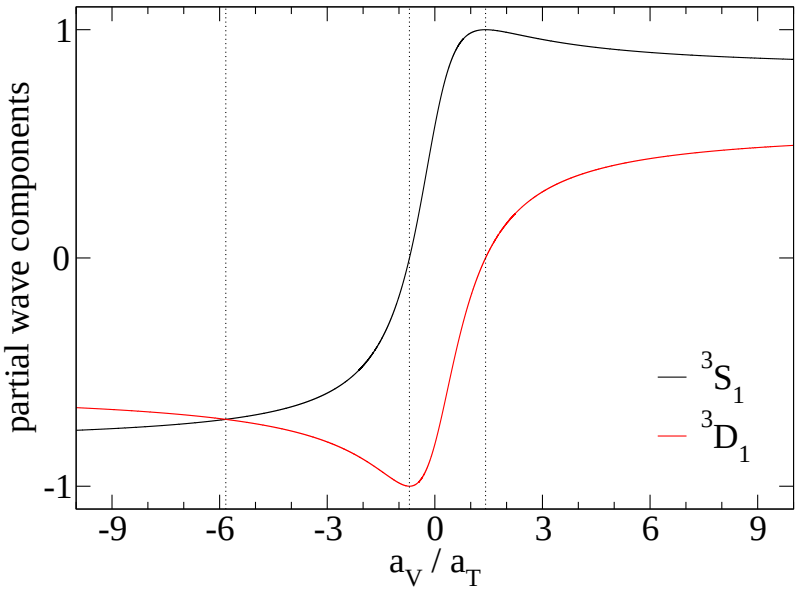

Figure 8.1: *The fractions of* $|1;\,^3S_1\rangle$ *and* $|1;\,^3D_1\rangle$ *are plotted against* a_V/a_T*. Special values, as discussed in Eq.* (8.9)*, are indicated by dotted lines.*

where the coefficients $a_i^{(n)}$ give us the overlap of the physical state $|n\rangle$ with the lattice interpolator O_i,

$$a_i^{(n)} = \langle 0|O_i|n\rangle \ . \tag{8.7}$$

The wave function of the state $|n\rangle$ would essentially be built from these coefficients if the basis of interpolators $\{O_i\}$ would be orthogonal. The two chiral representations $(0,1)\oplus(1,0)$ and $(1/2,1/2)_b$ form a complete and orthogonal basis (with respect to the chiral group) for ρ mesons. Consequently, using the variational method we are able to study the mixing of the two representations in both ρ and ρ' states.

Following the lines of [113, 114], one can show that the ratio of couplings can be written as (j is summed!)

$$\frac{a_i^{(n)}(t)}{a_k^{(n)}(t)} = \frac{C_{ij}(t)\,u_j^{(n)}(t)}{C_{kj}(t)\,u_j^{(n)}(t)} \ . \tag{8.8}$$

The ratio of the vector to the pseudotensor coupling, $a_V^{(n)}/a_T^{(n)}$, tells us something about chiral symmetry-breaking in the states $n=\rho,\rho'$.

Finally we want to give a qualitative view on the ratio (8.8). Inverting Eqs. (8.3) and (8.4) we can compute the $|1;\,^3S_1\rangle$ and $|1;\,^3D_1\rangle$ components of the analyzed state from the ratio a_V/a_T. In Fig. 8.1 these components are plotted against the ratio.

Three special cases are indicated by a dotted line, namely

$$\begin{aligned} \frac{a_V}{a_T} = -3 - 2\sqrt{2} \quad &\Longrightarrow \quad -\frac{1}{\sqrt{2}}\,|1;\,^3S_1\rangle - \frac{1}{\sqrt{2}}\,|1;\,^3D_1\rangle\ , \\ \frac{a_V}{a_T} = -\frac{1}{\sqrt{2}} \quad &\Longrightarrow \quad -|1;\,^3D_1\rangle\ , \\ \frac{a_V}{a_T} = \sqrt{2} \quad &\Longrightarrow \quad |1;\,^3S_1\rangle\ . \end{aligned} \tag{8.9}$$

In the first case the fractions of $|1;\,^3S_1\rangle$ and $|1;\,^3D_1\rangle$ are equal, for the other two cases the state is a pure $|1;\,^3D_1\rangle$ or $|1;\,^3S_1\rangle$ state, respectively.

8.4 Defining the resolution scale

If we probe the hadron structure with local interpolators, then we study the hadron decomposition at a scale, fixed by the lattice spacing a. For a reasonably small a, this scale is close to the ultraviolet. However, we are interested in the hadron content at infrared scales, where mass is generated. For this purpose we cannot simply use a large a, because then the matching with the continuum QCD will be lost due to lattice artifacts. Given a fixed, reasonably small, lattice spacing a, a large infrared scale R can be achieved by gauge-invariant smearing of the point-like interpolators. We smear the quark fields (sources) in spatial directions over the size R in physical units, such that $R/a \gg 1$. Then, even in the continuum limit $a \to 0$ we probe the hadron content at the infrared scale fixed by R. Such a definition of the resolution is similar to the experimental one, where an external probe is sensitive only to quark fields (it is blind to gluonic fields) at a resolution that is determined by the momentum transfer in spatial directions.

The smearing itself is done with the Jacobi smearing procedure discussed in Sec. 4.4. It creates an approximately Gaussian profile of the width $2R$ for each quark field of the smeared interpolators.

8.5 Technical details and results

As already discussed above, we apply this apparatus only for the ρ meson. Since this study was done in an earlier stage of this work, data is only available for three sets of gauge configurations, namely sets A50, B60 and C77.

The cross-correlation matrix is built from four different interpolators. According

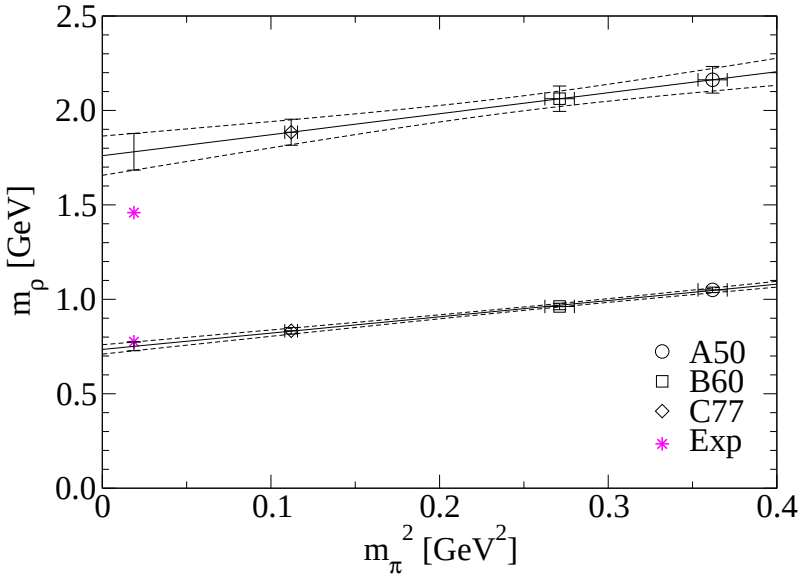

Figure 8.2: *The mass of the vector meson ρ, extracted using interpolators $1, 4, 5, 8$ from Tab. B.5, is plotted against m_π^2 in physical units.*

to the notation from Chap. 6 and Table B.5 from Appendix B, these are

$$O_1 = \overline{u}_n \, \gamma_k \, d_n \ , \tag{8.10}$$

$$O_4 = \overline{u}_w \, \gamma_k \, d_w \ , \tag{8.11}$$

$$O_5 = \overline{u}_n \, \gamma_k \, \gamma_t \, d_n \ , \tag{8.12}$$

$$O_8 = \overline{u}_w \, \gamma_k \, \gamma_t \, d_w \ . \tag{8.13}$$

Of course, the spatial directions $k = 1, 2, 3$ are averaged and γ_t is the Dirac matrix in (Euclidean) time direction. The sources have an approximate width of 0.35 fm (index n) and 0.67 fm (index w), as given in Tab. 4.1 in Sec. 4.4. Although we used another interpolator combination to extract the masses of the ρ meson in Chap. 6, we are also able to extract both the ground state mass and the mass of the first excited state of the ρ meson, using this combination. A plot of these masses can be found in Fig. 8.2.

In Fig. 8.3 we show the R-dependence of the ratio from Eq. (8.8), both for the ground state ρ meson and its first excited state ρ'. This ratio of the vector to the pseudotensor coupling to the states shows us their decomposition in terms of the $(0,1) \oplus (1,0)$ and $(1/2,1/2)_b$ representations. For the ground state at a resolution scale of $R \approx 0.67$ fm this ratio is approximately 1.2, i. e., we see a strong mixture of the two representations in the wave function of the ground state ρ meson. Inverting

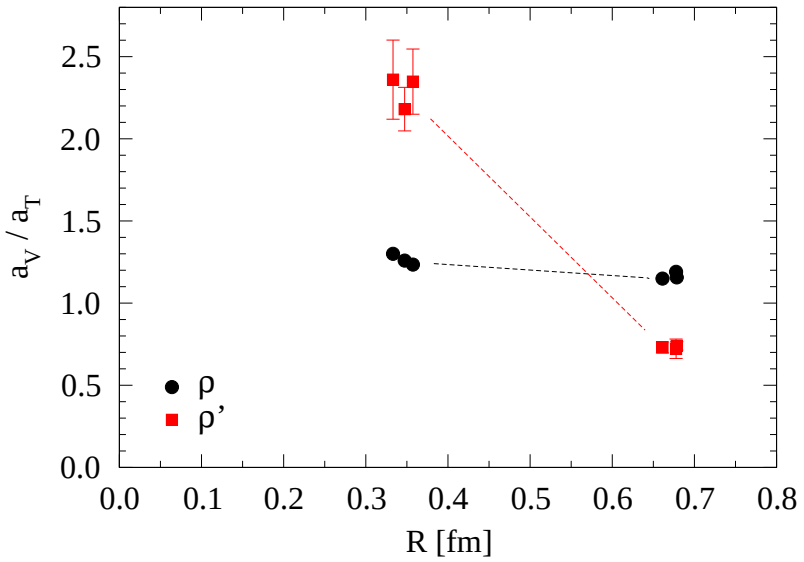

Figure 8.3: *The ratio a_V/a_T is plotted against the smearing width R for the data sets A50, B60 and C77. Black circles represent the ground state and red squares the first excitation. Dashed lines are drawn only to guide the eye.*

the unitary transformation from Eq. (8.3) results in the fact that the vector meson is predominantly a $|1;\,^3S_1\rangle$ state with a tiny admixture of a $|1;\,^3D_1\rangle$ wave (cf. Fig. 8.1). To be more precise, the state is $0.997\,|1;\,^3S_1\rangle - 0.079\,|1;\,^3D_1\rangle$. This result is not changed qualitatively if we do an extrapolation to values of R much bigger than our smearing widths [113, 114], which indicates that the ground state $\rho(770)$ is approximately a $|1;\,^3S_1\rangle$ state – in agreement with the quark model.

However, the situation changes dramatically for the first excited state, $\rho' = \rho(1450)$. There, a significant contribution comes from the $(1/2, 1/2)_b$ representation. Of course we cannot perform a reliable continuation to the deep infrared scale, since we only have two R values at hand. At such a scale the value of a_V/a_T will be small, unclear if it obeys a positive or negative absolute value. Simulations using sources with an approximate width of ≈ 0.85 fm are under way but the analysis is not finished yet. Around that width we expect that the ratio vanishes.

The interpretation is as follows. From the conformal symmetry of QCD and from renormalization group analysis one expects that the pseudotensor interpolator decouples from the ρ meson. Thus, the ratio a_V/a_T must increase for small R. At large R the ratio determines a degree of chiral symmetry breaking in the infrared region, where mass is generated. In contrast to the $\rho(770)$, such a breaking is insignificant for the $\rho(1450)$. The chiral decomposition of the ρ' is dominated by

only one of the chiral representations. This leads to an indication of a smooth onset of effective chiral restoration. Since the dominating representation for the ρ' is $(1/2,1/2)_b$, one predicts that in the same energy region there must exist a h_1 (and not an a_1) meson. And in fact there is a state $h_1(1380)$ and no a_1 state in the same energy region [9].

The main conclusion is the following. In the $\rho(770)$ meson chiral symmetry is strongly broken, since this state is a strong mixture of $(0,1)\oplus(1,0)$ and $(1/2,1/2)_b$. Consequently, its "would-be chiral partners" have a much larger mass: $a_1(1260)$ and $h_1(1170)$. To each of these low lying states we cannot assign any chiral representation. For the $\rho(1450)$ the contribution from $(1/2,1/2)_b$ is much bigger than the contribution of the other representation, and consequently its approximate chiral partner is the $h_1(1380)$. The second excited ρ meson, the $\rho(1700)$, should then be dominated by the representation $(0,1)\oplus(1,0)$. This assumption is favored by the existence of the $a_1(1640)$ state [9]. However, this $a_1(1640)$ meson can not be motivated by the quark model [117].

Although we do not have the value of the ratio a_V/a_T for $\rho(1450)$ at large R, there is an indication that this value is small. Then we are able to give a qualitative estimate for the angular momentum content of the $\rho(1450)$ in the infrared. If the ratio vanishes, the state would have the following partial wave content,

$$\sqrt{\frac{1}{3}}\,|1;\,^3S_1\rangle - \sqrt{\frac{2}{3}}\,|1;\,^3D_1\rangle\ . \tag{8.14}$$

This shows a significant contribution of the $|1;\,^3D_1\rangle$ wave. Even if the ratio varies slightly for large R, the qualitative result does not change. This result is inconsistent with ρ' to be a radial excitation of the ground state ρ meson, i. e., a $|1;\,^3S_1\rangle$ state, as predicted by the quark model [105].

Chapter 9

Conclusions and outlook

9.1 Summary of the technical details

We want to start this chapter by summarizing all technical details of the present work. Seven sets of gauge configurations, all for a lattice size of $16^3 \times 32$ have been created. They include two dynamical, mass degenerate light quarks and pion masses ranging from 260 to 600 MeV. The lattice spacings vary from 0.135 to 0.158 fm (in the mass dependent scheme) or rather from 0.131 to 0.138 fm in the mass independent scheme. We used the Lüscher-Weisz gauge action and the Chirally Improved Dirac operator, including one level of stout link smearing, which is one part of the definition of our Dirac operator. These configurations have been generated with the Hybrid Monte Carlo algorithm, using several improvements, such as Hasenbusch mass preconditioning and a mixed precision inverter. In each set we used 200 or 300 independent gauge configurations for the analyses. We think that our implementation is safe concerning the development of exceptional configurations. The mass parameter for the (partially quenched) strange quark was fixed using the mass of the positive parity Ω baryon. The quark propagators are created on Jacobi smeared or derivative smeared quarks sources, using three times HYP smeared gauge configurations.

9.2 Results from hadron spectroscopy

9.2.1 Baryons

For the spectroscopy of baryons (and also mesons) we used the variational method. Here, we worked with two different types of Jacobi smeared quark sources. Since for most of the baryons we had multiple Dirac structures which we could employ, the basis of interpolators for the variational method had a reasonable size. To guarantee for the best comparability we have chosen the same combination of interpolators and the same time range for the fit of the eigenvalues in each channel. An extrapolation of our data to the physical pion mass was done using a linear fit in m_π^2, motivated

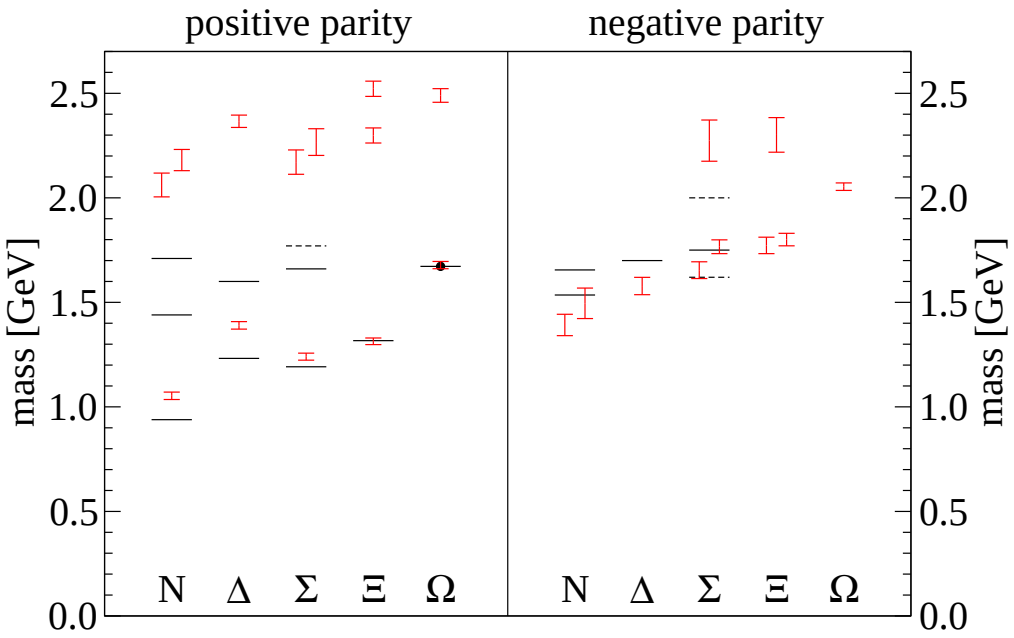

Figure 9.1: *For each channel we plot the range of the baryon mass (as vertical red line), obtained from the chiral fit of the different sets of gauge configurations. The mean values of the experimental energy levels are shown as horizontal straight black lines, states unconfirmed by the PDG are shown as horizontal dashed black lines. In the case of the positive parity Ω a black circle indicates the experimental value, since we use this data point as input. On the left panel the positive parity results are shown and on the right panel the negative parity results can be found.*

by chiral perturbation theory. A collection of the results of these fits can be found in Fig. 9.1 for all baryon channels. For all particles considered we could extract the ground state energy level with fairly small statistical errors; except for the negative parity Δ and Ω baryon, we also could get a signal for the first (or even second) excitation.

Positive parity

In the positive parity sector we slightly overestimate (except for the Ξ) the value for the ground states, but the obtained signals all have rather small statistical errors. The extracted energy levels for the excitations exceed the experimental data sometimes drastically. However, in the Ξ or the Ω channel we could get signals for states, which are not listed by the PDG. We did not see an indication for the first excited nucleon, the Roper resonance: our signal is much higher.

There may be various reasons for the high values we observe. First of all, this can be a finite volume effect, i.e., the particles could be squeezed due to the limited spatial lattice volumes we use. Another point, which of course cannot be neglected, is the limited statistics we deal with. The plateaus in the effective mass are sometimes short and rather noisy. Thus, improved statistics could shed a bit more light on some situations. The third important point concerns the interpolator basis we have at hand, it lacks two particle interpolators. Hence, we often are not able to draw a distinct conclusion about the particle content of the analyzed channel, i.e., it may be possible that we see a scattering instead of a bound state.

Negative parity

Except for the Σ, we have underestimated the ground state signals for the negative parity baryons compared to the PDG data. In most of the channels we encountered the same circumstances as for the positive parity, a reliable identification whether a bound or scattering state is observed was not possible. The first excitation of the nucleon is also below the experimental value. In the case of the Σ our signal of the first excitation matched the experimental value and the existence of the $\Sigma(2000)$. For the Ξ and Ω baryons up to now no state confirmed by the PDG exists. We could, however, get signals with reasonable errors in these cases.

9.2.2 Mesons

To obtain the results for the meson mass spectrum we used, in addition to the Jacobi smeared sources, also derivative smeared quark sources. We analyzed spin 0 and spin 1 mesons, both in the light and the light/strange sector. As for the baryons, we tried to find an overall combination of interpolators and time range, which gives rise to a fair signal for each set. Unfortunately this was not possible everywhere. A linear fit in m_π^2 of the final data was performed to get the values presented in Fig. 9.2. In general, the expected spectrum was nicely reproduced and except for the tensor meson b_1 the ground state and the first excitation could be measured.

Mesons built from light quarks

Five different mesons, built from only up and down quarks, were analyzed in this work. We do not discuss the ground state of the pseudoscalar meson π, since these masses served as scale for our plots of hadron masses. The other ground state signals matched the PDG data very well, only the mass of the b_1 was overestimated by about 10%. The energy levels of the first excited states were also compatible within two

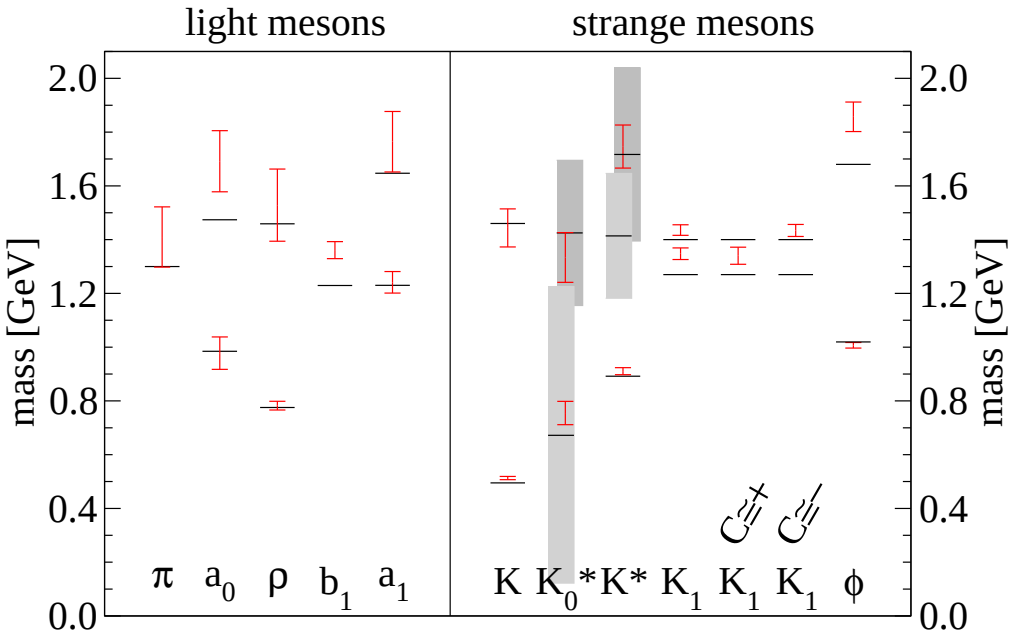

Figure 9.2: *For each channel we plot the range of the meson mass (as vertical red line), obtained from the chiral fit of the different sets of gauge configurations. The mean values of the experimental energy levels are shown as horizontal black lines. Grey bars indicate the full width of the corresponding resonance. On the left panel the mesons consisting of only light quarks are shown, while on the right panel we show mesons built from one light and one strange quark.*

standard deviations.

Mesons including strange quarks

Here, we mostly found excellent agreement of our data for the ground states with the experimental values. This fact strengthened our choice of the strange quark mass parameter. In the K_0^* and the K^* channels the assignment of states to a definite channel was not really possible, since these particles are broad resonances. The values of the first excited states were also fully compatible with the experimental values. For the case of the K_1 meson we could show that different energy levels are dominated by interpolators with different C parity, although this quantum number, strictly speaking, does hold only for mass degenerate quarks.

9.3 Results for low energy parameters

With our sets of gauge configurations we also analyzed low energy parameters. From the axial Ward identity we could obtain a relation for the (unrenormalized) quark mass, the AWI-mass m_{AWI}. Additionally we could check the relation between the quark mass and the pion mass, the famous Gell-Mann–Oakes–Renner relation. We found the expected linear behavior to be fulfilled very nicely.

The pion and kaon decay constants also have been investigated. There, we found very reasonable results for the fits of our data with a formula motivated by chiral perturbation theory. However, we did not include renormalization constants in our calculations. The (scale independent) ratio of these two decay constants perfectly matched the experimental value.

9.4 Results from angular momentum analysis of the vector meson

For the gauge configuration sets A50, B60 and C77 we did an analysis of the decomposition, concerning the dominant quark-antiquark components, of the vector meson ρ. More precisely, we analyzed the coupling of the ρ meson to interpolators with different chiral transformation properties. After application of a unitary transformation, we could get the decomposition in terms of the angular momentum basis, i.e., the ${}^{2S+1}L_J$ basis. From the quark model it is known that both, the ground state $\rho(770)$ meson and its first excitation $\rho(1450)$, are pure $|1;\, {}^3S_1\rangle$ states. The results we have obtained could confirm the situation for the ground state but gave a contradictory picture for the first excitation, where we expect the major contribution from the $|1;\, {}^3D_1\rangle$ state.

9.5 Outlook

Of course, as for nearly every scientific task, after finishing the work, a lot of possible improvements come into ones mind. Let us shortly mention some points, which may help to get a clearer picture in some cases.

Due to limited computational power we are forced to work with small and rather coarse lattices. Especially for the hadron mass spectrum we would need bigger lattice volumes with a finer lattice spacing to be able to get a higher resolution, which means particularly longer effective mass plateaus with less fluctuation. Additionally, increasing the statistics (preferably for the sets A66 and B70) can help to identify

effects which may be hidden on the limited number of available configurations. We then could draw more definite conclusions concerning the quality of the state, i.e., do we observe a scattering or a bound state. Also the availability of correlation functions with non-zero momentum helps to reliably identify a scattering state.

Some of these tasks are already under way. We will produce 150 independent gauge field configurations with the same parameters as sets A66 and C77, but for a lattice size of $24^3 \times 48$. For set C77 we will create 600 independent gauge field configurations for a small lattice size of $12^3 \times 24$. These new sets can then be used to analyze finite volume effects for our approach.

Appendix A

Parameters of D_{CI}

Coeff. number	Name	Value	Path shape	γ	Multiplicity
1	s_1	1.481599252	$[\,]$	$\mathbb{1}$	1
2	s_2	-0.05218251439	$[i]$	$\mathbb{1}$	8
3	s_3	-0.01473643847	$[i,j]$	$\mathbb{1}$	48
5	s_5	-0.002186103421	$[i,j,k]$	$\mathbb{1}$	192
6	s_6	0.002133989696	$[i,i,j]$	$\mathbb{1}$	96
8	s_8	-0.003997001821	$[i,j,-i]$	$\mathbb{1}$	48
10	s_{10}	-0.0004951673735	$[i,j,k,l]$	$\mathbb{1}$	384
11	s_{11}	-0.0009836500799	$[i,j,-i,k]$	$\mathbb{1}$	384
13	s_{13}	0.007529838581	$[i,j,-i,-j]$	$\mathbb{1}$	48
14	v_1	0.1972229309	$[i]$	γ_i	8
15	v_2	0.008252157565	$[i,j]$	γ_i	96
17	v_4	0.005113056314	$[i,j,k]$	γ_i	384
18	v_5	0.001736609425	$[j,i,k]$	γ_i	192
32	t_1	-0.08792744664	$[i,j]$	$\gamma_i\gamma_\nu$	48
33	t_2	-0.002553055577	$[i,j,k]$	$\gamma_i\gamma_j$	384
34	t_3	0.002093792069	$[i,k,j]$	$\gamma_i\gamma_j$	192
36	t_5	-0.005567377075	$[i,j,-i]$	$\gamma_i\gamma_j$	48
46	t_{15}	-0.003427310798	$[j,i,-j,-i]$	$\gamma_i\gamma_j$	48
51	p_1	-0.008184103136	$[i,j,k,l]$	γ_5	384

Table A.1: *Coefficients for the CI fermion action used in this simulation. The path shapes are given symbolically, e.g., $[i,j]$ stands for a path in i-direction and then in j-direction ($i \neq j$). The γ-matrices (fifth column) are permuted as described in more detail in [17].*

Appendix B

Interpolators

The baryon interpolators we use are the following:

- N

$$O_N^{(i)} = \epsilon_{abc}\,\Gamma_1\,u_a\,(u_b^T\,\Gamma_2\,d_c - d_b^T\,\Gamma_2\,u_c) \tag{B.1}$$

- $\Delta_k,\ k = 1,2,3$

$$O_\Delta = \epsilon_{abc}\,u_a\,(u_b^T\,C\,\gamma_k\,u_c) \tag{B.2}$$

- Σ

$$O_\Sigma^{(i)} = \epsilon_{abc}\,\Gamma_1\,u_a\,(u_b^T\,\Gamma_2\,s_c - s_b^T\,\Gamma_2\,u_c) \tag{B.3}$$

- Ξ

$$O_\Xi^{(i)} = \epsilon_{abc}\,\Gamma_1\,s_a\,(s_b^T\,\Gamma_2\,u_c - u_b^T\,\Gamma_2\,s_c) \tag{B.4}$$

- $\Omega_k,\ k = 1,2,3$

$$O_\Omega = \epsilon_{abc}\,s_a\,(s_b^T\,C\,\gamma_k\,s_c) \tag{B.5}$$

For N, Σ and Ξ we have three possible Dirac structures, for Δ and Ω only one. Details about the matrices Γ_i and the quark smearings in the interpolators can be found in Tab. B.1 and Tab. B.2, respectively.

In the N and Δ channels we omit interpolators, which are numerically very similar to others and obtain a total of only 18 (for N) respectively 6 (for Δ) different interpolators.

The charge conjugation matrix C is defined through

$$C\,\gamma_\mu\,C^{-1} = -\gamma_\mu^{\mathrm{T}} \tag{B.6}$$

and γ_t is the Dirac matrix in (Euclidean) time direction.

In all tables for meson interpolators (Tab. B.3 to Tab. B.6) the two quark fields are labeled by a and b. The indices n, w and ∂_i correspond to the smearings narrow, wide and derivative, respectively. The γ_i is one of the spatial Dirac matrices. In case of the light mesons, the quark fields can be both up or down quarks, in the strange meson sector we use an up or down quark for field a and a strange quark for field b. The last columns, where the C parity is given, are strictly speaking only valid for light mesons, for strange mesons this quantum number only holds approximately.

$\chi^{(i)}$	$\Gamma_1^{(i)}$	$\Gamma_2^{(i)}$	Smearing	$\#_N$	$\#_\Sigma$ or $\#_\Xi$
$\chi^{(1)}$	$\mathbb{1}$	$C\,\gamma_5$	$(nn)n$	1	1
			$(nn)w$	2	2
			$(nw)n$	3	3
			$(nw)w$	4	4
			$(wn)n$		5
			$(wn)w$		6
			$(ww)n$	5	7
			$(ww)w$	6	8
$\chi^{(2)}$	γ_5	C	$(nn)n$	7	9
			$(nn)w$	8	10
			$(nw)n$	9	11
			$(nw)w$	10	12
			$(wn)n$		13
			$(wn)w$		14
			$(ww)n$	11	15
			$(ww)w$	12	16
$\chi^{(3)}$	$\imath\,\mathbb{1}$	$C\,\gamma_t\,\gamma_5$	$(nn)n$	13	17
			$(nn)w$	14	18
			$(nw)n$	15	19
			$(nw)w$	16	20
			$(wn)n$		21
			$(wn)w$		22
			$(ww)n$	17	23
			$(ww)w$	18	24

Table B.1: *Interpolators for the N, Σ and Ξ channels. The Dirac structures $\chi^{(i)}$, the quark smearings and the corresponding interpolator numbers $\#_X$ are given.*

smearing	$\#_\Delta$, $\#_\Omega$
$(nn)n$	1
$(nn)w$	2
$(nw)n$	3
$(nw)w$	4
$(ww)n$	5
$(ww)w$	6

Table B.2: *Interpolators for the Δ and Ω channels. The quark smearings and the corresponding interpolator numbers $\#_X$ are given.*

$\#_{0^-}$	interpolator(s)	C
1	$\overline{a}_n\gamma_5 b_n$	+
2	$\overline{a}_n\gamma_5 b_w + \overline{a}_w\gamma_5 b_n$	+
3	$\overline{a}_n\gamma_5 b_w - \overline{a}_w\gamma_5 b_n$	−
4	$\overline{a}_w\gamma_5 b_w$	+
5	$\overline{a}_n\gamma_t\gamma_5 b_n$	+
6	$\overline{a}_n\gamma_t\gamma_5 b_w + \overline{a}_w\gamma_t\gamma_5 b_n$	+
7	$\overline{a}_n\gamma_t\gamma_5 b_w - \overline{a}_w\gamma_t\gamma_5 b_n$	−
8	$\overline{a}_w\gamma_t\gamma_5 b_w$	+
9	$\overline{a}_{\partial_i}\gamma_i\gamma_5 b_n + \overline{a}_n\gamma_i\gamma_5 b_{\partial_i}$	+
10	$\overline{a}_{\partial_i}\gamma_i\gamma_5 b_n - \overline{a}_n\gamma_i\gamma_5 b_{\partial_i}$	−
11	$\overline{a}_{\partial_i}\gamma_i\gamma_5 b_w + \overline{a}_w\gamma_i\gamma_5 b_{\partial_i}$	+
12	$\overline{a}_{\partial_i}\gamma_i\gamma_5 b_w - \overline{a}_w\gamma_i\gamma_5 b_{\partial_i}$	−
13	$\overline{a}_{\partial_i}\gamma_i\gamma_t\gamma_5 b_n + \overline{a}_n\gamma_i\gamma_t\gamma_5 b_{\partial_i}$	−
14	$\overline{a}_{\partial_i}\gamma_i\gamma_t\gamma_5 b_n - \overline{a}_n\gamma_i\gamma_t\gamma_5 b_{\partial_i}$	+
15	$\overline{a}_{\partial_i}\gamma_i\gamma_t\gamma_5 b_w + \overline{a}_w\gamma_i\gamma_t\gamma_5 b_{\partial_i}$	−
16	$\overline{a}_{\partial_i}\gamma_i\gamma_t\gamma_5 b_w - \overline{a}_w\gamma_i\gamma_t\gamma_5 b_{\partial_i}$	+
17	$\overline{a}_{\partial_i}\gamma_5 b_{\partial_i}$	+
18	$\overline{a}_{\partial_i}\gamma_t\gamma_5 b_{\partial_i}$	+

Table B.3: *Meson interpolators for $J^P = 0^-$. The first row shows the number, the second shows the explicit form of the interpolator. If this is a sum of two terms we omit the factor $1/2$ for simplicity. In the last column the C parity is given. Interpolators obeying the same Dirac structure, but with different quark field smearings, are separated by dotted lines.*

$\#_{0^+}$	interpolator(s)	C
1	$\overline{a}_n b_n$	$+$
2	$\overline{a}_n b_w + \overline{a}_w b_n$	$+$
3	$\overline{a}_n b_w - \overline{a}_w b_n$	$-$
4	$\overline{a}_w b_w$	$+$
5	$\overline{a}_{\partial_i} \gamma_i b_n + \overline{a}_n \gamma_i b_{\partial_i}$	$-$
6	$\overline{a}_{\partial_i} \gamma_i b_n - \overline{a}_n \gamma_i b_{\partial_i}$	$+$
7	$\overline{a}_{\partial_i} \gamma_i b_w + \overline{a}_w \gamma_i b_{\partial_i}$	$-$
8	$\overline{a}_{\partial_i} \gamma_i b_w - \overline{a}_w \gamma_i b_{\partial_i}$	$+$
9	$\overline{a}_{\partial_i} \gamma_i \gamma_t b_n + \overline{a}_n \gamma_i \gamma_t b_{\partial_i}$	$-$
10	$\overline{a}_{\partial_i} \gamma_i \gamma_t b_n - \overline{a}_n \gamma_i \gamma_t b_{\partial_i}$	$+$
11	$\overline{a}_{\partial_i} \gamma_i \gamma_t b_w + \overline{a}_w \gamma_i \gamma_t b_{\partial_i}$	$-$
12	$\overline{a}_{\partial_i} \gamma_i \gamma_t b_w - \overline{a}_w \gamma_i \gamma_t b_{\partial_i}$	$+$
13	$\overline{a}_{\partial_i} b_{\partial_i}$	$+$

Table B.4: *Same as Tab. B.3, now for* $J^P = 0^+$.

$\#_{1^-}$	interpolator(s)	C
1	$\overline{a}_n\gamma_k b_n$	$-$
2	$\overline{a}_n\gamma_k b_w + \overline{a}_w\gamma_k b_n$	$-$
3	$\overline{a}_n\gamma_k b_w - \overline{a}_w\gamma_k b_n$	$+$
4	$\overline{a}_w\gamma_k b_w$	$-$
5	$\overline{a}_n\gamma_k\gamma_t b_n$	$-$
6	$\overline{a}_n\gamma_k\gamma_t b_w + \overline{a}_w\gamma_k\gamma_t b_n$	$-$
7	$\overline{a}_n\gamma_k\gamma_t b_w - \overline{a}_w\gamma_k\gamma_t b_n$	$+$
8	$\overline{a}_w\gamma_k\gamma_t b_w$	$-$
9	$\overline{a}_{\partial_k} b_n + \overline{a}_n b_{\partial_k}$	$+$
10	$\overline{a}_{\partial_k} b_n - \overline{a}_n b_{\partial_k}$	$-$
11	$\overline{a}_{\partial_k} b_w + \overline{a}_w b_{\partial_k}$	$+$
12	$\overline{a}_{\partial_k} b_w - \overline{a}_w b_{\partial_k}$	$-$
13	$\overline{a}_{\partial_k}\gamma_t b_n + \overline{a}_n\gamma_t b_{\partial_k}$	$-$
14	$\overline{a}_{\partial_k}\gamma_t b_n - \overline{a}_n\gamma_t b_{\partial_k}$	$+$
15	$\overline{a}_{\partial_k}\gamma_t b_w + \overline{a}_w\gamma_t b_{\partial_k}$	$-$
16	$\overline{a}_{\partial_k}\gamma_t b_w - \overline{a}_w\gamma_t b_{\partial_k}$	$+$
17	$\overline{a}_{\partial_i}\gamma_k b_{\partial_i}$	$-$
18	$\overline{a}_{\partial_i}\gamma_k\gamma_t b_{\partial_i}$	$-$
19	$\overline{a}_{\partial_k}\epsilon_{ijk}\gamma_j\gamma_5 b_n + \overline{a}_n\epsilon_{ijk}\gamma_j\gamma_5 b_{\partial_k}$	$+$
20	$\overline{a}_{\partial_k}\epsilon_{ijk}\gamma_j\gamma_5 b_n - \overline{a}_n\epsilon_{ijk}\gamma_j\gamma_5 b_{\partial_k}$	$-$
21	$\overline{a}_{\partial_k}\epsilon_{ijk}\gamma_j\gamma_5 b_w + \overline{a}_w\epsilon_{ijk}\gamma_j\gamma_5 b_{\partial_k}$	$+$
22	$\overline{a}_{\partial_k}\epsilon_{ijk}\gamma_j\gamma_5 b_w - \overline{a}_w\epsilon_{ijk}\gamma_j\gamma_5 b_{\partial_k}$	$-$
23	$\overline{a}_{\partial_k}\epsilon_{ijk}\gamma_j\gamma_t\gamma_5 b_n + \overline{a}_n\epsilon_{ijk}\gamma_j\gamma_t\gamma_5 b_{\partial_k}$	$-$
24	$\overline{a}_{\partial_k}\epsilon_{ijk}\gamma_j\gamma_t\gamma_5 b_n - \overline{a}_n\epsilon_{ijk}\gamma_j\gamma_t\gamma_5 b_{\partial_k}$	$+$
25	$\overline{a}_{\partial_k}\epsilon_{ijk}\gamma_j\gamma_t\gamma_5 b_w + \overline{a}_w\epsilon_{ijk}\gamma_j\gamma_t\gamma_5 b_{\partial_k}$	$-$
26	$\overline{a}_{\partial_k}\epsilon_{ijk}\gamma_j\gamma_t\gamma_5 b_w - \overline{a}_w\epsilon_{ijk}\gamma_j\gamma_t\gamma_5 b_{\partial_k}$	$+$

Table B.5: *Same as Tab. B.3, now for* $J^P = 1^-$.

$\#_{1^+}$	interpolator(s)	C
1	$\overline{a}_n\gamma_k\gamma_5 b_n$	$+$
2	$\overline{a}_n\gamma_k\gamma_5 b_w + \overline{a}_w\gamma_k\gamma_5 b_n$	$+$
3	$\overline{a}_n\gamma_k\gamma_5 b_w - \overline{a}_w\gamma_k\gamma_5 b_n$	$-$
4	$\overline{a}_w\gamma_k\gamma_5 b_w$	$+$
5	$\overline{a}_{\partial_k}\gamma_5 b_n + \overline{a}_n\gamma_5 b_{\partial_k}$	$+$
6	$\overline{a}_{\partial_k}\gamma_5 b_n - \overline{a}_n\gamma_5 b_{\partial_k}$	$-$
7	$\overline{a}_{\partial_k}\gamma_5 b_w + \overline{a}_w\gamma_5 b_{\partial_k}$	$+$
8	$\overline{a}_{\partial_k}\gamma_5 b_w - \overline{a}_w\gamma_5 b_{\partial_k}$	$-$
9	$\overline{a}_{\partial_k}\gamma_t\gamma_5 b_n + \overline{a}_n\gamma_t\gamma_5 b_{\partial_k}$	$+$
10	$\overline{a}_{\partial_k}\gamma_t\gamma_5 b_n - \overline{a}_n\gamma_t\gamma_5 b_{\partial_k}$	$-$
11	$\overline{a}_{\partial_k}\gamma_t\gamma_5 b_w + \overline{a}_w\gamma_t\gamma_5 b_{\partial_k}$	$+$
12	$\overline{a}_{\partial_k}\gamma_t\gamma_5 b_w - \overline{a}_w\gamma_t\gamma_5 b_{\partial_k}$	$-$
13	$\overline{a}_{\partial_i}\gamma_k\gamma_5 b_{\partial_i}$	$+$
14	$\epsilon_{ijk}\overline{a}_{\partial_k}\gamma_j b_n + \epsilon_{ijk}\overline{a}_n\gamma_j b_{\partial_k}$	$-$
15	$\epsilon_{ijk}\overline{a}_{\partial_k}\gamma_j b_n - \epsilon_{ijk}\overline{a}_n\gamma_j b_{\partial_k}$	$+$
16	$\epsilon_{ijk}\overline{a}_{\partial_k}\gamma_j b_w + \epsilon_{ijk}\overline{a}_w\gamma_j b_{\partial_k}$	$-$
17	$\epsilon_{ijk}\overline{a}_{\partial_k}\gamma_j b_w - \epsilon_{ijk}\overline{a}_w\gamma_j b_{\partial_k}$	$+$
18	$\epsilon_{ijk}\overline{a}_{\partial_k}\gamma_j\gamma_t b_n + \epsilon_{ijk}\overline{a}_n\gamma_j\gamma_t b_{\partial_k}$	$-$
19	$\epsilon_{ijk}\overline{a}_{\partial_k}\gamma_j\gamma_t b_n - \epsilon_{ijk}\overline{a}_n\gamma_j\gamma_t b_{\partial_k}$	$+$
20	$\epsilon_{ijk}\overline{a}_{\partial_k}\gamma_j\gamma_t b_w + \epsilon_{ijk}\overline{a}_w\gamma_j\gamma_t b_{\partial_k}$	$-$
21	$\epsilon_{ijk}\overline{a}_{\partial_k}\gamma_j\gamma_t b_w - \epsilon_{ijk}\overline{a}_w\gamma_j\gamma_t b_{\partial_k}$	$+$
22	$\overline{a}_n\gamma_k\gamma_t\gamma_5 b_n$	$-$
23	$\overline{a}_n\gamma_k\gamma_t\gamma_5 b_w + \overline{a}_w\gamma_k\gamma_t\gamma_5 b_n$	$-$
24	$\overline{a}_n\gamma_k\gamma_t\gamma_5 b_w - \overline{a}_w\gamma_k\gamma_t\gamma_5 b_n$	$+$
25	$\overline{a}_w\gamma_k\gamma_t\gamma_5 b_w$	$-$
26	$\overline{a}_{\partial_i}\gamma_k\gamma_t\gamma_5 b_{\partial_i}$	$-$

Table B.6: *Same as Tab. B.3, now for* $J^P = 1^+$.

References

[1] K. G. Wilson, *Confinement and quarks*, *Phys. Rev. D* **10** (1974) 2445.

[2] H. B. Nielsen and M. Ninomiya, *Absence of Neutrinos on a Lattice. 1. Proof by Homotopy Theory*, *Nucl. Phys.* **B185** (1981) 20.

[3] H. B. Nielsen and M. Ninomiya, *No Go Theorem for Regularizing Chiral Fermions*, *Phys. Lett.* **B105** (1981) 219.

[4] H. B. Nielsen and M. Ninomiya, *Absence of Neutrinos on a Lattice. 2. Intuitive Topological Proof*, *Nucl. Phys.* **B193** (1981) 173.

[5] H. Neuberger, *Exactly massless quarks on the lattice*, *Phys. Lett.* **B417** (1998) 141–144, [hep-lat/9707022].

[6] C. B. Lang, P. Majumdar, and W. Ortner, *First results from dynamical chirally improved fermions*, *PoS* **LAT2005** (2006) 131, [hep-lat/0509005].

[7] C. B. Lang, P. Majumdar, and W. Ortner, *QCD with two dynamical flavors of chirally improved quarks*, *Phys. Rev.* **D73** (2006) 034507, [hep-lat/0512014].

[8] C. B. Lang, P. Majumdar, and W. Ortner, *Dirac eigenmodes in an environment of dynamical fermions*, hep-lat/0512045.

[9] K. Nakamura *et al.*, *Review of particle physics*, *J. Phys.* **G37** (2010) 075021.

[10] R. P. Feynman, *Space-time approach to nonrelativistic quantum mechanics*, *Rev. Mod. Phys.* **20** (1948) 367–387.

[11] C. Gattringer and C. B. Lang, *Quantum chromodynamics on the lattice*, *Lect. Notes Phys.* **788** (2010) 1–211.

[12] P. H. Ginsparg and K. G. Wilson, *A Remnant of Chiral Symmetry on the Lattice*, *Phys. Rev.* **D25** (1982) 2649.

[13] M. Lüscher, *Exact chiral symmetry on the lattice and the Ginsparg- Wilson relation*, *Phys. Lett.* **B428** (1998) 342–345, [hep-lat/9802011].

[14] P. Hasenfratz and F. Niedermayer, *Perfect lattice action for asymptotically free theories*, *Nucl. Phys.* **B414** (1994) 785–814, [hep-lat/9308004].

[15] P. Hasenfratz, *Prospects for perfect actions*, *Nucl. Phys. Proc. Suppl.* **63** (1998) 53–58, [hep-lat/9709110].

[16] C. Gattringer, *A new approach to ginsparg-wilson fermions*, *Phys. Rev.* **D63** (2001) 114501, [hep-lat/0003005].

[17] C. Gattringer, I. Hip, and C. B. Lang, *Approximate ginsparg-wilson fermions: A first test*, *Nucl. Phys.* **B597** (2001) 451–474, [hep-lat/0007042].

[18] D. B. Kaplan, *A Method for simulating chiral fermions on the lattice*, *Phys. Lett.* **B288** (1992) 342–347, [hep-lat/9206013].

[19] H. Neuberger, *More about exactly massless quarks on the lattice*, *Phys. Lett.* **B427** (1998) 353–355, [hep-lat/9801031].

[20] S. Aoki *et al.*, *Two-flavor QCD simulation with exact chiral symmetry*, *Phys. Rev.* **D78** (2008) 014508, [arXiv:0803.3197].

[21] N. Cundy *et al.*, *Numerical methods for the QCD overlap operator. IV: Hybrid Monte Carlo*, *Comput. Phys. Commun.* **180** (2009) 26–54, [hep-lat/0502007].

[22] N. Cundy, S. Krieg, and T. Lippert, *Improving the dynamical overlap algorithm*, *PoS* **LAT2005** (2005) 107, [hep-lat/0511044].

[23] N. Cundy *et al.*, *Dynamical overlap fermions with increased topological tunnelling*, *PoS* **LATTICE2007** (2007) 030, [arXiv:0710.1785].

[24] N. Cundy *et al.*, *Topological tunneling with Dynamical overlap fermions*, *Comput. Phys. Commun.* **180** (2009) 201–208, [arXiv:0803.0294].

[25] T. DeGrand and S. Schaefer, *Physics issues in simulations with dynamical overlap fermions*, *Phys. Rev. D* **71** (2005) 034507, [hep-lat/0412005].

[26] T. DeGrand and S. Schaefer, *Chiral properties of two-flavor QCD in small volume and at large lattice spacing*, *Phys. Rev. D* **72** (2005) 054503, [hep-lat/0506021].

[27] G. I. Egri *et al.*, *Topology with Dynamical Overlap Fermions*, *JHEP* **0601** (2006) 049, [hep-lat/0510117].

[28] Z. Fodor, S. D. Katz, and K. K. Szabo, *Dynamical overlap fermions, results with hybrid Monte-Carlo algorithm*, *Nucl. Phys. B (Proc. Suppl.)* **140** (2005) 704, [hep-lat/0409070].

[29] T. Kaneko *et al.*, *JLQCD's dynamical overlap project*, *PoS* **LAT2006** (2006) 054, [hep-lat/0610036].

[30] H. Matsufuru *et al.*, *Improvement of algorithms for dynamical overlap fermions*, *PoS* **LAT2006** (2006) 031, [hep-lat/0610026].

[31] J. Noaki *et al.*, *Light meson spectrum with $N_f = 2$ dynamical overlap fermions*, *PoS* **LAT2007** (2007) 126, [arXiv:0710.0929].

[32] C. Allton *et al.*, *Physical Results from 2+1 Flavor Domain Wall QCD and SU(2) Chiral Perturbation Theory*, *Phys. Rev.* **D78** (2008) 114509, [arXiv:0804.0473].

[33] S. Aoki *et al.*, *2+1 Flavor Lattice QCD toward the Physical Point*, *Phys. Rev.* **D79** (2009) 034503, [arXiv:0807.1661].

[34] B. Blossier *et al.*, *Light quark masses and pseudoscalar decay constants from Nf=2 Lattice QCD with twisted mass fermions*, *JHEP* **04** (2008) 020, [arXiv:0709.4574].

[35] P. Boucaud *et al.*, *Dynamical twisted mass fermions with light quarks*, *Phys. Lett.* **B650** (2007) 304–311, [hep-lat/0701012].

[36] S. Durr *et al.*, *Ab-Initio Determination of Light Hadron Masses*, *Science* **322** (2008) 1224–1227, [arXiv:0906.3599].

[37] E. E. Scholz, *Physical results from 2+1 flavor Domain Wall QCD*, *PoS* **LATTICE2008** (2008) 095, [arXiv:0809.3251].

[38] R. Sommer, *A New Way to Set the Energy Scale in Lattice Gauge Theories and itsApplication to the Static Force and α_s in SU(2) Yang–MillsTheory*, *Nucl. Phys. B* **411** (1994) 839, [hep-lat/9310022].

[39] A. Hasenfratz and F. Knechtli, *Flavor Symmetry and the Static Potential with Hypercubic Blocking*, *Phys. Rev. D* **64** (2001) 034504, [hep-lat/0103029].

[40] C. Gattringer *et al.*, *Hadron Spectroscopy with Dynamical Chirally Improved Fermions*, *Phys. Rev.* **D79** (2009) 054501, [arXiv:0812.1681].

[41] M. Lüscher and P. Weisz, *On-shell improved lattice gauge theories*, *Commun. Math. Phys.* **97** (1985) 59.

[42] M. Alford *et al.*, *Lattice QCD on Small Computers*, *Phys. Lett. B* **361** (1995) 87, [hep-lat/9507010].

[43] R. Frigori *et al.*, *Dynamical Chirally Improved Quarks: First Results for Hadron Masses*, *PoS* **LAT2007** (2007) 114, [arXiv:0709.4582].

[44] T. Burch *et al.*, *Spatially improved operators for excited hadrons on the lattice*, *Phys. Rev.* **D70** (2004) 054502, [hep-lat/0405006].

[45] T. Burch *et al.*, *Variational method for lattice spectroscopy with ghosts*, *Phys. Rev.* **D73** (2006) 017502, [hep-lat/0511054].

[46] T. Burch *et al.*, *Excited hadrons on the lattice: Mesons*, *Phys. Rev.* **D73** (2006) 094505, [hep-lat/0601026].

[47] T. Burch *et al.*, *Excited hadrons on the lattice: Baryons*, *Phys. Rev.* **D74** (2006) 014504, [hep-lat/0604019].

[48] T. Burch *et al.*, *B meson excitations with chirally improved light quarks*, *PoS* **LAT2007** (2007) 091, [arXiv:0709.3708].

[49] T. Burch *et al.*, *Excitations of single-beauty hadrons*, *Phys. Rev.* **D79** (2009) 014504, [arXiv:0809.1103].

[50] T. Burch *et al.*, *Heavy-light hadrons and their excitations*, *PoS* **LATTICE2008** (2008) 110, [arXiv:0809.3923].

[51] G. Engel *et al.*, *Excited hadrons in $N_f = 2$ QCD*, *PoS* **LAT2009** (2009) 088, [arXiv:0910.2802].

[52] G. Engel *et al.*, *Baryon axial charges from Chirally Improved fermions - first results*, *PoS* **LAT2009** (2009) 135, [arXiv:0910.4190].

[53] G. P. Engel *et al.*, *Meson and baryon spectrum for QCD with two light dynamical quarks*, *Phys. Rev.* **D82** (2010) 034505, [arXiv:1005.1748].

[54] C. Gattringer *et al.*, *Spectroscopy with dynamical Chirally Improved quarks*, *PoS* **LATTICE2008** (2008) 093, [arXiv:0809.4514].

[55] S. Duane *et al.*, *Hybrid Monte-Carlo*, *Phys. Lett. B* **195** (1987) 216.

[56] D. H. Weingarten and D. N. Petcher, *Monte Carlo Integration for Lattice Gauge Theories with Fermions*, *Phys. Lett.* **B99** (1981) 333.

[57] W. Ortner, *Dynamical chirally improved fermions in lattice QCD*, PhD thesis, Univ. Graz, 2006.

[58] I. P. Omelyan, I. M. Mryglod, and R. Folk, *Construction of high-order force-gradient algorithms for integration of motion in classical and quantum systems*, *Phys. Rev. E* **66** (2002) 026701.

[59] I. P. Omelyan, I. M. Mryglod, and R. Folk, *Symplectic analytically integrable decomposition algorithms: classification, derivation, and application to molecular dynamics, quantum and celestial mechanics simulations*, *Computer Physics Communications* **151** (2003) 272.

[60] J. C. Sexton and D. H. Weingarten, *Hamiltonian evolution for the hybrid Monte Carlo algorithm*, *Nucl. Phys.* **B380** (1992) 665–678.

[61] C. Urbach *et al.*, *HMC algorithm with multiple time scale integration and mass preconditioning*, *Comput. Phys. Commun.* **174** (2006) 87–98, [hep-lat/0506011].

[62] M. Hasenbusch, *Speeding up the Hybrid-Monte-Carlo algorithm for dynamical fermions*, *Phys. Lett. B* **519** (2001) 177, [hep-lat/0107019].

[63] R. C. Brower *et al.*, *Chronological inversion method for the Dirac matrix in hybrid Monte Carlo*, *Nucl. Phys.* **B484** (1997) 353, [hep-lat/9509012].

[64] S. Durr *et al.*, *Scaling study of dynamical smeared-link clover fermions*, *Phys. Rev.* **D79** (2009) 014501, [arXiv:0802.2706].

[65] C. Gottbrath *et al.*, *The Effects of Moore's Law and Slacking on Large Computations*, astro-ph/9912202.

[66] A. Ukawa, *Computational cost of full QCD simulations experienced by CP-PACS and JLQCD Collaborations*, *Nucl. Phys. Proc. Suppl.* **106** (2002) 195–196.

[67] M. Creutz, *Global MC algorithms for many fermion systems*, *Phys. Rev. D* **38** (1988) 1228.

[68] Y. Namekawa *et al.*, *Light hadron spectroscopy in two-flavor QCD with small sea quark masses*, *Phys. Rev. D* **70** (2004) 074503, [hep-lat/0404014].

[69] B. Joo *et al.*, *Instability in the molecular dynamics step of hybrid Monte Carlo in dynamical Fermion lattice QCD simulations*, *Phys. Rev. D* **62** (2000) 114501, [hep-lat/0005023].

[70] L. Del Debbio *et al.*, *Stability of lattice QCD simulations and the thermodynamic limit*, *JHEP* **0602** (2006) 011, [hep-lat/0512021].

[71] Y. Chen *et al.*, *The Sequential Empirical Bayes Method: An adaptive constrained-curve fitting algorithm for lattice QCD*, hep-lat/0405001.

[72] G. P. Lepage *et al.*, *Constrained curve fitting*, *Nucl. Phys. Proc. Suppl.* **106** (2002) 12–20, [hep-lat/0110175].

[73] M. Asakawa, T. Hatsuda, and Y. Nakahara, *Maximum entropy analysis of the spectral functions in lattice QCD*, *Prog. Part. Nucl. Phys.* **46** (2001) 459–508, [hep-lat/0011040].

[74] K. Sasaki *et al.*, *Excited nucleon spectrum from lattice QCD with maximum entropy method*, *Nucl. Phys. Proc. Suppl.* **129** (2004) 212–214, [hep-lat/0309177].

[75] M. Lüscher and U. Wolff, *How to calculate the Elastic Scattering Matrix in 2-Dimensional QuantumField Theories by Numerical Simulation*, *Nucl. Pbys. B* **339** (1990) 222.

[76] C. Michael, *Adjoint Sources in Lattice Gauge Theory*, *Nucl. Phys. B* **259** (1985) 58.

[77] J. Bulava *et al.*, *Nucleon, Δ and Ω excited states in $N_f = 2 + 1$ lattice QCD*, *Phys. Rev.* **D82** (2010) 014507, [arXiv:1004.5072].

[78] T. Burch *et al.*, *Low and high spin mesons from $N_f = 2$ Clover-Wilson lattices*, *Phys. Rev.* **D79** (2009) 114503, [arXiv:0903.2358].

[79] B. Blossier *et al.*, *Efficient use of the Generalized Eigenvalue Problem*, *PoS* **LATTICE2008** (2008) 135, [arXiv:0808.1017].

[80] B. Blossier *et al.*, *On the generalized eigenvalue method for energies and matrix elements in lattice field theory*, *JHEP* **04** (2009) 094, [arXiv:0902.1265].

[81] C. Best *et al.*, *Pion and rho structure functions from lattice QCD*, *Phys. Rev.* **D56** (1997) 2743–2754, [hep-lat/9703014].

[82] S. Gusken *et al.*, *Non-Singlet Axial Vector Couplings of the Baryon Octet in Lattice QCD*, *Phys. Lett.* **B227** (1989) 266.

[83] C. Gattringer *et al.*, *Derivative sources in lattice spectroscopy of excited mesons*, *Phys. Rev. D* **78** (2008) 034501, [arXiv:0802.2020].

[84] M. Albanese *et al.*, *Glueball Masses and String Tension in Lattice QCD*, *Phys. Lett.* **B192** (1987) 163–169.

[85] A. Hasenfratz, R. Hoffmann, and S. Schaefer, *Hypercubic Smeared Links for Dynamical Fermions*, *JHEP* **05** (2007) 029, [hep-lat/0702028].

[86] C. Morningstar and M. Peardon, *Analytic Smearing of SU(3) Link Variables in Lattice QCD*, *Phys. Rev. D* **69** (2004) 054501, [hep-lat/0311018].

[87] A. K. De, A. Harindranath, and J. Maiti, *On Scale Determination in Lattice QCD with Dynamical Quarks*, arXiv:0803.1281.

[88] N. Mathur *et al.*, *Scalar Mesons a0(1450) and sigma(600) from Lattice QCD*, *Phys. Rev.* **D76** (2007) 114505, [hep-ph/0607110].

[89] S. Prelovsek and D. Mohler, *A Lattice study of light scalar tetraquarks*, *Phys. Rev.* **D79** (2009) 014503, [arXiv:0810.1759].

[90] J. Gasser and H. Leutwyler, *Chiral Perturbation Theory to One Loop*, *Ann. Phys.* **158** (1984) 142.

[91] J. Gasser and H. Leutwyler, *Chiral Perturbation Theory: Expansions in the Mass of the Strange Quark*, *Nucl. Phys.* **B250** (1985) 465.

[92] S. Weinberg, *Phenomenological Lagrangians*, *Physica* **A96** (1979) 327.

[93] A. Walker-Loud *et al.*, *et al.*, *Light hadron spectroscopy using domain wall valence quarks on an Asqtad sea*, *Phys. Rev.* **D79** (2009) 054502, [arXiv:0806.4549].

[94] A. Walker-Loud, *New lessons from the nucleon mass, lattice QCD and heavy baryon chiral perturbation theory*, *PoS* **LATTICE2008** (2008) 005, [arXiv:0810.0663].

[95] L. D. Roper, *Evidence for a P-11 Pion-Nucleon Resonance at 556 MeV*, *Phys. Rev. Lett.* **12** (1964) 340–342.

[96] S. Basak *et al.*, *Lattice QCD determination of patterns of excited baryon states*, *Phys. Rev.* **D76** (2007) 074504, [arXiv:0709.0008].

[97] W. Melnitchouk *et al.*, *Excited baryons in lattice QCD*, *Phys. Rev.* **D67** (2003) 114506, [hep-lat/0202022].

[98] B. Lasscock *et al.*, *et al.*, *Even parity excitations of the nucleon in lattice QCD*, *Phys. Rev.* **D76** (2007) 054510, [arXiv:0705.0861].

[99] M. Mahbub *et al.*, *Isolating the Roper Resonance in Lattice QCD*, *Phys. Lett.* **B679** (2009) 418–422, [arXiv:0906.5433].

[100] N. Mathur *et al.*, *Roper resonance and S(11)(1535) from lattice QCD*, *Phys. Lett.* **B605** (2005) 137–143, [hep-ph/0306199].

[101] K. Sasaki, S. Sasaki, and T. Hatsuda, *Spectral analysis of excited nucleons in lattice QCD with maximum entropy method*, *Phys. Lett.* **B623** (2005) 208–217, [hep-lat/0504020].

[102] T. T. Takahashi and T. Kunihiro, *Axial charges of N(1535) and N(1650) in lattice QCD with two flavors of dynamical quarks*, *Phys. Rev.* **D78** (2008) 011503, [arXiv:0801.4707].

[103] S. Prelovsek, *Simulations of light scalar mesons on the lattice and related difficulties*, arXiv:0804.2549.

[104] K. Jansen, C. Michael, and C. Urbach, *The eta' meson from lattice QCD*, *Eur. Phys. J. C* **58** (2008) 261, [arXiv:0804.3871].

[105] J. J. J. Kokkedee, *The Quark Model*. W. A. Benjamin, NY, 1969.

[106] M. Gell-Mann, R. J. Oakes, and B. Renner, *Behavior of Current Divergences under SU(3)xSU(3)*, *Phys. Rev.* **175** (1968) 2195.

[107] H. Leutwyler, *On the foundations of chiral perturbation theory*, *Ann. Phys.* **235** (1994) 165–203, [hep-ph/9311274].

[108] G. Colangelo, J. Gasser, and H. Leutwyler, *Pi Pi Scattering*, *Nucl. Phys.* **B603** (2001) 125, [hep-ph/0103088].

[109] L. Y. Glozman, *Chiral multiplets of excited mesons*, *Phys. Lett.* **B587** (2004) 69–77, [hep-ph/0312354].

[110] L. Y. Glozman, *Restoration of chiral and $U(1)_A$ symmetries in excited hadrons*, *Phys. Rept.* **444** (2007) 1–49, [hep-ph/0701081].

[111] L. Y. Glozman and A. V. Nefediev, *Chiral symmetry and the string description of excited hadrons*, *Phys. Rev.* **D76** (2007) 096004, [arXiv:0704.2673].

[112] L. Y. Glozman and A. V. Nefediev, *Chiral symmetry, the angular content of the vector current in QED and QCD, and the holographic description of hadrons*, *Phys. Rev.* **D80** (2009) 057901, [arXiv:0904.3067].

[113] L. Y. Glozman, C. B. Lang, and M. Limmer, *Angular momentum content of the ρ-meson in lattice QCD*, *Phys. Rev. Lett.* **103** (2009) 121601, [arXiv:0905.0811].

[114] L. Y. Glozman, C. B. Lang, and M. Limmer, *The chiral and angular momentum content of the ρ-meson*, *Few Body Syst.* **47** (2010) 91–103, [arXiv:0909.2939].

[115] L. Y. Glozman, C. B. Lang, and M. Limmer, *Effective chiral restoration in the ρ'-meson in lattice QCD*, *Phys. Rev.* **D82** (2010) 097501, [arXiv:1007.1346].

[116] L. Y. Glozman, C. B. Lang, and M. Limmer, *The chiral and angular momentum content of the ρ-mesons in lattice QCD*, *PoS* **LATTICE2010** (2010) 149, [arXiv:1010.5660].

[117] S. Godfrey and N. Isgur, *Mesons in a Relativized Quark Model with Chromodynamics*, *Phys. Rev.* **D32** (1985) 189–231.

Danksagung

An dieser Stelle möchte ich mich bei allen Menschen bedanken, die zum Entstehen dieser Arbeit beigetragen haben.

Bei meinen Doktorvater Prof. Dr. Christian Lang möchte ich mich ganz herzlich bedanken. Er gab mir die Möglichkeit zu dieser Arbeit und hatte immer ein offenes Ohr für meine zahlreichen Fragen. Wann immer ich an meinen Vorhaben zweifelte, gab er mir meine Motivation zurück. Genauso großer Dank geht an die Gittergruppe der Karl-Franzens-Universität Graz, allen voran an Prof. Dr. Christof Gattringer. Durch ihn wurde in Form meiner Diplomarbeit sozusagen der Grundstein zu dieser Arbeit gelegt.

Großer Dank geht auch an Prof. Dr. Andreas Schäfer für die großzügige finanzielle Ünterstützung und die tolle Zusammenarbeit.

Des Weiteren bedanke ich mich bei allen (auch ehemaligen) Mitarbeitern und Kollegen, mit denen ich meine Zeit verbringen durfte. Für viele wertvolle Diskussionen bedanke ich mich bei Georg Engel, Prof. Dr. Leonid Glozman und Daniel Mohler. Bei Erek Bilgici, Georg Engel, Gernot Lassnig und Dr. Bernd-Jochen Schaefer möchte ich mich auch für die Beantwortung aller Fragen „jenseits der Physik“ ganz herzlich bedanken.

Meinen Korrekturlesern Prof. Dr. Robert Danzer, Georg Engel und Daniel Mohler sei an dieser Stelle für die hilfreichen Verbesserungsvorschläge gedankt.

Nicht zu vergessen sind die Personen, ohne die Vieles nicht funktionieren würde. Daher bedanke ich mich auch bei unserer Sekretärin Claudia Spidla und den EDV-Beauftragten Eva Rothwangl und Martin Volk

Ich möchte mich auch bei allen Menschen bedanken, die mir – unabhängig von der Physik – geholfen haben, diese Arbeit fertig zu stellen, ganz besonders bei Brigitte und Robert Danzer.

Der größte Dank jedoch geht an meine Famile. Ohne deren Unterstützung, in jeglicher Hinsicht, wäre ich nicht bis hierher gekommen. Die allerbeste Motivation aber ging immer von meinem Sohn aus: Danke, Moritz!

Graz, im April 2011